



## Deliverable Report D1.43

# Methods for feed-forward control and real time system simulator

Agreement n.:	308974
Duration	November 2012 – October 2017
Co-ordinator:	DTU Wind



The research leading to these results has received funding from the European Community's Seventh Framework Programme FP7-ENERGY-2012-1-2STAGE under grant agreement No. 308974 (INN WIND.EU)



## Document information

Document Name:	D1.43 Methods for feed-forward control and real time system simulator
Document Number:	Deliverable D 1.43
Author:	Anand Natarajan, Athanasios Barlas, Troels Friis Pedersen, Torben Mikkelsen, Mikael Sjöholm (DTU) Avishek Kumar, Oscar Hughes Salas (DNV GL) Vasilis Riziotis (NTUA), Dimitris Manolas (NTUA) Rene Bos (TUD)
Document Type	Report
Dissemination level	PU
Review:	Takis Chaviaropoulos
Date:	Aug 30, 2017
WP:	1
Task:	4
Approval:	Approved by WP Leader



## Table of Contents

1.0 Introduction and Objectives .....	6
Applications for turbine control.....	7
Flap fatigue/extreme load reduction feedback controller .....	7
Flap AEP increase/fatigue reduction inflow scheduled controller .....	9
Comparisons with Pitch control .....	10
2.0 Application of Distributed Blade Control to Three Bladed Wind Turbines .....	11
Inflow-based flap control on the DTU 10MW RWT mounted on DTU jacket (NTUA).....	11
Description of the spinner anemometer controller .....	11
Tuning of the spinner anemometer controller .....	12
Results from application of the spinner anemometer controller on the DTU 10MW RWT mounted on DTU jacket.....	17
Comparison of Individual Pitch Control and Individual Pitch + Flap Control on INN WIND 10 MW RWT (DNV GL (UK)).....	25
Background.....	25
Modelling of the 10 MW Reference Turbine with Flaps .....	25
Blade root load and blade tip deflection comparison .....	29
Control Design.....	31
Supervisory Control.....	35
Results .....	37
3.0 Application of Distributed Blade Control to Two Bladed Wind Turbines (DTU) .....	40
Comparison of the DTU 10MW two bladed wind turbine in onshore and floating configurations.....	40
Evaluation of individual flap control on the DTU 10MW two-bladed wind turbine in onshore configuration .....	43



Evaluation of individual flap control on the DTU 10MW two-bladed wind turbine on the semi-floater .....	45
4.0 Spinner Anemometer and Spinner Lidar Demonstrations (DTU) .....	47
Zero wind speed calibration .....	48
Wind tunnel calibration of sonic sensors .....	49
Internal calibration of the spinner anemometer .....	49
Calibration for inflow angle measurements .....	49
Calibration of local and free wind speed measurements with use of NTF .....	51
Demonstration of Fatigue Load Reduction with De-Rating .....	56
Spinner Lidar Demonstration .....	58
5.0 Spinner Anemometer based Feed Forward Control (DTU) .....	62
Inflow-based flap control on the two-bladed DTU 10MW RWT on the semi-floater .....	62
6.0 Stochastic Embedded Gust Simulations for Design Loads (TUD) .....	66
Introduction .....	66
Response to extreme gusts .....	66
Set-up .....	66
Response in the yz-plane .....	67
Response in the time domain .....	68
Application to Lidar-assisted control .....	72
Set-up .....	72
1.1.1 Velocity field reconstruction .....	73
A gust measured in the field .....	75
1.1.2 Construction of a control input signal .....	76
1.2 DLC 1.1 extreme load predictions .....	78
1.2.1 Case study: the NREL 5 MW .....	79
An importance sampling method .....	81
8.0 Conclusions .....	85
References .....	87
Appendix A Load case definition for 10 MW Reference, IPC vs IFPC Comparison (DNV GL) .....	89
General Comments .....	89
Fatigue Load Cases .....	89



Extreme Load Cases ..... 92



## 1.0 Introduction and Objectives

An assessment of individual pitch control (IPC) and distributed blade flap based in combination with wind measurements using Lidars or spinner anemometers is made for different innovative 10 MW offshore wind turbine designs. Further validations of the performance of the spinner anemometer and spinner Lidar with measurements from instrumented research wind turbines are described which quantify the potential for its use in aid of flap based control.

The implementations of individual and distributed blade flaps instead of full-span pitch control is performed using several developed control algorithms and evaluated using detailed aeroelastic simulations on different innovative wind turbine designs. Wind measurements from the Spinner anemometer data are directly utilized in load simulations with distributed flap control to quantify its benefits. These research targets are explored and the outcomes quantified in this report in terms of the following:

1. Implementation and quantification of loads reduction potential from distributed blade flap control with and without wind measurement feed-forward control on three bladed and 2 bladed rotors.
2. A comparison between IPC and flap control on their loads reduction potential on 3 bladed rotors
3. Wind simulation methods to simulate realistic gust events occurring in the atmosphere as a means to validate the performance of controls that use wind measurements.
4. An assessment on the potential for LCOE reduction from distributed blade control and spinner anemometer, spinner Lidar based wind measurements

### Overview of Blade Flap based Distributed Control (DTU)

New concepts for distributed load reduction methods focus on a faster and localized load control, compared to existing individual blade pitch control, by utilizing active aerodynamic control devices distributed along the blade span [1]. Results in literature from numerical and experimental analysis mostly focusing on trailing edge flaps have shown a considerable potential in fatigue and extreme load reduction [2][3][4]. Existing work has provided aeroelastic tools with the capability of simulating active flap configurations, however the benefit of applying distributed flap control on innovative rotor and offshore support structure designs, or utilizing inflow sensor measurements has not yet been fully explored.

The INN WIND 10MW Reference Wind Turbine (RWT) [5] is used for the aeroelastic simulations, as a representative modern multi-MW wind turbine model utilized in the INN WIND.EU project. The simulated flap configuration is chosen based on prior studies [4], with the parameters utilized in the two-bladed setups shown in Table 1. In the studies by DTU, the unsteady aerodynamics associated with the active flaps is accounted for by using the ATEFlap dynamic stall model in the aeroelastic code HAWC2 [6][7]. The variation of steady lift, drag, and moment coefficients introduced by the flap deflection is based on 2D CFD simulations. The flap structural dynamics are not accounted for,



assuming a small flap and actuator size and weight, and not coupling with the rest of the blade structure. The actuator dynamics are implemented as a linear servo model, for a first order system with a time constant of 0.1s. This corresponds to the characteristics of a Controllable Rubber Trailing Edge Flap (CRTEF) actuator developed by DTU [2].

Table 1 – Main flap system parameters (two-bladed rotor).

Flap configuration	
Chordwise extension	10%
Deflection angle limits	$\pm 10^\circ$
Spanwise length	25.9m (30% blade length)
Spanwise location	56.1379m-82.0477m (from blade root)
Airfoil	FFA-W3-241
Max $\Delta C_l$	$\pm 0.4$
Deflection rate limit	100°/s
Actuator time constant	100ms

### Applications for turbine control

The distributed flap controllers are applied on top of the baseline DTU turbine mounted on a jacket, an innovative semi floater with 2-bladed and 3-bladed rotor. Further evaluation of several flap control concepts have been investigated in combination with the innovative rotor and offshore support structure wind turbine configurations. Constrained turbulent gust based load simulations are explained in the end as a future means for validating flap control performance.

### Flap fatigue/extreme load reduction feedback controller

A blade-independent, feedback active flap controller is specified. The controller is a simple implementation of a blade-independent, feedback based controller using the high-pass-filtered blade root flapwise bending moment. Only the dynamic part of the controller is described, with no supervisory functions (wind speed range of operation, transition in power regions, faults etc). The block diagram of the flap controller is shown, in relation to the main controller, sensors and actuators (Figure 1), and focusing on its internal processes (Figure 2).

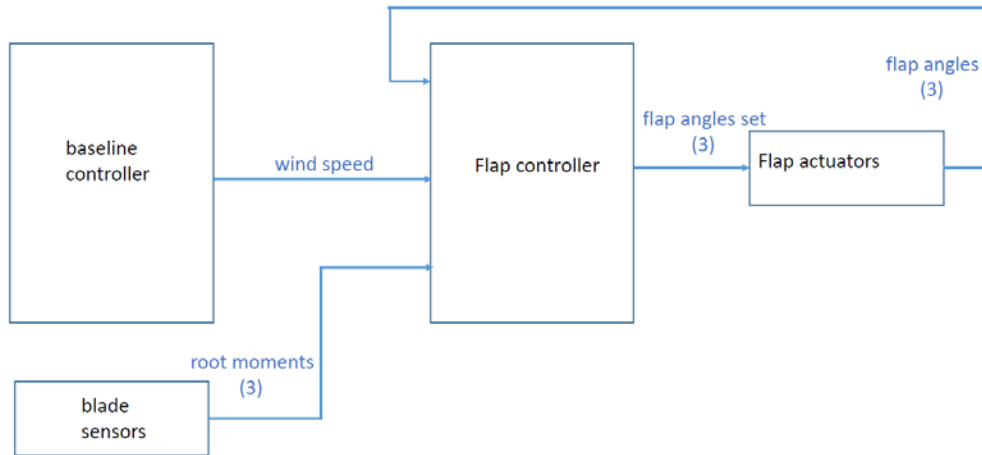


Figure 1 - Flap controller block diagram - relation to main controller, sensors and actuators.

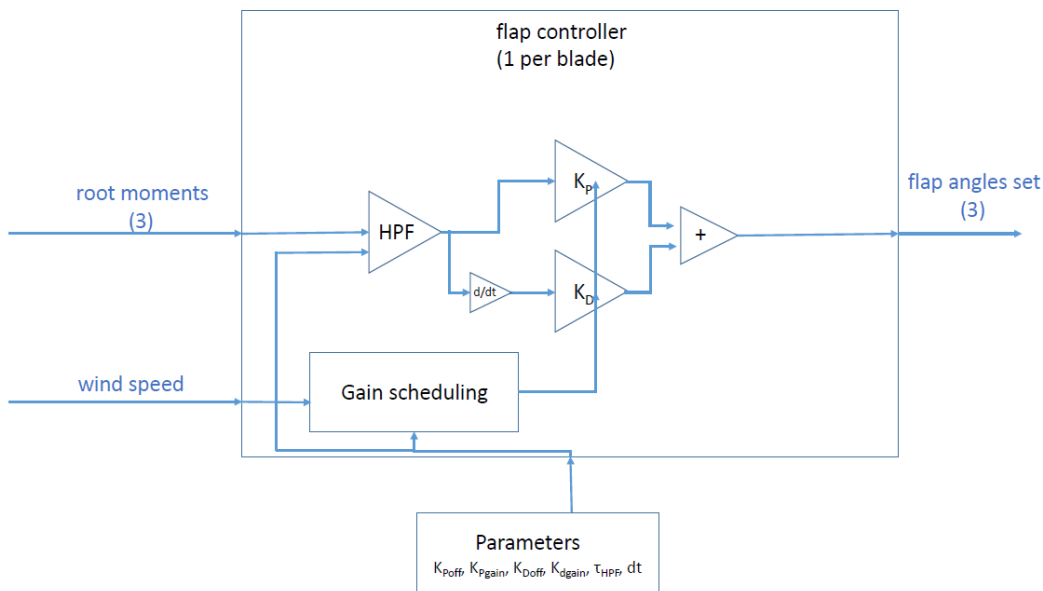


Figure 2 - Flap controller block diagram – internal processes.

In every time step, the flap controller reads the measured blade flapwise root bending moments and applies a high-pass filter (HPF) with a lower cut-off frequency, in order to remove the steady-state part. A proportional gain is applied on the HPF moments and a derivative gain on the derived HPF moments, and signals are summed. The P and D gains are linearly scheduled for the average wind speed during



the controller tuning process. The actual P and D gains are calculated in every time step, based on the average wind speed, in the HAWC2 case, a low pass filtered hub-height wind speed signal, coming from the main controller. The pitch setting in full load operation can also be used for the scheduling, with a higher-order fit if necessary. The resulting flap angle command signals are then send to the flap servo, in our case a first-order low-pass filter, simulating the flap actuators. For the extreme load control part a threshold parameter is set, where if the measured blade flapwise root bending moments exceeds this value, the flaps are collectively set to their extreme negative position, as described in [3].

### Flap AEP increase/fatigue reduction inflow scheduled controller

A scheduled quasi-steady active flap controller utilizing only spinner anemometer inflow signals is described. The controller comprises of a flap scheduling for below rated operating, targeting at increasing power output, and an on-off flap target for increased turbulence operation above rated. The block diagram of the flap controller is shown, in relation to the main controller, sensors and actuators (Figure 3).

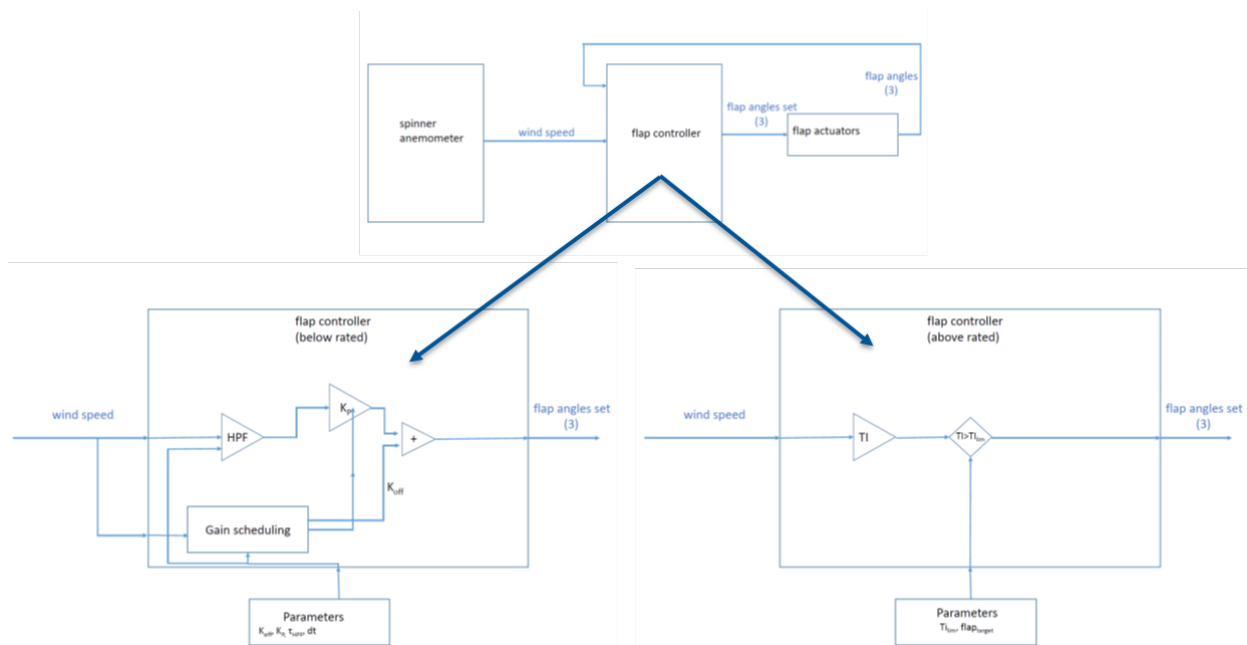


Figure 3 - Inflow-based flap controller block diagram

In every time step, the flap controller reads the measured spinner anemometer hub-height wind speed. Below rated, it schedules the flap angle according to Equation 1, and above rated it set the flap to a target angle when the measured turbulence intensity in a window of 100s exceeds 10% of the IEC value. The parameters have been tuned based on parametric studies.



$$\beta = K(V_{av}) \cdot V + offset(V_{av})$$

-(1)

## Comparisons with Pitch control

Active flap control methods have been extensively compared against individual pitch control on onshore reference configurations in various prior studies. Within the context of the INNWIND.EU project, D2.3.2 (Validation of New Control Concepts by Advanced Fluid-Structure Interaction Tools) [4] includes studies from NTUA, TU Delft and DTU on comparison and combination of individual pitch and flap controllers. A common outcome is that the flap controller is able to achieve similar load reduction objectives by replacing pitch activity by flap activity, thus limiting any impact on the pitch bearing damage. With both controllers used simultaneously, the blade load reduction is increased, while reducing the demands on the flap actuation. In the following sections the benefits of IFC are compared now for offshore innovative configurations.



## 2.0 Application of Distributed Blade Control to Three Bladed Wind Turbines

### Inflow-based flap control on the DTU 10MW RWT mounted on DTU jacket (NTUA)

#### Description of the spinner anemometer controller

An individual flap control algorithm based on wind speed measurements obtained using a spinner anemometer is described below. The controller uses flap actuators with the aim to remove any deterministic source of load variation on blades, associated with the characteristics of the inflow. Such load variations are concentrated on multiples of the rotational frequency ( $p$  multiples) and they are mainly due to i) wind yaw misalignment - within the range that yaw control is not activated ii) ABL shear and iii) wind inclination. The aim of the controller is to assist operation of the conventional feedback individual pitch controller (IPC) and thereby reduce its control duty cycle. Then, IPC control is only employed for removing 1P excitation due to the rotational sampling of turbulence.

Inflow yaw and inclination (tilt) angles can be directly calculated through the three components of the wind velocity measured by the spinner anemometer. Moreover, information about the ABL characteristics (an estimate of the shear exponent) can be also obtained through cross correlation characteristics of the axial and vertical wind components. The absolute value of the covariance of  $u$ ,  $w$  components increases as the shear exponent increases. The instantaneous yaw and tilt angles provided by spinner anemometer measurements are low-pass filtered with the aim to remove the high frequency/low energy turbulent content. Filtered yaw and tilt angle and shear exponent input characteristics are then translated into 1P and 2P periodic variations (higher harmonics could also be considered however their effect is expected to be small) of the flap angle of the three blades. The amplitude of the flap angle variation (1P and 2P) will be proportional to the load amplitude caused by the asymmetry of the inflow. Of course, load amplitude does not only depend on yaw and tilt angle but also on the wind speed. Therefore, a gain scheduling is applied based on the low pass filtered wind velocity. Flap angle variation should be imposed out of phase to load variation so as finally load variation is counter-acted. Look-up tables for the amplitude and phase of the flap angle variations (as functions of the wind velocity, yaw and tilt angle and shear exponent) are created through an automated tuning process described below which is based on deterministic runs over the whole range of operational wind speeds and combinations of yaw, tilt angles and shear exponents.

The feed-forward control strategy described above is illustrated in Figure 4.

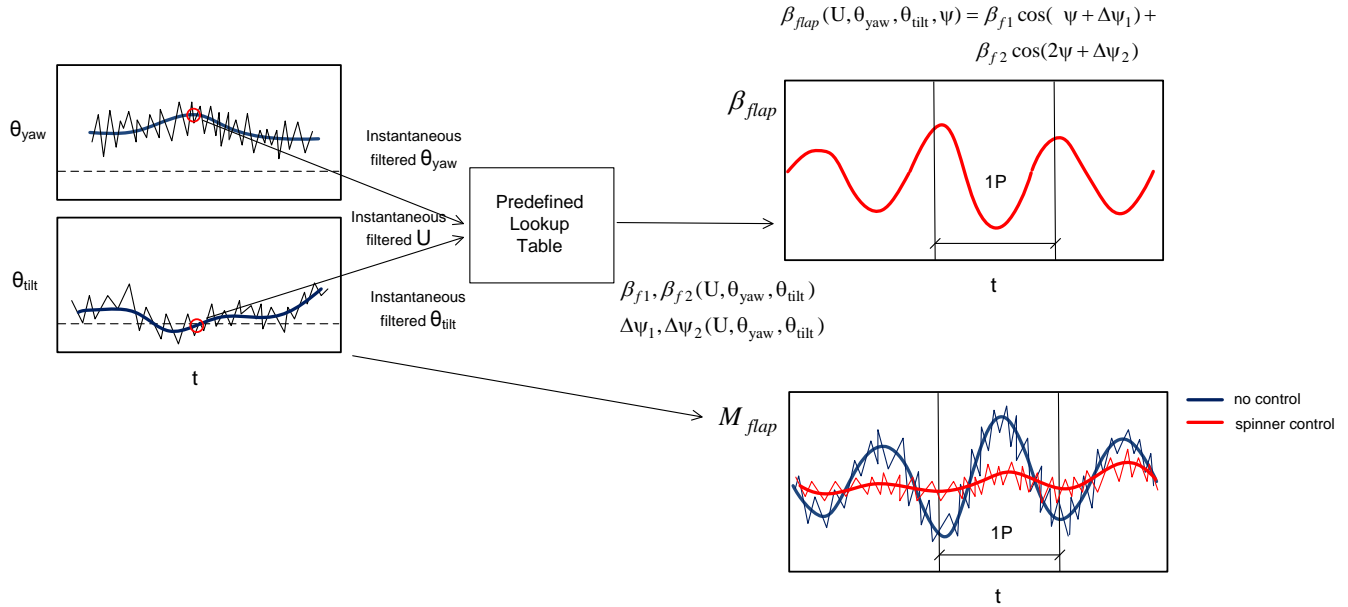


Figure 4. Description of control loop.

### Tuning of the spinner anemometer controller

The look-up tables for the amplitudes  $\beta_{f1}$  and  $\beta_{f2}$  and the phases  $\Delta\psi_1$  and  $\Delta\psi_2$  of the flap angle variation (as functions of the wind velocity, yaw and tilt angle and shear exponent) shown in Figure 4, have been generated through an automated tuning process illustrated in Figure 5. Tuning is performed through deterministic runs over the whole range of operational wind speeds and combinations of yaw, tilt angles and shear exponents. It is based on the standard individual feedback flap control (IFC) loop as the one employed in [2]. The blade root out-of-plane bending moment signals are transformed into yaw and tilt moments  $M_{yaw i}$  and  $M_{tilt i}$  by applying the Coleman transformation (1P and 2P):

$$\begin{Bmatrix} M_{tilt i} \\ M_{yaw i} \end{Bmatrix} = \begin{bmatrix} \frac{2}{3} \sin(i\psi_1) & \frac{2}{3} \sin(i\psi_2) & \frac{2}{3} \sin(i\psi_3) \\ \frac{2}{3} \cos(i\psi_1) & \frac{2}{3} \cos(i\psi_2) & \frac{2}{3} \cos(i\psi_3) \end{bmatrix} \begin{Bmatrix} M_{out1} \\ M_{out2} \\ M_{out3} \end{Bmatrix} \quad i = 1, 2 \quad (2)$$

where,  $\psi_k = \omega t + (k-1)\frac{2\pi}{3}$ ,  $k = 1, 3$



The yaw and tilt moment signals are then passed through an integral control element (I) and the cyclic  $\beta_{yaw i}$  and  $\beta_{tilt i}$  angles are obtained. These angles are then back transformed into flap angle amplitudes  $\beta_{f1}$  and  $\beta_{f2}$  and phases  $\Delta\psi_1$  and  $\Delta\psi_2$  of the individual blades' flap motion, via an inverse Coleman transformation. The flap motion of every blade is then obtained through:

$$\beta_{flap}^k = \beta_{f1} \cos(\psi_k + \Delta\psi_1) + \beta_{f2} \cos(2\psi_k + \Delta\psi_2) \quad , \quad k = 1,3$$

Trailing edge (TE) flap control is performed on the outer part of the blade of the DTU 10MW RWT. The blade of the reference turbine comprises FFA series airfoils. The relative thickness of the outer 35% of the blade is constant and equal to  $t/c=0.24$ . The camber line morphing shape presented in [3] is used. The flap extends to 30% of the section chord length. The spanwise extent of the flap is 34% of the blade radius. The basic characteristics of the flap are detailed in Table 2. Flap motion is bounded in the range  $[-10^0, +10^0]$ . In addition, saturation limits have been imposed on the velocity of the flap motion to 200/s. In all configurations a delay of 0.1 s has been imposed on the flap motion in order to account for the dynamics of the flap actuator (through a first order filter in flap response).

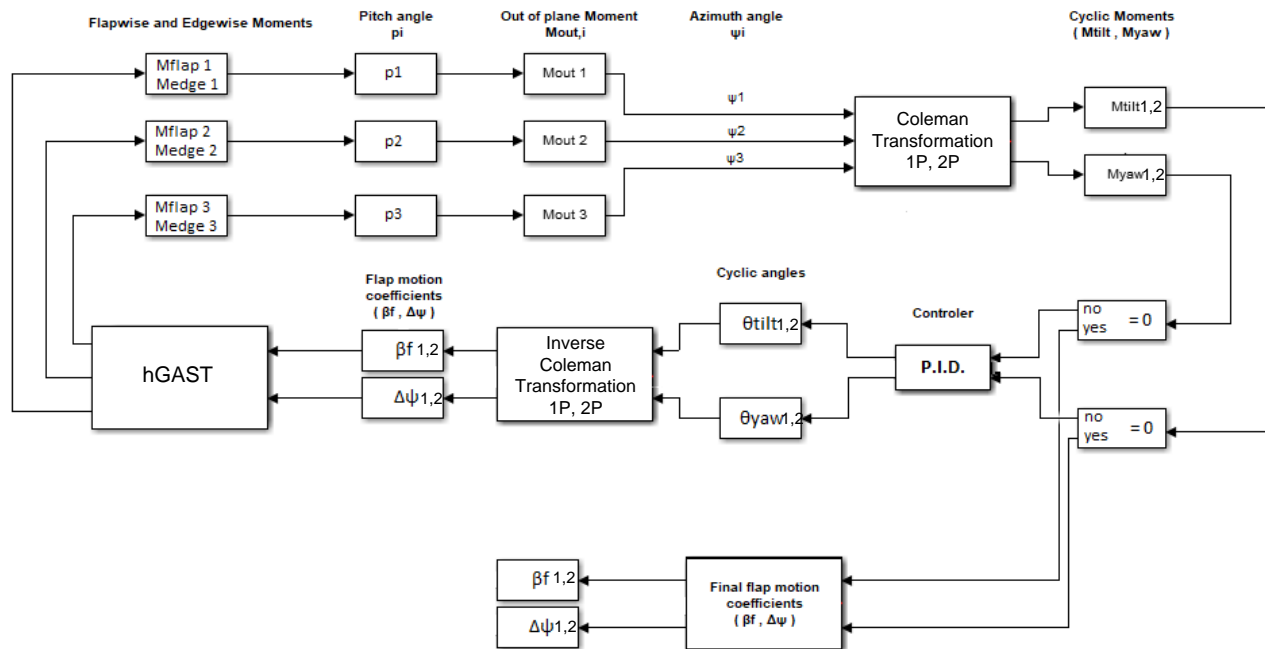


Figure 5. Description of the automated tuning process.



Table 2: TE flap layout.

Flap configuration	
	10MW RWT
Chordwise extent	30%
Deflection angle limits	$\pm 10^\circ$
Deflection speed limit	$20^\circ/s$
Spanwise length	30 m (~34% of blade length)
Spanwise location	55 m-85 m (from rotor centre)
Airfoil	FFA-W3-241

Examples of the maps produced for the amplitudes  $\beta_{f1}$  and  $\beta_{f2}$  and the phases  $\Delta\psi_1$  and  $\Delta\psi_2$  are presented in Figure 6-Figure 9 for the case of zero inclination angle and shear exponent 0.2.

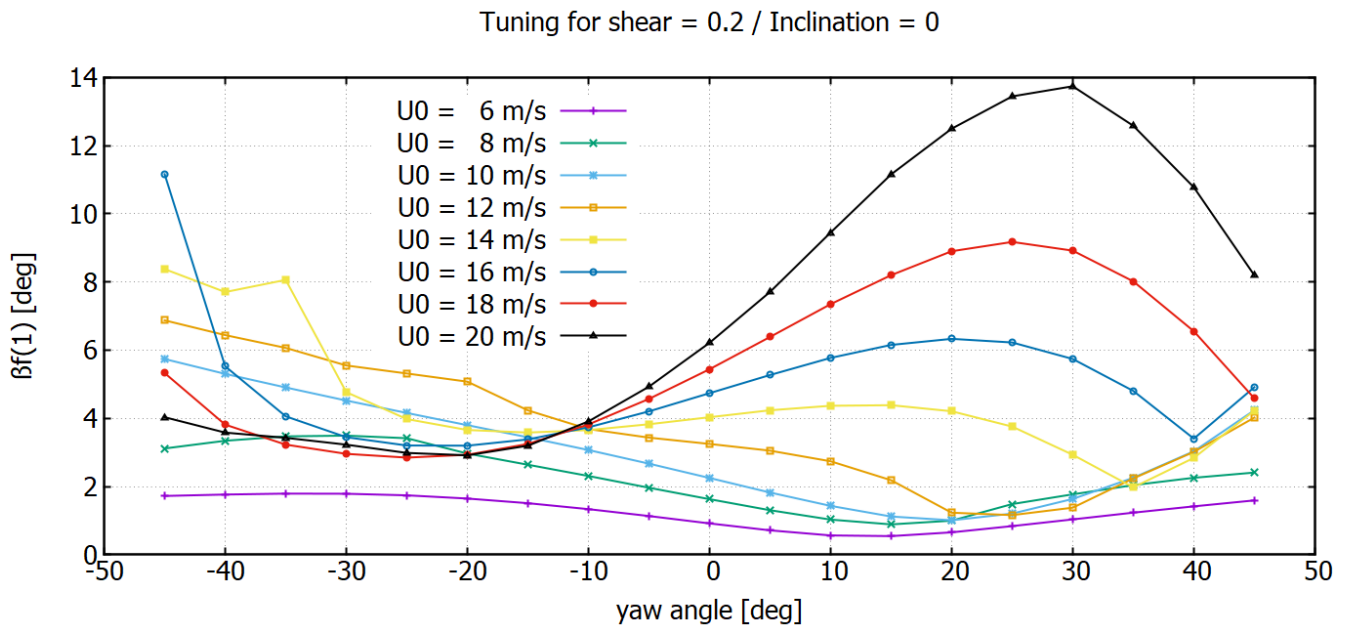


Figure 6. Map of  $\beta_{f1}$  for zero inclination angle and shear exponent 0.2.



Tuning for shear = 0.2 / Inclination = 0

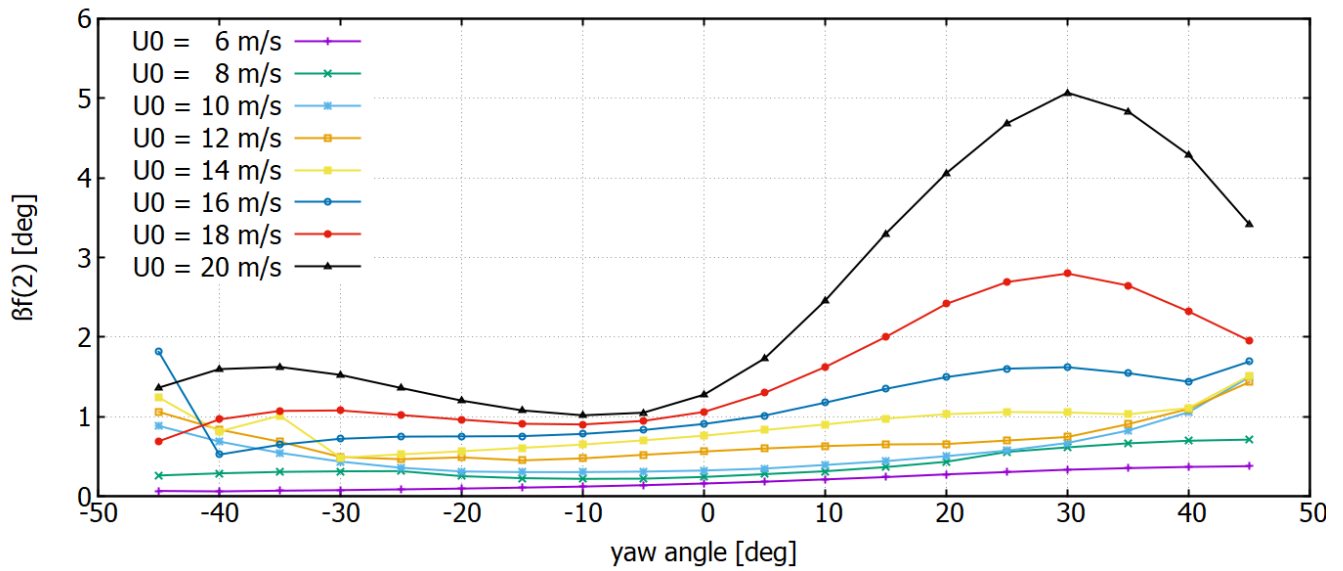


Figure 7. Map of  $\beta_{f2}$  for zero inclination angle and shear exponent 0.2.

Tuning for shear = 0.2 / Inclination = 0

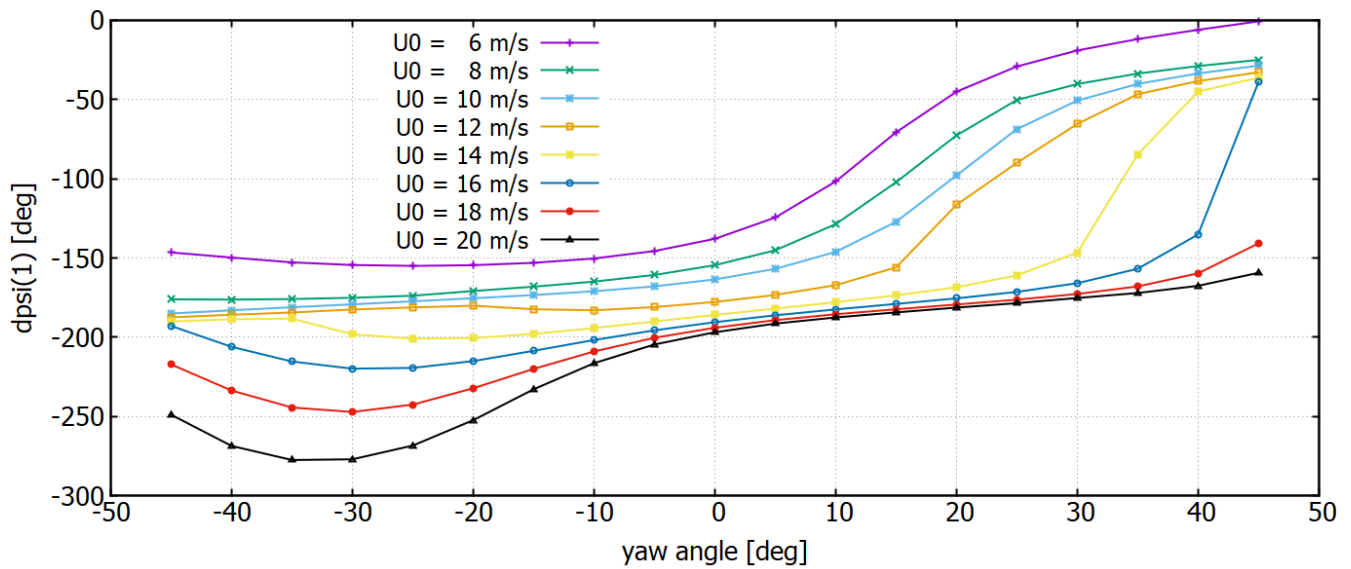


Figure 8. Map of  $\Delta\psi_1$  for zero inclination angle and shear exponent 0.2.



Tuning for shear = 0.2 / Inclination = 0

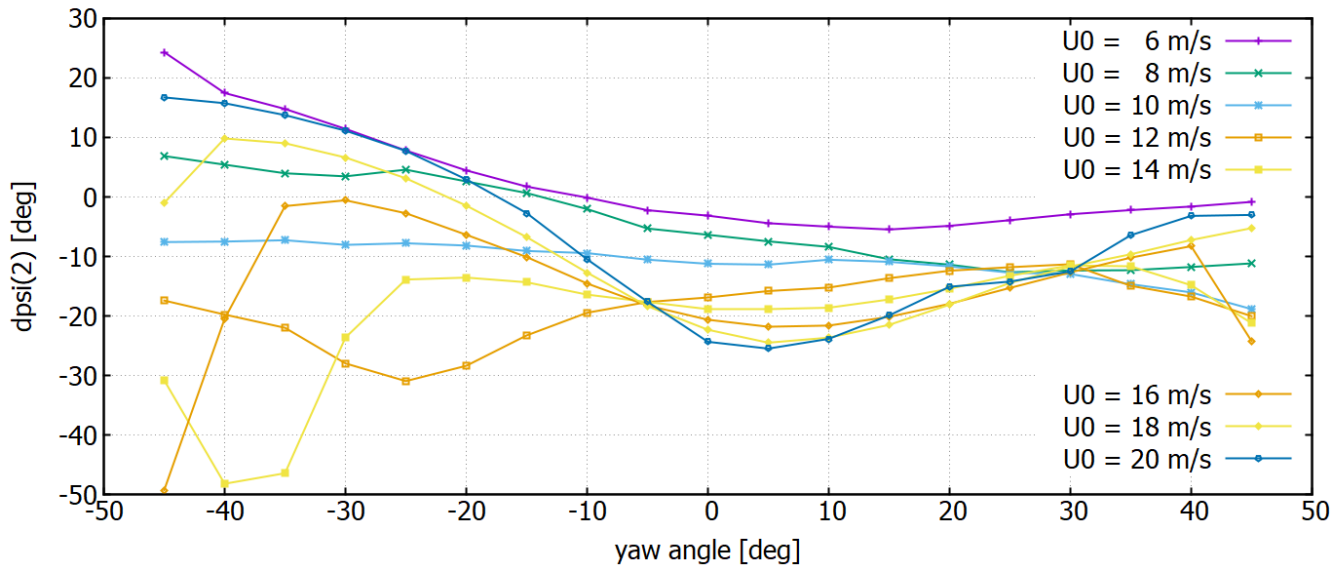


Figure 9. Map of  $\Delta\psi_2$  for zero inclination angle and shear exponent 0.2.

Figure 10 compares deterministic simulation results without flap control and with spinner anemometer 1P and combined 1P and 2P flap control. The plot presents out of plane blade root bending moment results at the wind speed of 16m/s for yaw angle of 30o and inclination angle of 0o. It is seen that 1P variation of the bending moment due to the effect of the yaw misalignment of the flow is substantially reduced when flap control is applied. Further reduction of the load amplitude is achieved when 2P flap control is superimposed on 1P control.

U<sub>0</sub> = 16 m/s - Yaw = 30 deg - Inclination = 0 deg

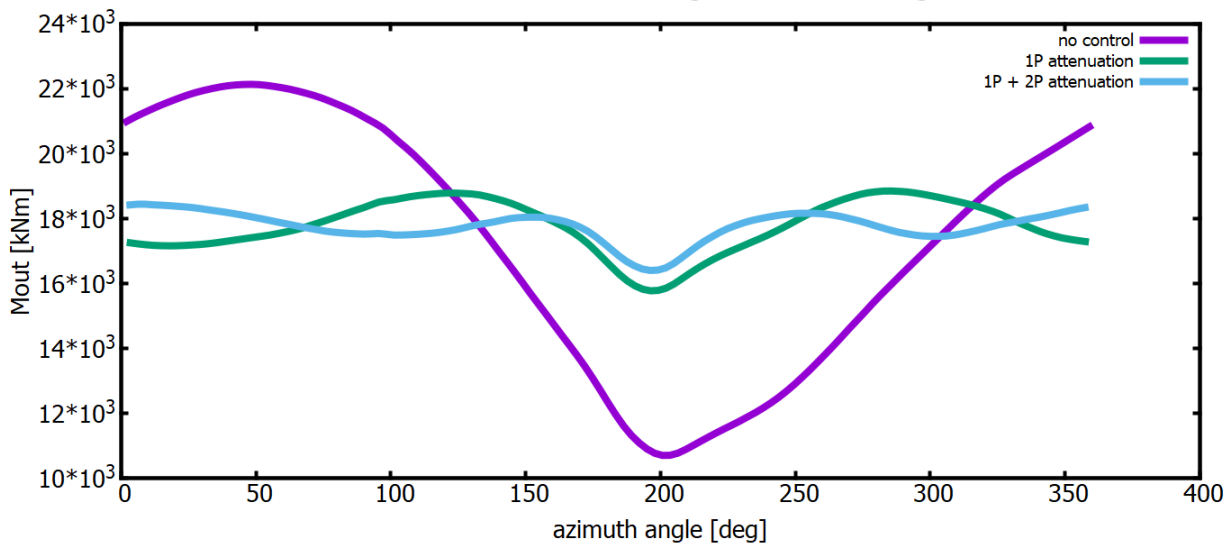


Figure 10. Effect of flap controller on out of plane moment variation at the wind speed of 16m/s and for yaw angle of 30°.

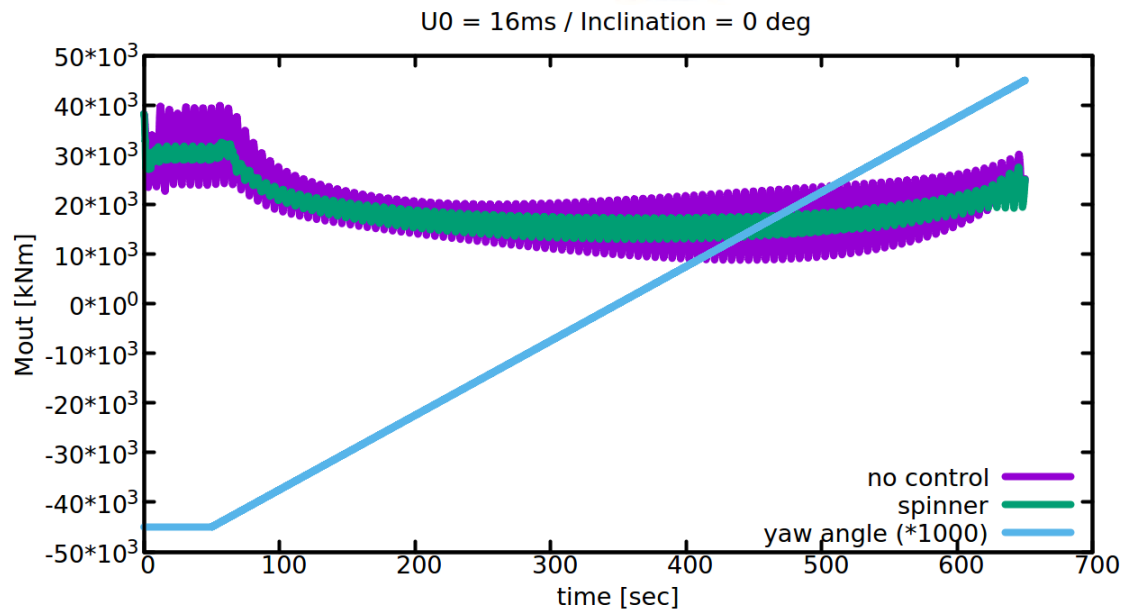


Figure 11. Effect of flap controller on out of plane moment variation at the wind speed of 16m/s and for a ramp variation of the yaw angle starting at  $-45^\circ$  and increasing up to  $+45^\circ$ .

In Figure 11 the effect of the spinner flap control on the amplitude of the out-of-plane blade root bending moment is shown for the case that yaw angle follows a ramp variation. Yaw angle starts at  $-45^\circ$  and linearly increases up to  $+45^\circ$ . It is seen that although the amplitude of  $M_{out}$  changes with the yaw angle when no control is applied, the amplitude of  $M_{out}$  remains almost constant when spinner flap control is applied.

### Results from application of the spinner anemometer controller on the DTU 10MW RWT mounted on DTU jacket

Assessment of load reduction capabilities of the proposed feed-forward control method is performed for the DTU 10MW RWT mounted on the DTU jacket. Both fatigue and ultimate loads are considered in the analyses. Fatigue loads are assessed on the basis of IEC DLC 1.2 (normal operation with normal turbulence conditions NTM and normal sea state NSS) while ultimate loads are estimated through DLC 1.3 (normal operation with extreme turbulence conditions ETM and NSS) and DLC 1.6 (NTM combined with severe sea state SSS). For all wind speeds simulations for yaw angles  $0^\circ$ ,  $+15^\circ$ , and  $-15^\circ$  are performed. Simulated conditions and wind speeds are summarized in Table 3. It is noted that for all wind speeds and yaw angles two turbulent seeds are simulated. In Table 4, wave characteristics (in terms of significant wave height  $H_s$  and peak spectral period  $T_p$ ) used in the simulations are provided for the different sea conditions and wind speeds.



For the IA 10MW RWT simulations are performed (a) for the baseline turbine without IPC and/or flap control (thereafter called “default”), (b) for the turbine with IPC only and (c) for the turbine with combined IPC& spinner anemometer based flap control (thereafter called “spinner”). The aim of the analysis is i) to assess load reduction capabilities of the combined pitch/flap control loop against pure IPC and ii) to assess pitch actuator duty cycle reduction for IPC as a result of the operation of the flaps. Lifetime fatigue loads are calculated assuming the following Weibull parameters:  $C=11$  m/s and  $k=2$ . Individual pitch or/and flap control is usually not recommended in the partial load region since the interaction of the pitch/flap controller with the basic power-speed controller could compromise power production. However, in order to assess load reduction capabilities at lower wind speeds in the present work pitch/flap operation has been also extended to wind speeds below rated.

Table 3: Simulated DLCs.

DLC	Definition	Bins [m/s]	Yaw(deg)
1.2	NTM, NSS	7, 11, 15, 19, 23	0, +-15
1.3	ETM, NSS	11	0, +-15
1.6	NTM, SSS	11	0, +-15

Table 4: Definition of sea state.

NSS		
U [m/s]	Hs [m]	Tp [s]
5.0	1.14	5.78
7.0	1.25	5.67
9.0	1.40	5.71
11.0	1.59	5.81
13.0	1.81	5.98
15.0	2.05	6.22
17.0	2.33	6.54
19.0	2.62	6.85
21.0	2.93	7.20
23.0	3.26	7.60
SSS		
	9.40	13.70



#### Fatigue loads (Table 5-Table 7)

- The percentage of reduction of the DEL of the flapwise bending moment is about the same for IPC and combined IPC&spinner flap control. Flapwise bending moment DEL reduction is about 25% at  $0^\circ$  yaw, 18% at  $+15^\circ$  yaw and 35% at  $-15^\circ$  yaw. Overall higher reduction rates are obtained with increasing wind speed.
- A slight reduction of 1-2% is also noted on the edgewise bending moment DEL.
- Blade torsion moment DEL significantly increases by spinner flap control. The rate of increase is lower (12.9%) at  $+15^\circ$  yaw and higher (100%) at  $-15^\circ$  yaw. Depending on the yaw angle, pure IPC has either neutral or decreasing effect on torsion moment. Maximum reduction of 19.3% is obtained at yaw  $-15^\circ$ . It is noted that TE flap motion locally increases twisting moment of the blade sections equipped with flaps.
- A slight increase in the tower fore-aft bending moment DEL is obtained both through IPC and combined IPC & spinner flap control. Both IPC and spinner flap control have been designed to reduce blade loads. So, no control logic exists in the design of the control loop that could effectively be used for the alleviation of the tower loads. However, the increase in the DEL of the fore-aft bending moment is rather marginal. It is about 1.5% at  $0^\circ$  yaw, increases to about 4% at  $-15^\circ$  yaw while it is almost negligible at  $+15^\circ$  yaw.
- A marginal increase is also noted on the side-side bending moment DEL
- Tower yawing moment decreases. Slightly higher load reduction rates are obtained through combined IPC & spinner anemometer input based flap control.
- As a result of the higher tower fatigue loads, increased DELs are obtained on the jacket structure (both at the base and the first level of X-braces above the base). Higher rates of load increase are obtained at X1. Interestingly, the rate of change of the combined moment at the base of the jacket is very low at  $0^\circ$  and  $+15^\circ$  yaw (both with IPC and spinner flap control) while a reduction of the combined moment is obtained at  $-15^\circ$  yaw (2.9% with IPC and 1.3% with combined IPC & spinner anemometer input based flap control).



Table 5: 10MW RWT at yaw angle 0°. Lifetime DELs (1Hz, m=10 for the blades, m=4 for the tower & jacket) calculated for C=11 m/s and k=2.

		YAW= 0deg																	
		07.00m/s			11.00m/s			15.00m/s			19.00m/s			23.00m/s			Overall		
		default	ipc	spinner	default	ipc	spinner	default	ipc	spinner	default	ipc	spinner	default	ipc	spinner	default	ipc	spinner
ROOT BLADE	edge (kNm)	23466	-2.4%	-2.2%	25998	-3.4%	-2.9%	26111	-1.2%	-1.3%	26865	-0.1%	-0.6%	27909	0.4%	0.3%	25890	-1.0%	-1.1%
	flap (kNm)	10359	-8.5%	-11.8%	26300	-16.9%	-16.9%	30108	-27.5%	-26.0%	33691	-28.4%	-27.0%	37844	-25.0%	-24.3%	31238	-26.0%	-25.2%
	torsion (kNm)	303	-8.1%	1.2%	409	-11.4%	26.8%	460	-13.3%	47.6%	495	-9.3%	69.1%	550	-7.7%	67.1%	465	-9.5%	66.2%
BASE TOWER	side (kNm)	8670	2.1%	2.5%	6746	-6.3%	-3.6%	12534	-3.0%	-3.0%	19666	1.3%	0.8%	28199	2.4%	3.0%	16734	1.7%	1.4%
	fore (kNm)	27355	-2.5%	-2.7%	58362	-0.9%	-1.7%	51998	4.0%	4.3%	55441	2.3%	2.7%	62822	3.2%	3.7%	50955	1.5%	1.6%
	yaw (kNm)	7673	-3.6%	-2.8%	15309	-4.0%	-5.2%	22016	-1.4%	-2.4%	26755	-0.2%	-0.8%	31318	1.5%	0.2%	22191	0.0%	-1.2%
JACKET BASE	Fz (kN)	1243	-0.2%	-0.4%	2382	-0.6%	-1.3%	2376	2.5%	2.1%	2734	2.8%	2.0%	3242	3.3%	2.5%	2380	2.1%	1.3%
	Mx (kNm)	173	1.0%	0.7%	335	-1.0%	-4.3%	410	3.3%	2.6%	490	3.7%	3.0%	580	3.7%	2.3%	413	3.2%	2.2%
	Mcomb (kNm)	260	-2.0%	-0.7%	472	-3.3%	-2.2%	649	-0.1%	0.0%	792	0.3%	0.5%	912	1.9%	1.9%	653	0.4%	0.4%
JACKET XI	Fz (kN)	114	-0.2%	-0.4%	238	-3.3%	-5.3%	326	0.9%	0.0%	394	1.4%	1.3%	468	1.7%	0.9%	329	1.3%	0.6%
	Mx (kNm)	3	0.0%	-0.4%	6	0.1%	0.1%	6	3.9%	4.2%	7	4.0%	3.4%	9	3.1%	3.1%	6	3.0%	2.8%
	Mcomb (kNm)	6	2.1%	0.3%	10	0.0%	0.2%	15	1.4%	1.2%	19	2.5%	1.0%	24	3.8%	3.1%	16	2.6%	1.5%

Table 6: 10MW RWT at yaw angle +15°. Lifetime DELs (1Hz, m=10 for the blades, m=4 for the tower & jacket) calculated for C=11 m/s and k=2.

		YAW= 15deg																	
		07.00m/s			11.00m/s			15.00m/s			19.00m/s			23.00m/s			Overall		
		default	ipc	spinner	default	ipc	spinner	default	ipc	spinner	default	ipc	spinner	default	ipc	spinner	default	ipc	spinner
ROOT BLADE	edge (kNm)	23268	-1.8%	-1.7%	25778	-2.8%	-3.1%	25898	0.2%	-0.8%	26489	1.2%	-0.3%	27787	1.6%	0.2%	25608	0.1%	-0.9%
	flap (kNm)	9975	-11.0%	-14.2%	24416	-15.0%	-14.6%	28766	-22.3%	-21.5%	30220	-20.5%	-18.8%	31957	-12.2%	-10.9%	28279	-18.8%	-17.9%
	torsion (kNm)	303	-7.3%	1.6%	383	-8.5%	19.3%	429	-5.7%	16.9%	449	2.0%	12.7%	500	4.8%	6.5%	426	0.9%	12.9%
BASE TOWER	side (kNm)	8921	5.0%	6.4%	6877	-3.1%	-4.8%	12302	-3.6%	-3.3%	18931	1.1%	0.4%	27160	0.8%	0.4%	16249	0.5%	0.0%
	fore (kNm)	26860	-1.4%	-1.4%	57697	-2.8%	0.2%	59526	-0.9%	0.5%	61099	1.5%	0.9%	69642	2.0%	1.0%	54702	-0.4%	0.0%
	yaw (kNm)	7264	-2.7%	-2.4%	14339	-3.7%	-5.7%	21983	-2.6%	-4.1%	27107	-1.2%	-3.7%	31940	-0.4%	-3.7%	22415	-1.2%	-4.0%
JACKET BASE	Fz (kN)	1225	0.5%	0.4%	2366	-1.9%	-0.5%	2613	0.0%	-0.1%	2908	3.1%	0.8%	3522	2.2%	0.6%	2512	1.4%	0.3%
	Mx (kNm)	169	2.0%	2.0%	307	3.1%	1.9%	400	7.9%	6.4%	480	5.5%	4.8%	587	4.7%	2.8%	405	5.5%	4.3%
	Mcomb (kNm)	259	-1.8%	-1.2%	457	-4.3%	-2.2%	654	-1.3%	-1.7%	787	1.2%	-0.3%	934	1.9%	-0.4%	656	0.8%	-0.7%
JACKET XI	Fz (kN)	109	0.0%	0.7%	217	-0.4%	-2.7%	316	3.1%	1.5%	388	2.1%	0.6%	468	1.3%	-1.2%	323	2.0%	0.0%
	Mx (kNm)	3	-0.2%	-0.3%	6	-1.9%	-0.1%	7	0.0%	0.7%	8	3.0%	1.9%	9	2.9%	1.9%	7	1.6%	1.2%
	Mcomb (kNm)	6	5.9%	4.9%	9	0.1%	-1.0%	15	1.6%	1.5%	19	3.3%	2.0%	24	3.8%	2.6%	16	3.2%	1.9%



Table 7: 10MW RWT at yaw angle -15°. Lifetime DELs (1Hz, m=10 for the blades, m=4 for the tower & jacket) calculated for C=11 m/s and k=2.

		YAW=-15deg																	
		07.00m/s			11.00m/s			15.00m/s			19.00m/s			23.00m/s			Overall		
		default	ipc	spinner	default	ipc	spinner	default	ipc	spinner	default	ipc	spinner	default	ipc	spinner	default	ipc	spinner
ROOT BLADE	edge (kNm)	23383	-2.0%	-1.8%	26554	-3.5%	-2.3%	26474	-2.6%	-1.8%	27229	-1.6%	-0.3%	28586	-1.4%	-0.3%	26244	-2.2%	-1.2%
	flap (kNm)	9676	-4.8%	-6.1%	26275	-20.2%	-22.7%	32177	-31.0%	-28.2%	38123	-36.9%	-34.8%	45572	-37.7%	-37.7%	35852	-35.7%	-34.5%
	torsion (kNm)	307	-6.7%	1.5%	407	-12.0%	46.7%	506	-19.8%	82.1%	570	-20.5%	103.5%	641	-18.7%	98.7%	531	-19.3%	100.3%
BASE TOWER	side (kNm)	9111	2.4%	0.8%	7306	-6.8%	-5.2%	12388	-1.3%	-0.6%	18995	1.6%	3.2%	28735	0.4%	-1.3%	16470	0.7%	1.0%
	fore (kNm)	25949	-0.3%	-1.6%	54147	2.8%	1.7%	51038	8.3%	6.6%	53448	3.1%	5.8%	61013	2.7%	3.0%	48751	3.8%	4.0%
	yaw (kNm)	7363	-2.0%	-2.5%	14708	-3.6%	-4.5%	21512	-0.3%	-0.8%	26661	-0.9%	-0.2%	31195	2.6%	2.5%	22050	-0.4%	-0.4%
JACKET BASE	Fz (kN)	1180	0.8%	-0.1%	2251	2.0%	0.4%	2292	7.1%	5.3%	2553	3.3%	4.3%	3080	1.9%	0.2%	2250	3.4%	2.9%
	Mx (kNm)	170	0.9%	0.1%	320	0.2%	-2.9%	416	2.8%	1.7%	493	3.2%	2.6%	583	3.7%	2.4%	414	2.9%	1.8%
	Mcomb (kNm)	220	0.5%	-0.4%	383	1.4%	0.4%	461	-0.4%	0.1%	557	-3.6%	-2.3%	670	-4.7%	-1.4%	470	-2.9%	-1.3%
JACKET XL	Fz (kN)	112	-0.4%	-0.8%	231	-3.8%	-5.5%	327	0.3%	-0.3%	399	0.4%	0.9%	466	3.2%	3.0%	331	0.8%	0.6%
	Mx (kNm)	3	1.5%	1.2%	6	2.0%	0.8%	6	7.6%	6.4%	7	4.9%	5.1%	8	2.5%	1.9%	6	4.4%	4.1%
	Mcomb (kNm)	6	2.4%	0.3%	9	0.2%	1.8%	15	0.7%	0.8%	19	1.4%	0.6%	24	1.6%	0.2%	16	1.0%	0.6%

### Ultimate loads (Table 8)

- Extreme flapwise bending moment decreases both with IPC and combined IPC & spinner based flap control. A slightly higher reduction of the maximum flapwise moment (maximum moment is the ultimate design moment in this case) is obtained through combined IPC & spinner flap control (3.8% reduction through spinner flap against 2.7% reduction with pure IPC). It is noted that driving DLC for the flapwise bending moment is DLC 1.3.
- A 6% reduction of the maximum (ultimate load) edgewise bending moment is obtained both with IPC and combined pitch/flap control.
- A significant torsion moment increase (both min and max) is obtained through spinner flap control. This is again due to the twisting moment induced by flap motion.
- Overall the combined blade moment decreases. A 3.6% reduction is obtained through combined IPC & spinner flap and 2.8% reduction through pure IPC.
- Maximum tower base fore-aft moment slightly decreases. Higher rate of load reduction (2.4%) is again obtained through combined IPC & spinner flap control.
- Ultimate tower base side-side and yaw moments significantly decrease
- An overall reduction of the combined tower base moment of 2.4% is obtained through combined IPC & spinner flap control. In case of pure IPC the load reduction rate is 0.5%. It is seen that combined tower base moment is essentially driven by fore-aft component. The rates of combined tower moment reduction are exactly the same with those of the tower fore-aft moment component.



- A 2.3% reduction of the jacket X1 combined moment is obtained through IPC & spinner flap control. Pure IPC leads to 2.4% higher combined moment.
- A 2.1% reduction of the jacket base combined moment is obtained through combined IPC & spinner flap. A slightly lower load reduction (0.9%) is attained through IPC. As in the case of the flapwise bending moment, tower and jacket design loads are driven by high turbulence levels (design DLC 1.3).

Table 8: 10MW RWT. Min-max loads – Min and Max loads of the fatigue DLC 1.2 are also included.

		DLC 1-2			DLC 1-3			DLC 1-6			Overall			
		default	ipc	spinner										
ROOT BLADE	edge (kNm)	max	25703	-6.0%	-4.4%	33512	-5.9%	-6.0%	27198	-5.2%	-5.3%	33512	-5.9%	-6.0%
		min	-22061	4.1%	2.5%	-24760	-6.0%	-7.4%	-18429	-4.1%	-6.6%	-24760	-6.0%	-7.4%
	flap (kNm)	max	56379	-4.3%	-4.4%	67349	-2.7%	-3.8%	60687	-4.4%	-4.3%	67349	-2.7%	-3.8%
		min	-38043	-59.1%	-53.4%	-23854	-88.1%	-87.3%	-2687	-390.5%	-357.2%	-38043	-59.1%	-53.4%
	torsion (kNm)	max	438	-8.5%	95.2%	584	-3.8%	79.4%	478	-9.5%	44.3%	584	-3.8%	79.4%
combined (kNm)	min	-709	-1.8%	70.0%	-591	-6.1%	91.3%	-431	-17.8%	33.7%	-709	-1.8%	70.0%	
BASE TOWER	side (kNm)	max	71832	-23.4%	-23.9%	40694	-20.6%	-24.1%	31614	-20.7%	-20.0%	71832	-23.4%	-23.9%
		min	-26668	-28.6%	-28.0%	640	19.8%	-721.7%	6961	-28.9%	-13.0%	-26668	-28.6%	-28.0%
	fore (kNm)	max	249051	-2.7%	-2.0%	299097	-0.5%	-2.4%	266176	-1.0%	-0.7%	299097	-0.5%	-2.4%
		min	-25367	26.1%	26.1%	-8592	89.3%	134.2%	65188	-1.8%	-6.1%	-25367	26.1%	26.1%
	yaw (kNm)	max	39032	-19.4%	-18.5%	33725	-30.2%	-30.2%	22091	-34.3%	-32.3%	39032	-19.4%	-18.5%
combined (kNm)	min	-44064	-23.4%	-23.8%	-30963	-25.4%	-27.8%	-18090	-10.6%	-13.0%	-44064	-23.4%	-23.8%	
JACKET BASE	Fz (kN)	max	-3862	1.2%	1.4%	-5116	-0.3%	-3.5%	-8167	-1.6%	-3.2%	-3862	1.2%	1.4%
		min	-15130	-1.3%	-0.5%	-17571	-0.4%	-0.2%	-16817	-0.2%	-1.7%	-17571	-0.4%	-0.2%
	Mx (kNm)	max	1536	1.0%	1.0%	1866	2.6%	0.3%	1703	2.0%	2.7%	1866	2.6%	0.3%
		min	148	-75.0%	-2.1%	381	-0.5%	12.7%	646	8.6%	9.9%	148	-75.0%	-2.1%
	Mz (kNm)	max	1784	-1.2%	-1.4%	2098	-3.7%	-4.6%	2066	-1.9%	-1.4%	2098	-3.4%	-2.9%
min		-351	-68.5%	-36.6%	129	16.2%	-72.3%	427	27.6%	31.0%	-351	-68.5%	-36.6%	
Mcomb (kNm)	max	2213	-1.8%	-1.1%	2627	-0.9%	-2.1%	2575	0.1%	-2.6%	2627	-0.9%	-2.1%	
JACKET X1	Fz (kN)	max	263	-37.6%	-45.4%	97	-133.2%	-168.8%	-105	101.0%	87.8%	263	-37.6%	-45.4%
		min	-929	-10.7%	-9.3%	-932	-5.1%	-9.5%	-768	-1.4%	-3.9%	-932	-5.1%	-9.5%
	Mx (kNm)	max	34	-2.0%	-1.3%	40	-0.2%	-0.1%	37	0.2%	-0.4%	40	-0.2%	-0.1%
		min	8	-6.7%	-6.4%	10	-5.8%	-13.3%	17	-0.9%	-4.1%	8	-6.7%	-6.4%
	Mz (kNm)	max	21	5.6%	7.1%	18	-14.5%	-19.8%	45	2.5%	-3.1%	45	2.5%	-3.1%
min		-19	16.3%	14.7%	-13	0.2%	1.9%	-38	-4.7%	-4.2%	-38	-4.7%	-4.2%	
Mcomb (kNm)	max	34	-1.5%	-0.7%	40	0.7%	0.0%	56	2.4%	-2.3%	56	2.4%	-2.3%	

- In Figure 12 and Figure 13 the flap and pitch motion characteristics of the different control strategies are presented for the NTM conditions. When combined IPC & spinner based flap



control is applied, the flap motion reaches the saturation limit of +10° only at wind speeds higher than 15m/s (see Figure 12). The standard deviation (SDV) of the flap angle is significantly lower than the limit angle of 10° (goes up to 4.5°) indicating that flap motion stays well below the limit angles most of the time and rarely hits the upper bound.

- In Figure 13 the SDV of the pitch motion is shown for all control strategies. It is seen that the SDV of the pitch motion in the full load region increases by more than 50% when pure IPC is applied as compared to the “default” case (no load control). When spinner based flap control is combined with IPC the rate of increase of the pitch motion with respect to the “default” case is almost half that of the pure IPC. So, a significant saving of the duty cycle of the pitch actuator is achieved when spinner anemometer based flap control is engaged.

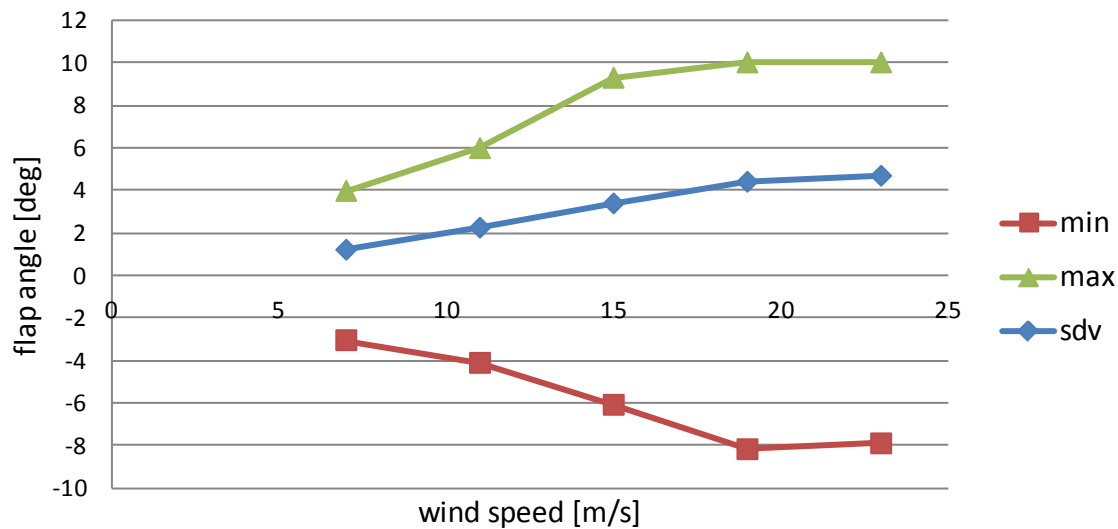


Figure 12. 10MW RWT. Flap angle variation.

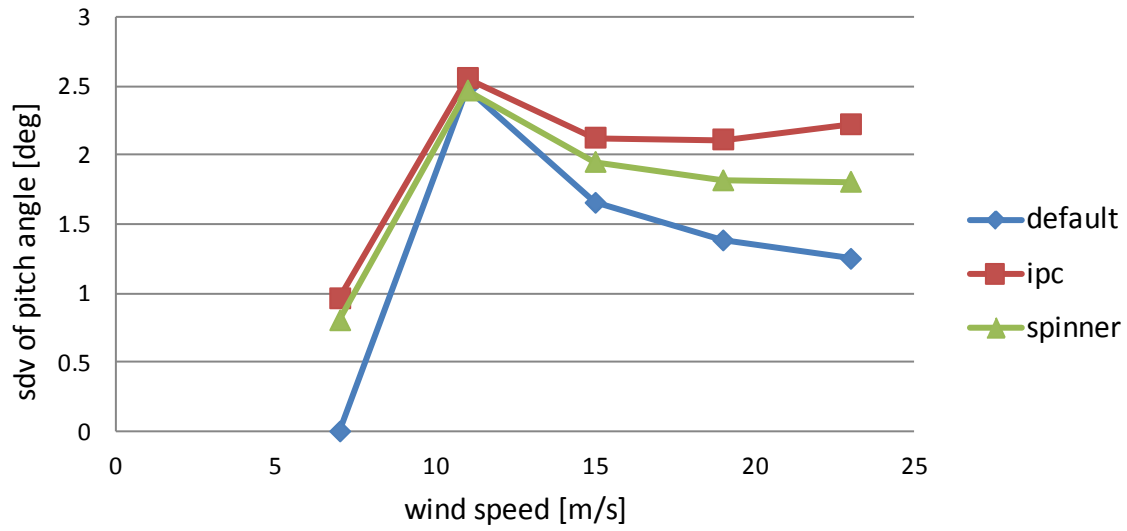


Figure 13. 10MW RWT. Pitch angle variation.



## Comparison of Individual Pitch Control and Individual Pitch + Flap Control on INN WIND 10 MW RWT (DNV GL (UK))

### Background

Distributed actuation devices that alter the aerodynamic profile of a turbine blade have been studied extensively in literature with application to wind turbine load reduction [1]. A study into several concepts of distributed control devices was conducted in [2], [3] for the INN WIND.EU project and have shown that trailing edge flaps (TEFs) present the highest TRL

When normalised for actuation levels, TEFs have shown similar fatigue load reduction potential to using individual pitch control (IPC) alone [1], when using similar algorithms to facilitate the load reductions. The limits of IPC actuation levels are typically driven by pitch acceleration limits and the stall margin of the blade under operation. If the angle of attack is increased too far a blade can enter stall. Combine IPC with flap actuation, some additional actuation may be possible if the superimposition of IPC and individual flap control (IFC) does not drive the blade into stall.

As blades become larger, with increased pitching inertia's and friction levels, the requirements on pitch systems can also increase. If TEFs can be used to reduce pitch activity, and at the same time provide the replacement actuation at lower costs there is a pathway to reductions in LCoE. TEFs provide this pathway as a smaller section of the blade is actuated. Another concern with IPC actuation is the constant cycling of pitch angle over a narrow range causing uneven wear in the pitch bearing and ring gear. If this cycling were passed on to a dedicated actuator such as a TEF, the actuation mechanism can be designed to be fully utilised with even wear leading to a more efficient mechanical design. Beyond fatigue loading TEFs also have the potential to assist in extreme load reduction by providing additional actuation during turbine failures.

In this work, we demonstrate a methodology of replacing individual pitch actuation with individual flap actuation for load reduction of wind turbines. We begin by comparing the spectral and time series differences when using IFC and IPC to indicate the characteristics that can be exploited in each case. We demonstrate the extent to which IPC can be augmented with IFC for a specific TEF configuration and maintain or improve load reduction capabilities. This is verified by application to the INN WIND 10 MW Reference wind turbine over a significant set of IEC design load calculations [4].

### Modelling of the 10 MW Reference Turbine with Flaps

#### *Simulation and Analysis Tools*

Investigations have been conducted using Bladed 4.8, a validated multi-body wind turbine simulation code. Bladed 4.8 uses blade element and momentum theory to model blade aerodynamics, with the Øye dynamic wake model, the Glauert skew wake model and the Incompressible Beddoes-Leishman dynamic stall model. Flaps are defined as changes to the lift, drag and moment curves, as a function of



flap deployment angle for the blade stations containing the active flap. Flap deployment can also be defined with linear dynamics from flap angle demand to flap angle position.

As indicated in [2], Bladed does not consider unsteady flow over the flap sections, but the assumption has been made that the frequency of actuation is low enough that unsteady effects do not dominate the response. The reader is referred to [2] for a more complete review of the flap modelling performance of a range of engineering codes against CFD models. In that report it was concluded that the results by Bladed acceptable for analysing load reduction potential or active flaps.

#### *Reference 10 MW*

The turbine is modelled based on data supplied in [5]–[7] for the turbine and [8] for the reference jacket. The structural model is approximated with:

- 10 modes on each blade;
- 15 support structure modes;
- one drivetrain flexibility; and
- Constrained linear actuator dynamics.

Frequency and damping ratios for the uncoupled blade and support structure modes are given in Table 8 and Table 9 respectively, and a Campbell diagram of the aero-elastically coupled modes is given in Figure 14.

**Table 9 Uncoupled Blade Modes of 10 MW Reference Turbine**

Damping Ratio (%)	Mode	Frequency (Hz)
0.48	1st flapwise mode	0.62
0.48	1st edgewise mode	0.94
1.34	2nd flapwise mode	1.75
1.41	2nd edgewise mode	2.79
2.7	3rd flapwise mode	3.59
3.3	3rd edgewise mode	5.71
4.2	4th flapwise mode	6.11
0.8	1st torsional mode	6.54
Frequency proportional	5th flapwise mode	8.90
Frequency proportional	4th edgewise mode	9.86

**Table 10 Uncoupled Support Structure Modes of 10 MW Reference Turbine**

Damping Ratio (%)	Mode	Frequency (Hz)
1	1st side-side mode	0.29



1	1st fore-aft mode	0.30
1	1st torsional mode	1.07
1	2nd side-side mode	1.52
1	3rd side-side mode	1.76
1	2nd fore-aft mode	1.76
1	3rd fore-aft mode	1.78
1	4th side-side mode	2.14
1	4th fore-aft mode	2.88
1	5th side-side mode	2.88
1	6th side-side mode	3.17
1	5th fore-aft mode	3.74
1	6th fore-aft mode	3.81
1	7th fore-aft mode	3.92
1	7th side-side mode	3.92

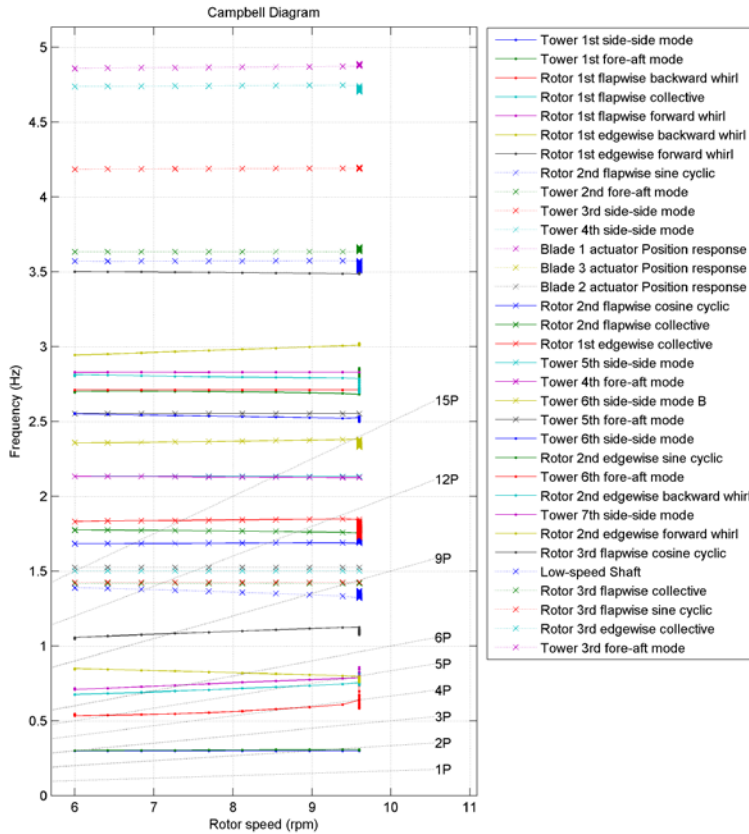


Figure 14: Campbell diagram for the 10 MW RWT

The characteristics of the trailing-edge flap model used for this study are summarised in Table 10.

Table 11 Flap configuration for 10 MW Reference Turbine

Flap configuration	
Chordwise extension	30%
Deflection angle limits	$\pm 10^\circ$
Spanwise length	10 m
Spanwise location	75.00 m – 84.87 m (from blade root)
Airfoil	FFA-W3-241
Deflection rate limit	100°/s
Actuator time constant	0.1 s



## Blade root load and blade tip deflection comparison

TEF actuation and blade pitching have subtle differences in their impacts on blade root loading and blade tip deflections. In Figure 15 we can see the time series response of the blade root loading and blade tip deflection when subjected to pitching at 1P, flapping at 1P and pitching + flapping at 1P in steady wind. Note that the magnitude of results will change depending on the wind speed, but trends will remain similar. We can see that when pitch and flap actuation levels are the same, the out-of-plane (OOP) loading ( $M_y$  direction) is significantly lower for the TEF system as expected, however the blade tip OOP deflections are much closer in magnitude. This indicates that flaps could reduce tip-to-tower clearance (TTC); conversely, if a designed carefully and with appropriate feedback, the blade tip path could be guided to increase TTC with less impact on blade root loads. The latter is not considered in this work. The in-plane loading is almost identical when pitching or flapping, but the blade tip deflections are again larger with flapping. In the blade-torsional direction ( $M_z$ ) the loading levels are very similar; while the blade tip twist is similar for both systems. The response with both pitching and flapping together has been created with the pitch and flapping phase corrected so that the influence of the pitching and flapping actions is in-phase. The response is more like the pitching only response, but with larger magnitudes. This is important because it shows that when the pitching and flapping are applied together with the correct phase corrections, the total response is 'clean' and can be applied with little modification of existing algorithms. We can see in Figure 16 that the spectral response of each actuation method follows almost identical trends, we would then expect that for a given control algorithm, an identical filtering can be applied regardless of actuation method.

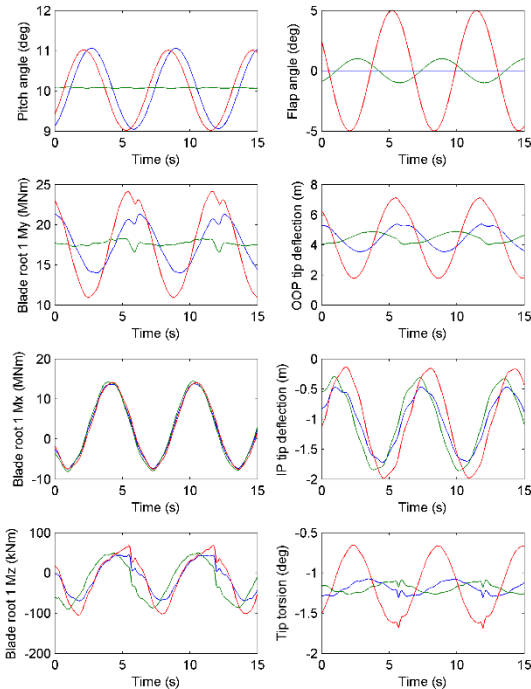


Figure 15: Time series response to 1P pitching - blue; 1P flapping - green and 1P pitching and flapping - red.

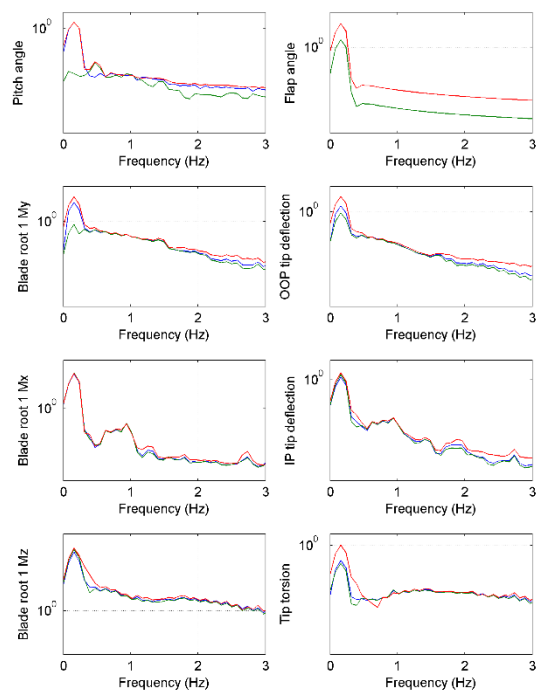


Figure 16: Spectral response to 1P pitching - blue; 1P flapping - green and 1P pitching and flapping - red.

The responses to 2P pitching, flapping and pitching + flapping are shown in Figure 17 and Figure 18. The key differences can be seen in the frequency domain, which shows that the loading and displacement responses are more concentrated when using flaps versus using pitch.

Overall, the blade root loading trends are very similar between blade flapping and pitching with the key difference being that the flap actuator must actuate to much larger angles than blade pitching. The displacement response is much closer for blade pitching and blade flapping showing that for a given load, the displacement of the blade tip for flapping control will be much higher than for pitching control. From a loading perspective, we should be able to use the algorithm structures that have been successful for IPC in IFC. In addition, by applying the appropriate phase correction, it is possible to use IPC and IFC together without introducing any harmful characteristics into the loading and displacement responses.

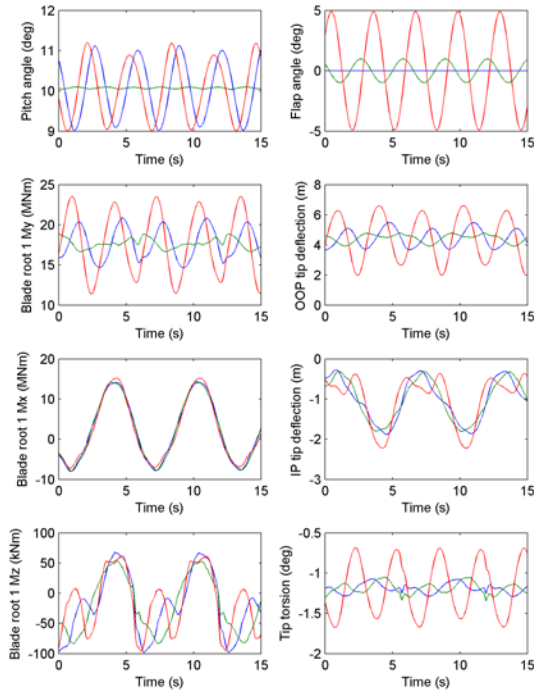


Figure 17: Time series response to 2P pitching - blue; 2P flapping - green and 1P pitching and flapping - red.

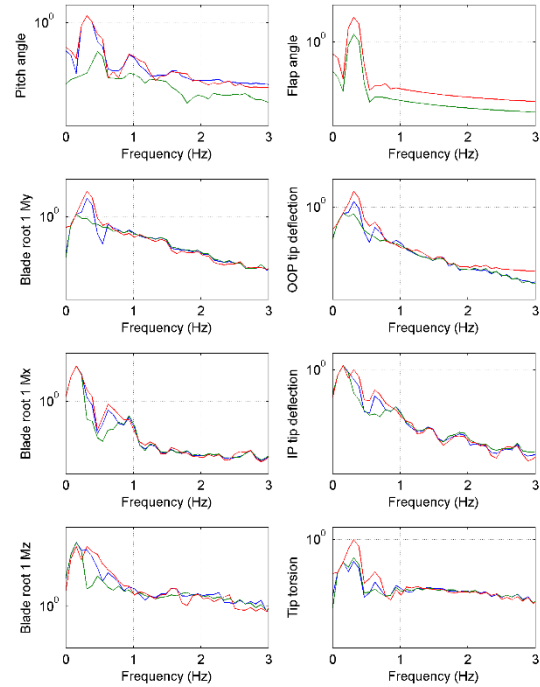


Figure 18: Spectral response to 2P pitching - blue; 2P flapping - green and 2P pitching and flapping - red.

## Control Design

The IPC and IFC algorithms in this work operate under the structure shown in Figure 19. This implementation makes use of the d-q axis transform (also referred to as the multi-blade coordinate transformation and Coleman transformation) [9]. In this structure, each blade is pitched cyclically as a function of azimuth angle, with amplitude defined as a function of the blade root loading. This structure decouples the individual pitch activity from collective pitch activity; which in turn limits impacts on power control and collective pitch damping loops such as tower dampers. The structure also allows the targeting of blade damage at rotor speed harmonic frequencies which account for a significant portion of the blade fatigue loading. For this investigation, two harmonics are targeted, 1P and 2P, as they account for most damage accumulation. However, higher order transforms are possible to apply in principle and may be very suitable for application to TEF actuators which can deploy very quickly.

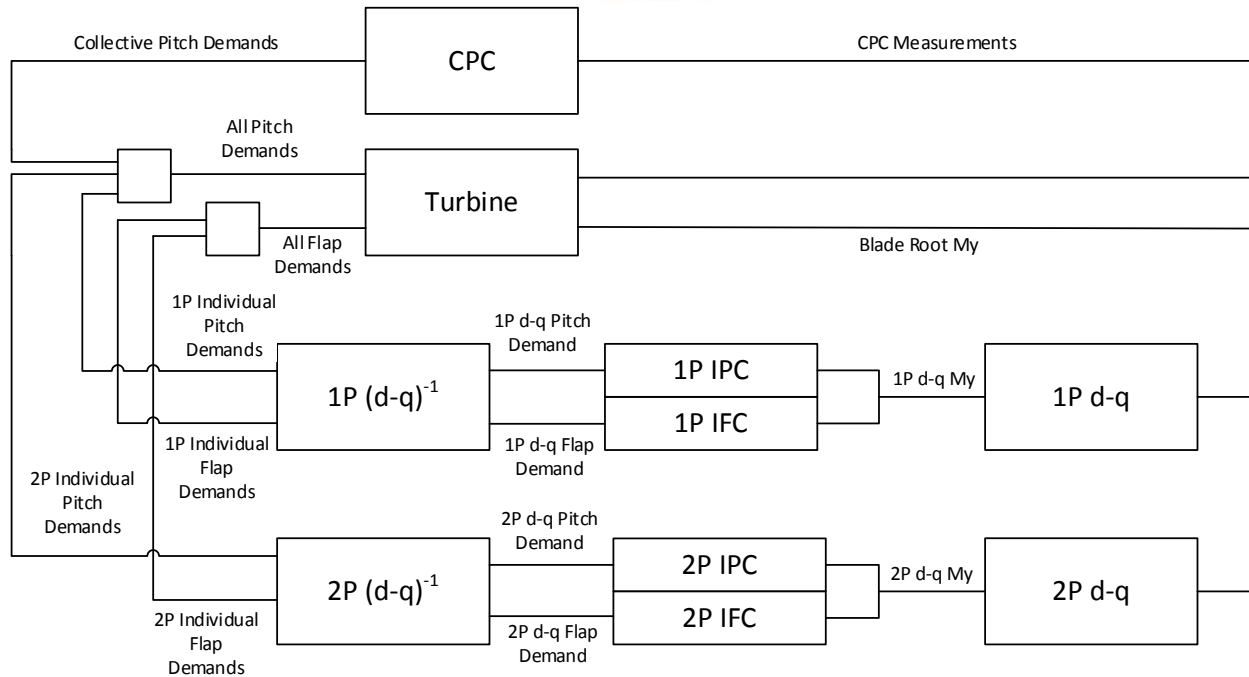


Figure 19: Schematic of IPC and IFC control loops

Ideally d and q-axis blade root loading is only affected by d and q-axis pitch demands respectively; however, due to actuator dynamics and turbine flexibilities there is a coupling of both d and q-axis pitch demands with d and q-axis blade root loading. By including a phase shift in the d and q-axis demands, the coupling can be almost entirely removed making controller tuning straight forward, i.e. the d and q-axis control loops can be tuned independently. Furthermore, when using both IPC and IFC (IFPC), algorithm design is simplified if the blade root loading from pitch and flap demands are in phase.

The IPC and IFC control loops are implemented as parallel, filtered proportional-integral (PI) controllers, one for the d-axis and one for the q-axis. The PI gains are identical for the d and q-axis. The filtering is applied after the d-q axis transforms to isolate the target frequencies of each loop; 1P and 3P for the 1P transform, 1P, 2P and 3P for the 2P transform. The 1P loops are described by the following equation:

$$\frac{\theta_{x1P}}{M_{x1P}} = \left( K_p + \frac{K_i}{s} \right) \left( \frac{4\pi^2}{s^2 + 8.92 + 4\pi^2} \right) \left( \frac{s^2 + 0.02s + 1}{s^2 + 0.6s + 1} \right) \left( \frac{s^2 + 0.06s + 9}{s^2 + 1.8s + 9} \right)$$

and the 2P loops are described by the following equation:

$$\frac{\theta_{x2P}}{M_{x2P}} = \left( K_p + \frac{K_i}{s} \right) \left( \frac{4\pi^2}{s^2 + 8.92 + 4\pi^2} \right) \left( \frac{s^2 + 0.02s + 1}{s^2 + 0.6s + 1} \right) \left( \frac{s^2 + 0.04s + 9}{s^2 + 1.2s + 9} \right) \left( \frac{s^2 + 0.06s + 9}{s^2 + 1.8s + 9} \right)$$



where  $x$  indicates either the d or q-axis and  $\theta$  indicates the demanded blade pitch or TEF deployment angle.  $K_p$  and  $K_i$  values are given in Table 11.

Table 12 Controller gains for IPC and IFC controllers

	Pitch Gain	Flap Gain
$K_p$ ( $^{\circ}/\text{Nm}$ )	8.74E-10	4.37E-9
$K_i$ ( $^{\circ}\text{s}/\text{Nm}$ )	1.01E-9	5.05E-9

The loops are designed to remove 1P and 2P blade loading with a time constant of  $\sim 15$  s. This is typically sufficient to remove deterministic loading created by slowly varying events such as wind shear, wind direction and turbine geometry. Adjusting the 1P and 2P pitch actions more quickly can amplify 1P loading on the non-rotating structure, for example loads to due rotor imbalances.

We denote the combined IPC and IFC controller IFPC. In the IFPC controller, the pitch activity is limited until the flap activity has reached sufficient amplitude that it is at risk of saturating. This way the flap actuation is prioritised above pitch actuation, resulting in our target of reducing overall pitch activity. An example time series of this behaviour is shown in Figure 20 in which we can see as the flap amplitude falls, the IPC action is gradually phased out.

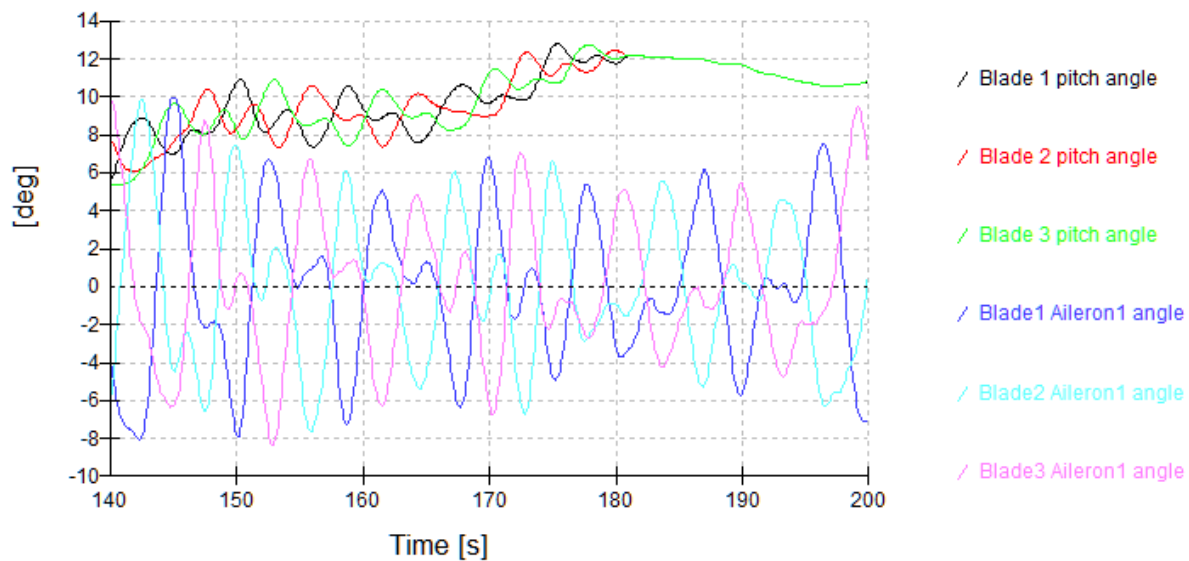


Figure 20 Time series response of pitch and flap angles demonstrating maximum IPC contribution logic.



The IPC and IFC algorithms are designed to operate in parallel with a collective pitch control system. The structure of the collective pitch control system is presented in [10], though the controller has been retuned for this study. The Annual Energy Yield comparison when using IPC and IFPC in turbulent wind shows no difference in electrical power production.

Example time series of the pitch and flap response when using IPC and IFPC in turbulent wind with mean wind speed of 14 m/s and direction error of  $8^\circ$  is shown in Figure 21, with accompanying spectral analysis shown in Figure 22. We can see that the pitch activity at 1P and 2P for the IFPC controller is significantly lower than for the IP case. The extent to which pitching can be reduced will be dictated by the size, aerodynamic characteristics and actuation range. For this study's configuration, pitch spectral peaks at 1P and 2P were reduced by a factor of 10 and 2 respectively when operating near rated wind speeds.

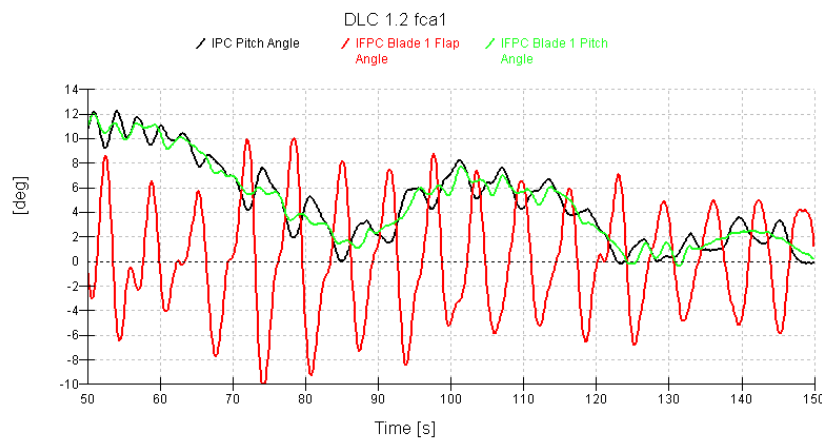


Figure 21 Example time series response if pitch angle and flap angle when using IPC and IFPC.

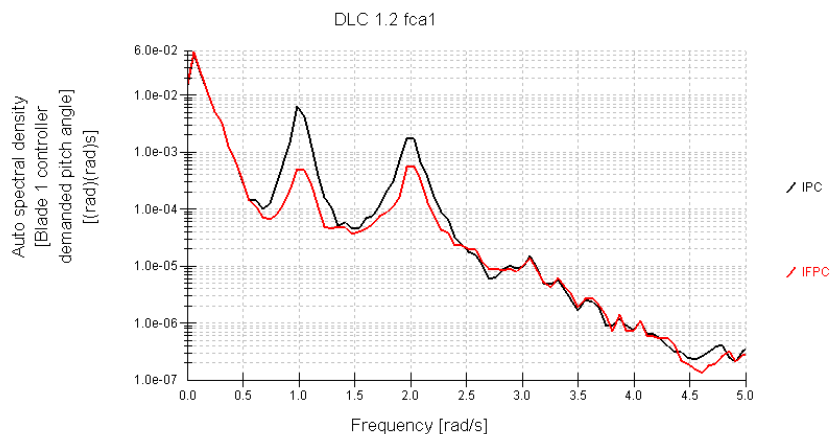


Figure 22 Example spectral response of pitch angle when using IPC and IFPC.



## Supervisory Control

Pitch failures on a wind turbine can introduce significant asymmetric loading across the rotor. Trailing edge flaps can be used to reduce the levels of asymmetric loading if the failures are correctly detected. We have implemented controller logic that moves the flaps towards the mean pitch measured pitch angle between all three blades on detection of a pitch fault. Then the total thrust difference across the three blades is reduced. During a blade pitching fault, the faulted blade can still have a slight feathering effect applied by fully deploying the trailing edge flap on that blade and the opposite applied by the other blades. Figure 23 shows an example of this approach during a pitch seizure at rated wind speed; note the reduction in Stationary Hub Myz loading when the flaps are deployed to oppose the blade pitch asymmetry rather than being pitched to 0.

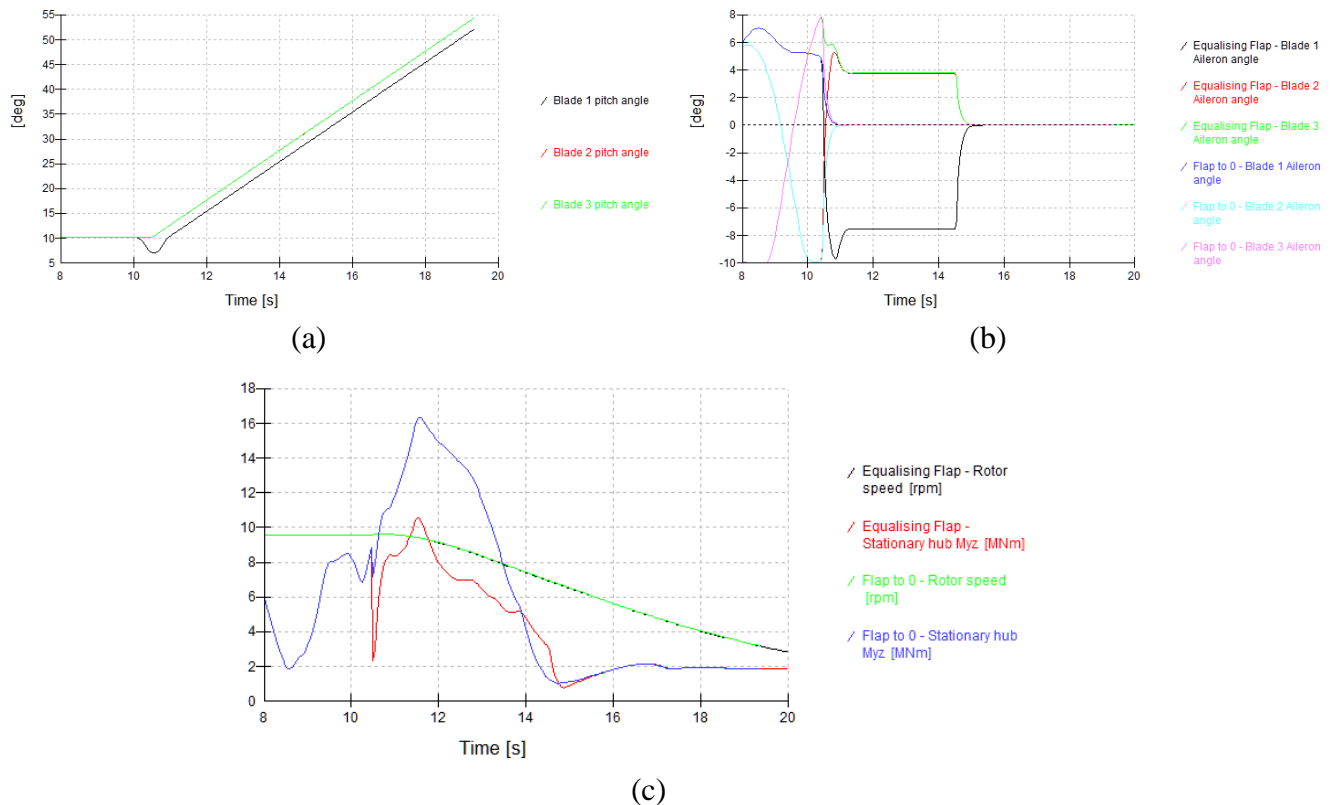


Figure 23 Time series response during pitch failure (individual runaway to fine) of flaps to 0 on fault detection and faults to equalise asymmetric loading.

Including flap actuators introduces a new set of failure mechanisms that need to be addressed. In this work, we have included alarms to ensure safe operation of the turbine in the case of flap system failures and flap controller failures:



1. Flap algorithm failures are detected if the mean demanded flap angle exceeds  $0^\circ$  by a preset threshold. This would indicate the D-Q axis commands are not being correctly applied.
2. Flap system failures are detected by sensing a mismatch in the measured flap angle and the demanded flap angle and accounting for the dynamics of the flap actuator.

If either failure is detected, the flap angle demand is set to the mean of the measured flap angles to equalise the load on each of the blades; IPC is enabled and the turbine undergoes a closed loop shutdown.

A full list of shutdown programs is given in Table 12 and a list of alarms with example failures and consequences is given in Table 13.

Table 13 Shutdown Programs for 10 MW Reference Turbine

Shutdown Name	Pitch Action	Flap Action	Generator Action
Safety System Circuit 1	Pitch is set to a rate of $5^\circ/\text{s}$	Move to negative limit	Disconnect immediately
Grid Loss	Pitch is set to a rate of $5^\circ/\text{s}$	Move to negative limit	Ramp to 0 Nm in 4 s
Autonomous Feather	Pitch is set to a rate of $5^\circ/\text{s}$	Move to mean measured pitch angle	As defined in Table 0-3
Fast	Pitch is set to a rate of $5^\circ/\text{s}$	Move to negative limit	As defined in Table 0-3
Normal	Power setpoint is ramped down at $350\text{kW}/\text{s}$ . When the generator is disconnected, the blades are pitched to feather at $4^\circ/\text{s}$ .	Move to mean measured flap angle	Follow operating torque curve

Table 14 Alarms for 10 MW Reference Turbine (Blue shading indicates flap related alarms)

Alarm	Shutdown Program	Possible Failures	Threshold
NA Overspeed	Safety system circuit 1	Any	$60.32 \text{ rads}^{-1}$
N4 Overspeed	Fast	Extreme conditions/ Algorithm fault/Actuator fault	$56.79 \text{ rads}^{-1}$
Low pitch angle demand overspeed	Fast	Algorithm failure	$1^\circ$ if speed is $> 52.27 \text{ rads}^{-1}$
Pitch demand sanity	Fast	Algorithm failure	$< -1.5^\circ/\text{s}^{-1}$ if speed is $> 50.26 \text{ rads}^{-1}$



Pitch rate to fine	Fast	Algorithm failure	$< -3^{\circ}\text{s}^{-1}$
Demanded collective pitch angle below fine	Fast	Algorithm failure	$< -1^{\circ}$
Measured collective pitch angle below fine	Fast	Algorithm failure	$< -1^{\circ}$
Pitch following error	Autonomous Feather	Pitch system fault	$> 4.5^{\circ}$ for $> 1$ s.
Modelled pitch following error	Autonomous Feather	Pitch system fault	$> 1.5^{\circ}$
Modelled flap following error	Normal	Flap system fault	$> 2.5^{\circ}$
Maximum pitch demand difference	Fast	IPC algorithm failure	$10^{\circ}$
IPC demand error	Fast	IPC algorithm failure	$0.5^{\circ}$
IFC demand error	Fast	IFC algorithm failure	$1^{\circ}$
High yaw error	Normal	Yaw system failure	5 s average yaw error $>$ threshold while 5 s average wind speed $> 2\text{ms}^{-1}$ (see Table 0-4)

Table 15 Torque vs. Generator speed Lookup Table During Open Loop Shutdowns

Generator Speed (rad/s)	36.65	50.26
Torque (kNm)	0	212

Table 16 Wind Speed vs Yaw Error Threshold Before Shutdown

Wind Speed (m/s)	0	5	10.0	35
Yaw Error (rad)	1.047	1.047	0.785	0.523

## Results

A set of IEC design load calculations have also been undertaken to validate test whether extreme load reductions can be obtained whilst keeping the IFPC tuning to give the same or better extreme loading in addition to reduced pitch actuator usage. Details of the load cases simulated are given in [Appendix A]. Relative comparisons of lifetime fatigue loads of major components are given in Table 16 and relative extreme load results are given in Table 17. Note that the lifetime damage-equivalent-load (DEL) is given assuming  $10^7$  cycles over 25 years.

In the extreme load results, for DLC1.3, the characteristic loads for each load case group were calculated as the mean of the maxima from each of the six seeds. For DLC1.4, DLC2.3 and DLC4.2,



the maximum value is reported. Finally, for DLC2.1 and DLC2.2, the characteristic loads for each load case group are calculated as the mean of the upper half of the maxima from each of the twelve seeds.

Fatigue loads of IFPC typically higher than IPC, but are within 2.5%. It is usually possible with fine-tuning to reduce this difference, or even make IFPC perform better due to the extra actuation, however, the aim in the case of this study is to get fatigue load reduction similar and see the benefits in reduced actuator usage and impacts on extreme loading.

Extreme loading is also very similar, typically within 4%, however the hub yaw and tower base torsional loading is reduced significantly, 9.8% and 10.3% respectively. The extra potential for equalising loads over the rotor is then providing a clear load reduction benefit. Collective-thrust loading is likely to be driving the tower base overturning moment, so further tuning of the collective pitch loops and extreme event response may be able to get the tower base loads back to IPC levels.

The TTC has reduced from 2.02 m to 1.76 m when using IFPC as shown in Table 18.

Table 17 Relative fatigue loads of IFPC versus IPC

Component	Direction	Change from IPC (%)	
		m = 4	m = 10
Stationary Hub	In-plane	0.2	NA
	Tilt	0.9	NA
	Yaw	2.1	NA
Blade root	Edgewise	0.0	-0.1
	Flapwise	-0.7	-0.4
	Torsion	1.9	2.5
Tower base	Overturning	1.0	NA
	Torsion	2.3	NA

Table 18 Relative extreme loads of IFPC versus IPC

Component	Moment Direction	Change from IPC (%)	Load case (names as given in the Appendix)
Stationary Hub	In-plane	-0.1	DLC1.3ea-6
	Tilt	0.0	DLC1.4bcb_2_b
	Yaw	-9.8	DLC2.2bc5
	Out-of-plane resolved	0.0	DLC1.4bcb_2_b
Blade Root	Edgewise	2.8	DLC2.2ec8
	Flapwise	0.8	DLC1.4bcb_2_c
	Bending resolved	0.8	DLC1.4bcb_2_c
Tower Base	Torsional	-4.2	DLC1.4cba_2_b
	Side-side	-1.9	DLC1.4cca_1_d
	Fore-aft	3.3	DLC2.2eb7



Table 19 TTC for IPC and IFPC

	IPC	IFPC
TTC (m)	2.02	1.76



### 3.0 Application of Distributed Blade Control to Two Bladed Wind Turbines (DTU)

#### Comparison of the DTU 10MW two bladed wind turbine in onshore and floating configurations

Innovative concepts of two bladed rotors mounted on a semi-floater are shown to possibly have significant benefits in fatigue load reduction of the sub-structure and can result in a significant reduction of LCOE [11]. The semi-floater concept has been evaluated in [11], where a two-bladed scaled version of the DTU10MW RWT three-bladed rotor is taken. An illustration of the two-bladed rotor mounter on the semi-floater is shown in Figure 24. In this study, before evaluating the impact of distributed controls on the semi-floater offshore configuration, a load comparison between the onshore version and the semi-floater version of the two-bladed DTU10MW wind turbine is performed. In both cases, the rotor design corresponds to the downwind version of the two-bladed scaled rotor with no coning or tilt [12].



Figure 24 - Illustration of the two bladed rotor mounted on the semi-floater.

All wind turbine models in this study are evaluated using DTU's aeroelastic tool HAWC2 in a realistic industry-based Design Load Basis (DLB). The utilized DLB follows the current design standard (third edition of the IEC 61400-1 [13]) and is representative of a general DLB used by the industry in a certification process. The overview of the parameters defining the Design Load Cases (DLC) is



presented in [14]. Following the standard load cases for the evaluation of innovative designs in the INN WIND project, a reduced DLB is utilized, as shown in Table 20. The standard DTU Wind Energy Design Load Case post-processing method for the DLB has been utilized. This includes the process of extraction of the defined load sensors statistics, the ultimate load analysis including the prescribed safety factor, and the fatigue analysis. Representative load sensors on the main components of the wind turbine aeroelastic model are chosen, with the corresponding parameters for fatigue analysis (Table 21).

Table 20 - Description of load cases.

Load cases														
Name	Load	PSF	Description	WSP	Wdir	Wavedir	Turb	Seeds	Shear	WSP_dist	Wdir_dist	Wavedir_dist	T	Files
DLCxxx	U: ultimate, F: fatigue	Partial safety factor for U		Wind speed [m/s]	Wind direction [deg]	Wave direction [deg]	Turbulence	Number of seeds	Shear factor	Fatigue WSP distribution	Fatige Wdir distribution [%]	Fatige Wdir distribution [%]	Simulation time [s]	Number of files
DLC12	U/F	1.25	Normal production	4:2:26	-10/0/10	-10/0/10	NTM	6	0.2	Weibull	25/50/25	25/50/25	600	648
DLC13	U	1.35	Normal production	4:2:26	-10/0/10	0	ETM	2	0.2				600	72
DLC62	U	1.1	Parked grid loss	43	0:15:345	0:15:345	0.11	1	0.11				600	72

Table 21 - Description of load channels.

Load channels	
MxTB	Tower bottom fore-aft
MyTB	Tower bottom side-side
MxTT	Tower top tilt
MyTT	Tower top roll
MzTT	Tower top yaw
MxMB	Main bearing tilt
MyMB	Main bearing yaw
MzMB	Main bearing torsion
MxBR	Blade root flap
MyBR	Blade root edge
MzBR	Blade root torsion
MxFB	Foundation moment fore-aft
MyFB	Foundation moment side-side
MzFB	Foundation moment torsion
MxFT	Floater base moment fore-aft
MyFT	Floater base moment side-side
MzFT	Floater base moment torsion
FxML	Axial force in mooring line



For the comparison of the onshore and semi-floater loads, the onshore model has been evaluated with the equivalent onshore load cases, and the geometry of the tower and foundation is changed in the offshore version to incorporate the floater. The results are shown in terms of lifetime fatigue load (Figure 25) and ultimate load (Figure 26) comparisons. It is seen that, as also reported in previous studies, most of the load channels lifetime fatigue and ultimate levels are largely reduced up to 95% and 78% respectively.

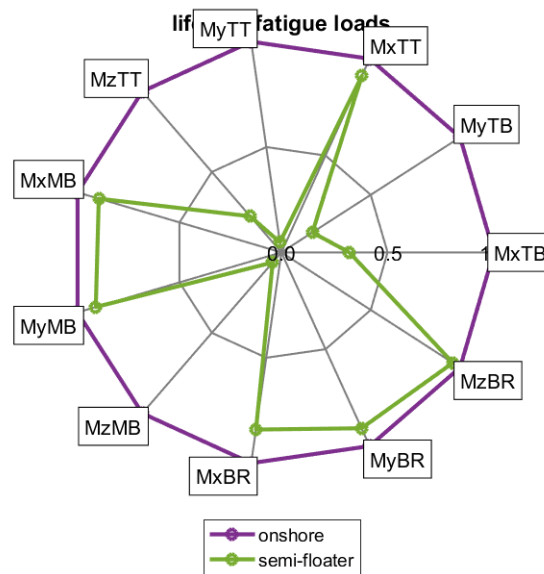


Figure 25 - Comparison of lifetime fatigue loads - onshore vs semi-floater.

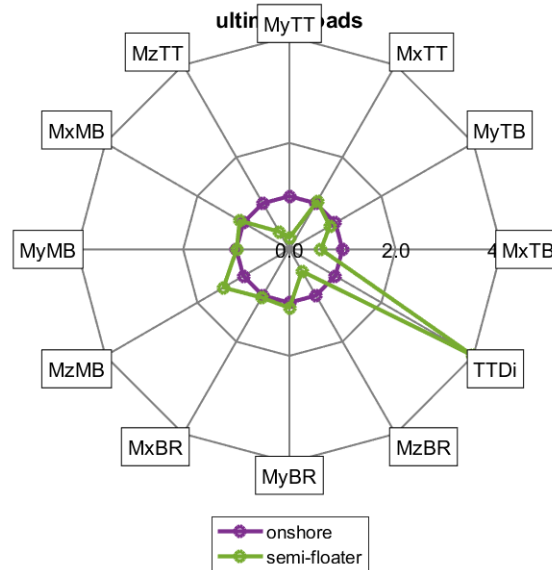


Figure 26 - Comparison of ultimate loads - onshore vs semi-floater.

## Evaluation of individual flap control on the DTU 10MW two-bladed wind turbine in onshore configuration

The flap configuration described in the first section of the report is applied on the onshore realization of the two-bladed DTU 10MW wind turbine model. The results are shown in terms of lifetime fatigue load (Figure 27) and ultimate load (Figure 28) comparisons. It is seen that, most of the load channels lifetime fatigue and ultimate levels are largely reduced up to 59% and 47% respectively.

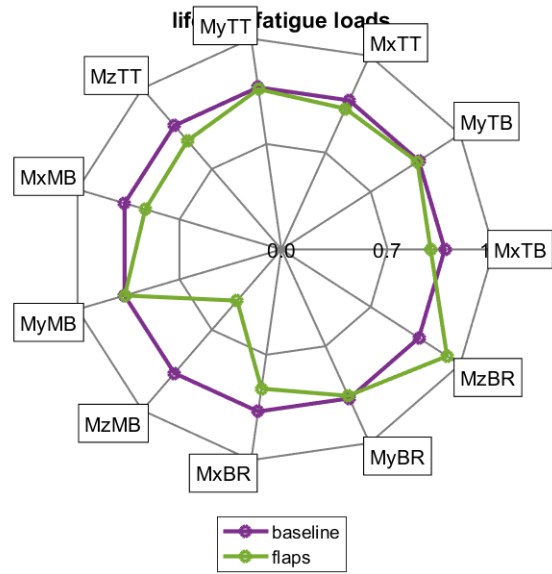


Figure 27 - Comparison of lifetime fatigue loads – baseline vs flaps (onshore).

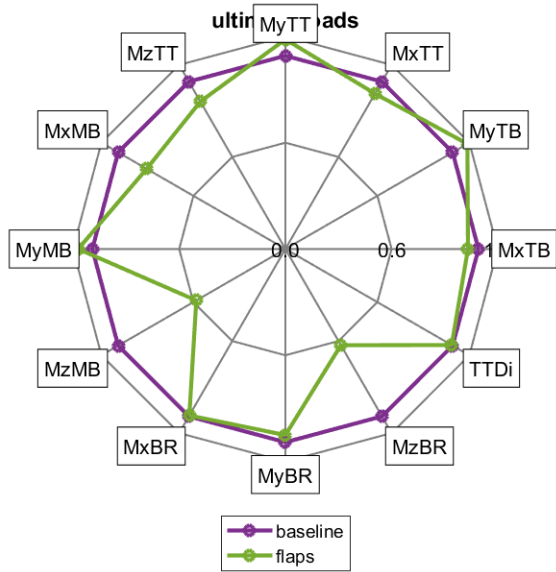


Figure 28 - Comparison of ultimate loads – baseline vs flaps (onshore).



## Evaluation of individual flap control on the DTU 10MW two-bladed wind turbine on the semi-floater

The flap configuration described in the first section of the report is applied on the onshore realization of the two-bladed DTU 10MW wind turbine model. The results are shown in terms of lifetime fatigue load (Figure 29) and ultimate load (Figure 30) comparisons. It is seen that, most of the load channels lifetime fatigue and ultimate levels are largely reduced up to 16% and 21% respectively.

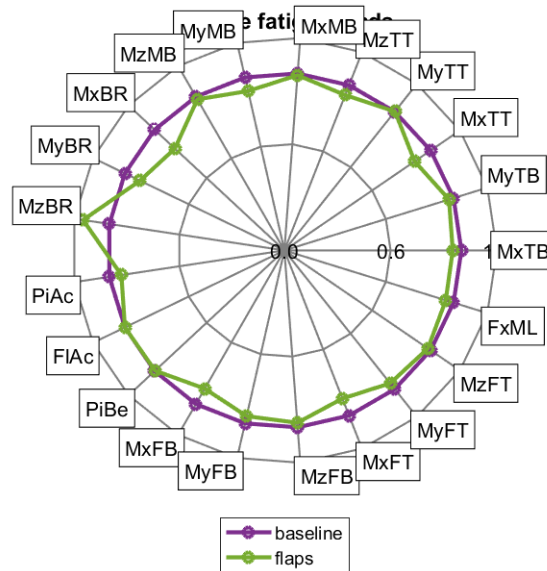


Figure 29 - Comparison of lifetime fatigue loads – baseline vs flaps (semi-floater).

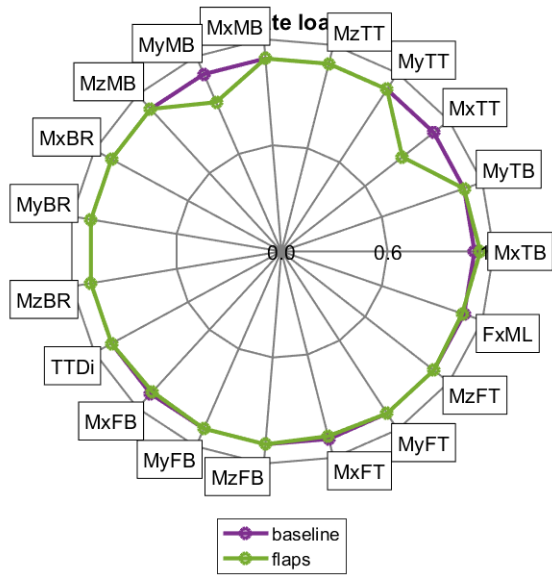


Figure 30 - Comparison of ultimate loads – baseline vs flaps (semi-floater).

## 4.0 Spinner Anemometer and Spinner Lidar Demonstrations (DTU)

A spinner anemometer was mounted on the experimental DTU wind turbine Vestas V52 at the DTU test site at Risø campus in November 2015, see Figures 32 and 33 for the purposes of demonstrating its measurement capabilities as an input for future feed-forward control mechanisms. Measurements are available from 22 November 2015.

The spinner anemometer measurement principles are documented in articles and reports [15,16]. The calibration methods of the spinner anemometer are summarized in [17]. An overall table of the calibration steps is shown below in Figure 31.

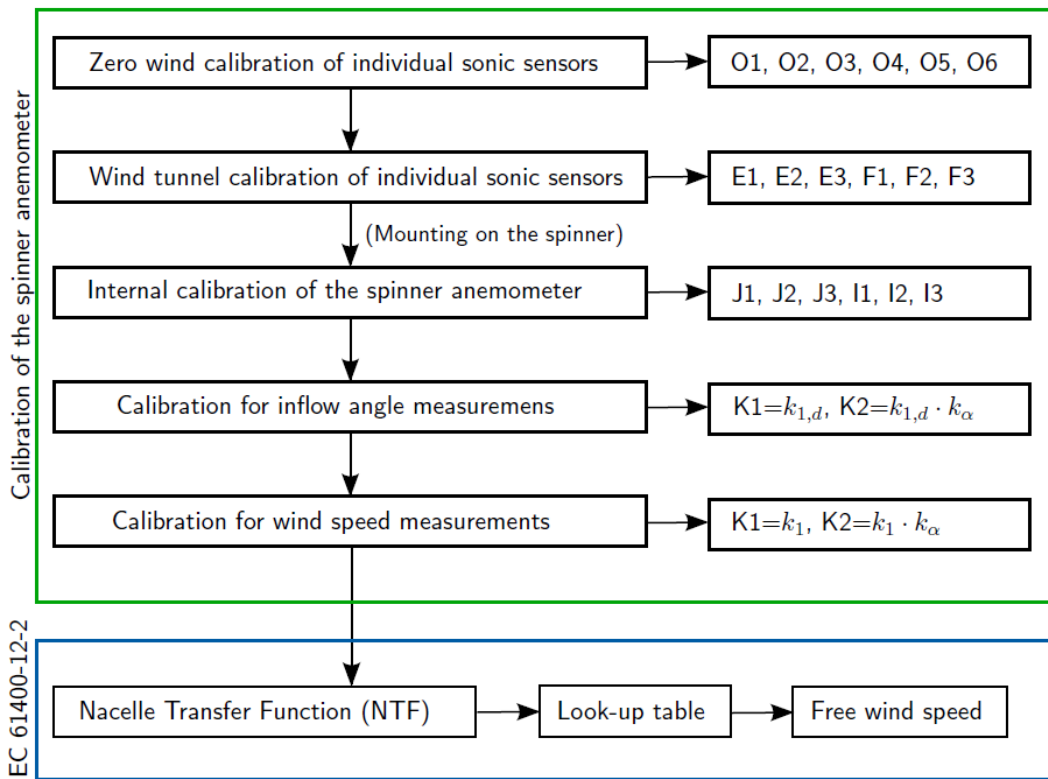


Figure 31 Overview of steps involved in the calibration of a spinner anemometer, from (7). To the right are shown the calibration parameters that may be inserted into the spinner anemometer box



Figure 32 Installed spinner anemometer on experimental DTU wind turbine Vestas V52 showing one sonic sensor mounted in line with the shaft axis



Figure 33 Installed spinner anemometer on experimental DTU wind turbine Vestas V52 showing two sonic sensors. One sensor shows the tilted sonic path in order to avoid sensor head flow distortions

### Zero wind speed calibration

Zero wind speed calibration was made in order to measure zero wind speed correctly with no offset. This zero wind speed calibration is not important for traceability of the spinner anemometer since traceability is attained with the mast cup anemometer through the NTF calibration.

## Wind tunnel calibration of sonic sensors

Wind tunnel calibration of sonic sensors are made according to the IEC standard [18] with the elaboration on mounting of the sensors in the wind tunnel, see Figure 34. Wind tunnel calibrations of the spinner anemometer sonic sensors on the V52 turbine have not been made, and they are not necessary for the traceability of the spinner anemometer since traceability is attained with the mast cup anemometer through the NTF calibration.

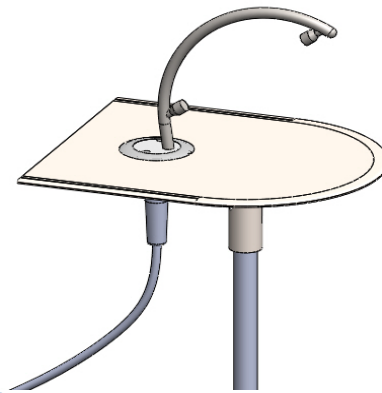


Figure 34 Mounting of spinner anemometer sonic sensor in wind tunnel, from (12)

## Internal calibration of the spinner anemometer

An internal calibration of the spinner anemometer was made with half an hour of wind measurements just after installation of the spinner anemometer sonic sensors on the spinner. The internal calibration makes a correction of the local sonic sensor measurements so that they all match each other, i.e. they all give the same measurements over time. The internal calibration out-compensates non-rotation symmetry of the spinner and the effects of installation uncertainties. The internal calibration is meant to eliminate systematic 1P variations without changing average wind speed measurements or adding uncertainty to the measurements. The internal calibration procedure is described in [17].

## Calibration for inflow angle measurements

Calibration for inflow angle measurements was made according to the procedure in [19]. The calibration was made on a day with about 6m/s average wind speed. Unfortunately, the wind direction was on average 50°, north-east, see Figure 37, which is a direction with relatively high flow distortion. A better calibration direction would have been the free sector 259° to 314°, see Figure 37. However, the calibration was made successfully. The wind turbine was stopped and yawed several times in and out of the wind while measurements were made with high sampling frequency (10Hz), sampling the spinner anemometer yaw misalignment and the yaw direction of the wind turbine. The measurements



are shown in Figure 35, showing that the default k constants give close to the correct yaw misalignment measurements. A full analysis to detect the uncertainty was not made.

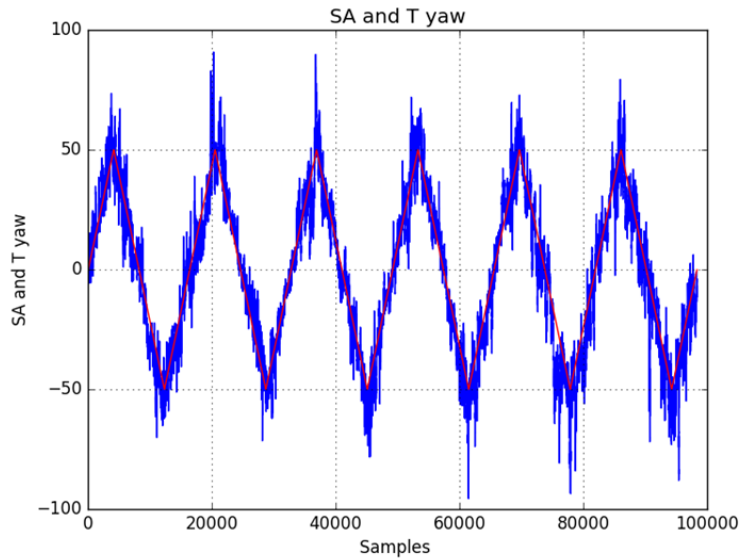


Figure 35 Yaw calibration measurements of the spinner anemometer on the V52. Red is wind turbine yaw and blue is spinner anemometer yaw misalignment

Yaw misalignment measurements on V52 from all wind directions in the period November 2015 to October 2016 are shown in Figure 36.

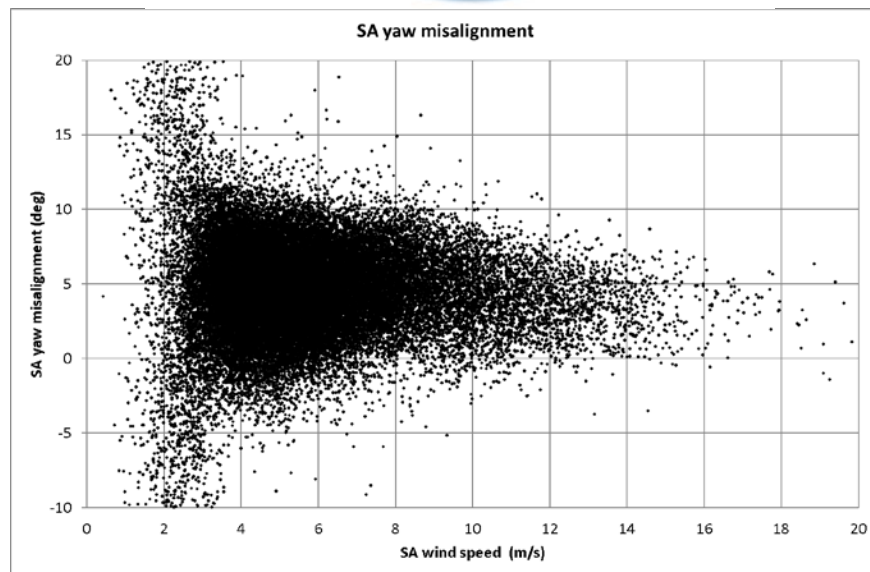
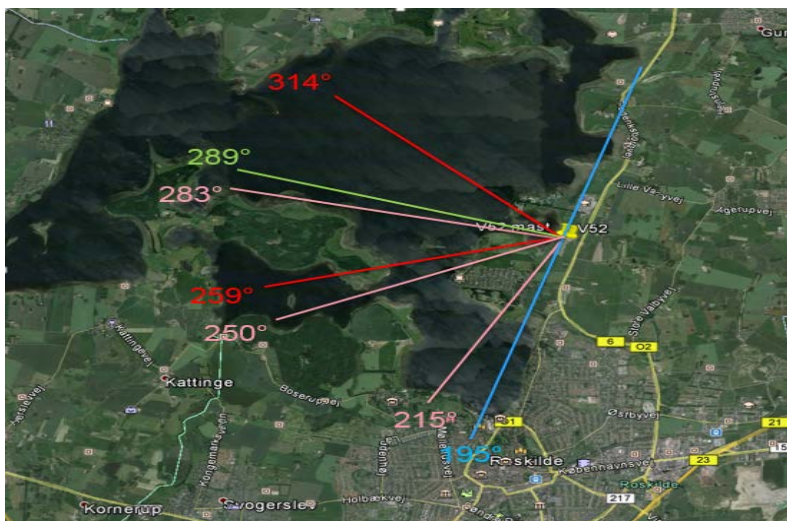


Figure 36 Yaw misalignment measurements on V52



Directions:	
Free sector:	259°-314°
Mast:	289°
Turbine row:	195°
Veddelev village:	215°-250°
Bognæs forest:	250°-283°
Open water:	283°-314°

Figure 37 Free wind sector for wind speed measurement calibration

## Calibration of local and free wind speed measurements with use of NTF

The calibration for wind speed measurements was made as described in [20] during operation of the wind turbine in the period November 2015 to October 2016. The data were sorted for wind directions in the free sector between 259° and 314°, see Figure 37. Additional sorting of data included the spinner anemometer quality signals `Speed_Quality_avg`, `Speed_Quality_stdev`, `sa_Acc_Quality_avg`,



sa\_Acc\_Quality\_stdev. Setting these parameters equal to zero ensures that all spinner anemometer sonic and accelerometer sensors are functioning without any faults during the 10min datasets. Filtering was also made for cup and sonic wind speeds equal to zero. A few outliers were also eliminated.

The cup versus spinner anemometer wind speeds are shown in Figure 38, where also the correction factor  $F1=1.445$  is shown.  $F1$  may be used as a proportionality factor to correct the spinner anemometer wind speed measurements. Corrected data are shown in Figure 39. The deviations from the straight line in Figure 9 determines the NTF or induction. The induction is shown in Figure 40 as function of the spinner anemometer wind speed. Induction is determined by:

$$a = \frac{U_{cup} - U_{sa}}{U_{cup}}$$

The induction can be fitted to the following formula, ensuring that the regression line is 1.000:

$$a = B \left( \frac{U_{sa} - C}{A} \right)^{D-1} \cdot \exp\left(-\left(\frac{U_{sa} - C}{A}\right)^D\right)$$

For V52 the A to D parameters were found to:  $A=5,71$ ,  $B=0,449$ ,  $C=3$  and  $D=2$ .

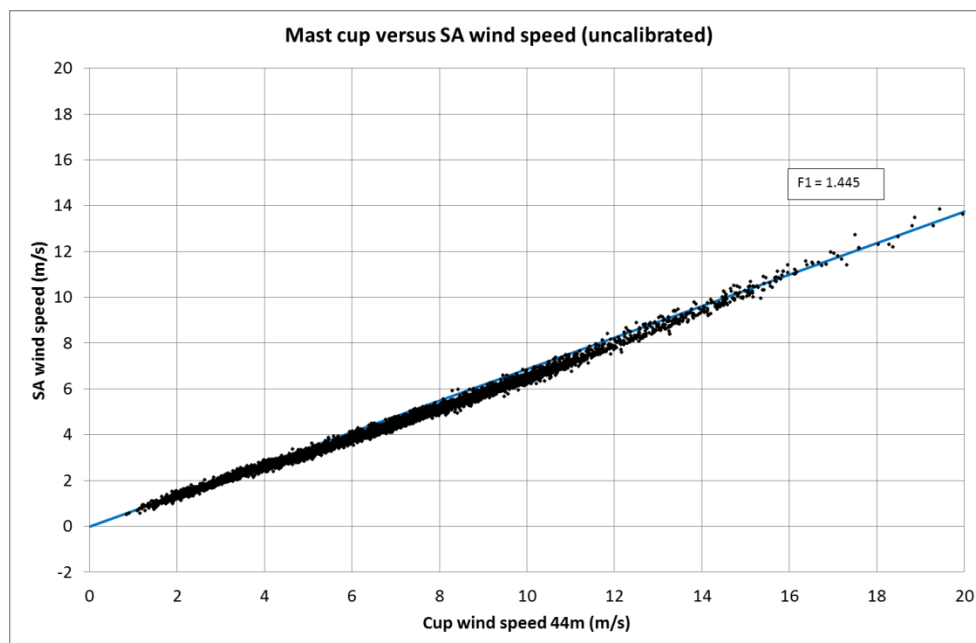


Figure 38 Spinner anemometer wind speed versus cup wind speed at 44m height

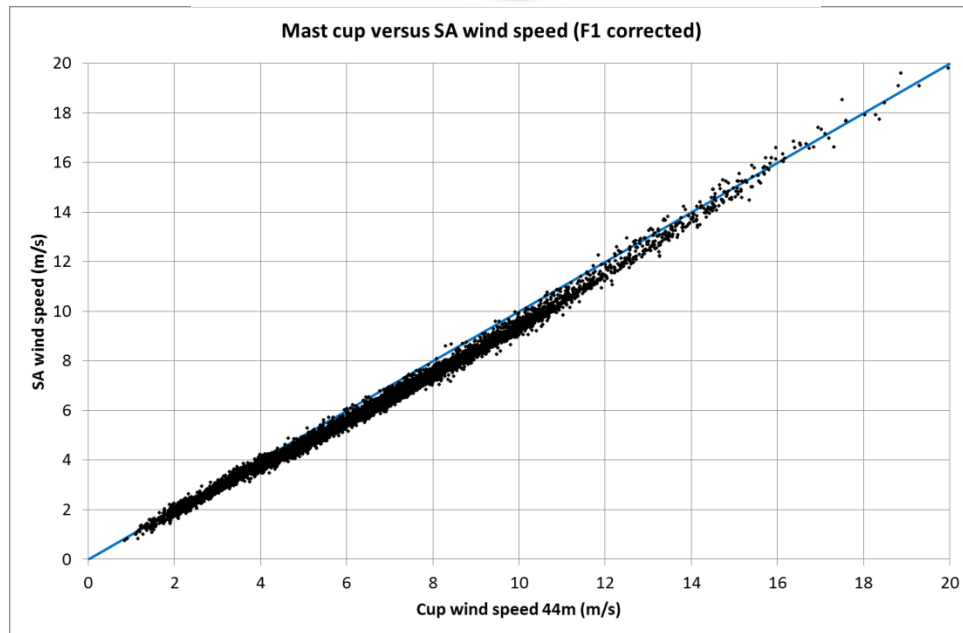


Figure 39 Spinner anemometer wind speed corrected with  $F1=1.455$  versus cup wind speed at 44m height

Applying the induction or NTF to find the free wind speed the following formula is used:

$$U_{free} = U_{sa}/(1 - a)$$

The measured free wind speed with the spinner anemometer is shown in Figure 41.

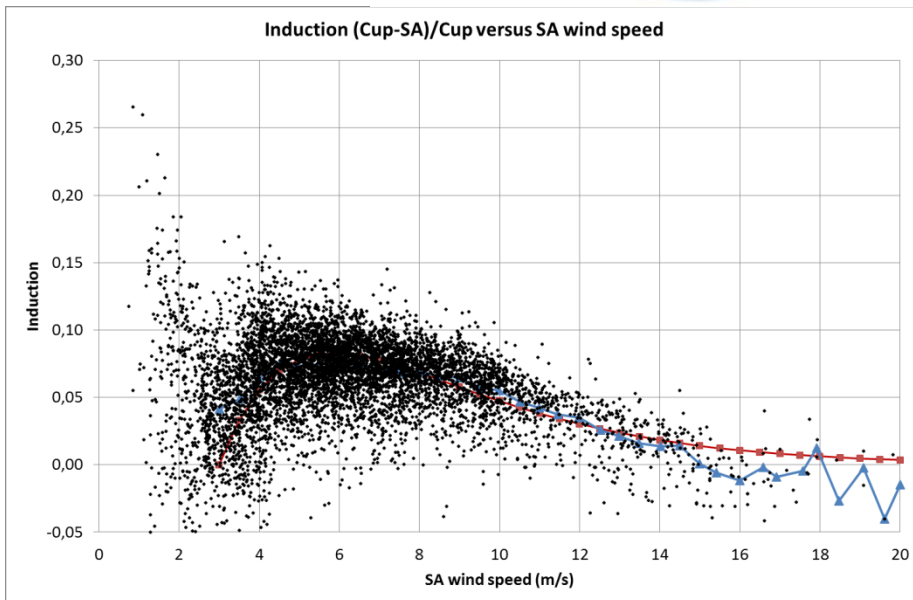


Figure 40 Induction at the spinner anemometer corresponding to the correction in the NTF. Red curve is fitted formula. Blue curve is fitted with method of bins.

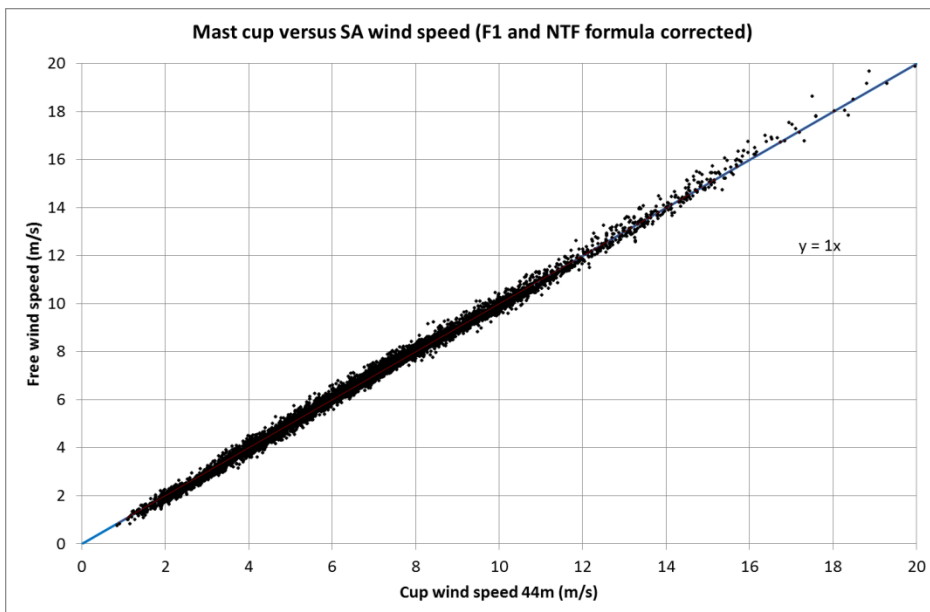


Figure 41 Spinner anemometer wind speed corrected with F1 and NTF formula to get the free wind speed

The spinner anemometer turbulence (standard deviation of the wind speed) measured in the same period is plotted against the cup anemometer turbulence, shown in Figure 42.

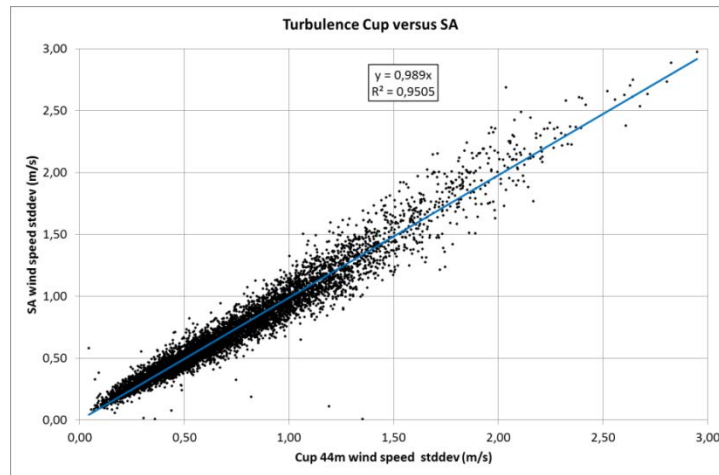


Figure 42 Turbulence (standard deviation) of spinner anemometer versus cup anemometer at 44m height

The Figures 38-42 demonstrate the spinner anemometer mounted on the V-52 test turbine is able to measure the mean wind speed, direction and turbulence adequately and the same measurements can be utilized in feed-forward control of the turbine or in supervisory control to mitigate fatigue damage.

On a two-bladed wind turbine, four sonic sensors may be mounted on the spinner at the centre of the rotor. The sonic sensors on the spinner should be mounted in pairs in front of the blade roots and in the gaps between the blade roots. The flow over the spinner is assumed to follow the same flow equations as for the spinner anemometer for three-bladed wind turbines. This assumption is made for each of the two pairs of sonic sensors. The conversion algorithm converts the sonic sensor path flow velocities and the rotor azimuth position to the free horizontal wind speed and the flow direction. The free wind speed is here defined as the free wind speed determined at stand still of the rotor. This means that the influence of the rotor induction during operation is not taken into account, and the drag of the spinner, blade roots and nacelle arrangement is cancelled out in the measurement. This also means that the spinner anemometer wind measurements cannot be considered to be the local wind speed at the spinner, and can thus not be compared directly to for example lidar measurements in front of the spinner.

The generic relation between the sonic sensor path flow velocities  $V_1, V_2, V_3, V_4$ , the free wind speed  $U$  and the inflow angle to the rotor axis  $\alpha$  at the azimuth position of the flow stagnation point on the spinner  $\theta$  is then:



$$V_1 = U(k_1 \cos \alpha - k_2 \sin \alpha \cos \theta) \quad (3)$$

$$V_2 = U(k_1 \cos \alpha - k_2 \sin \alpha \cos(\theta - \pi)) \quad (4)$$

$$V_3 = U(k_3 \cos \alpha - k_4 \sin \alpha \cos(\theta - \frac{\pi}{2})) \quad (5)$$

$$V_3 = U(k_3 \cos \alpha - k_4 \sin \alpha \cos(\theta - \frac{3\pi}{2})) \quad (6)$$

These generic equations include the four spinner anemometer algorithm constants  $k_1$ ,  $k_2$ ,  $k_3$  and  $k_4$ . The formulas are paired so that equation 1 and 2 relates to the wind orthogonal to the blade roots while equation 5 and 6 relates to the wind along the blade roots.

The ratio  $k_{\alpha 1} = k_2/k_1$  between the two constants of the first pair is a generic constant that relates to the inflow angle  $\alpha$  alone and it must be calibrated to measure the flow angle correctly. The constant  $k_1$  is afterwards calibrated for measurement of free wind speed  $U$ , see calibration procedures for three-bladed wind turbines [17]. A similar relation is valid for the other sonic sensor pair along the blade roots.

### Demonstration of Fatigue Load Reduction with De-Rating

The Vestas V-52 turbine was de-rated from its rated power of 850 kW to 600 kW for a measurement period spanning 1.5 months from Nov. 1 2016 to Dec. 15 2016. The remaining period beyond Dec 15, 2016 pertains to normal operation of the wind turbine. During both periods of operation, the spinner anemometer continually measures the mean wind velocities, direction and longitudinal turbulence. Further, several high frequency measurements are continuous logged from the turbine. These comprise of the blade root flap and edge moments, the tower top bending moments, yaw moment, the tower base fore-aft and side-side moment, as well as typical SCADA records such as the rotor speed, power, generator torque, tower top vibrations and blade pitch angle.

Figure 43 depicts the turbulence measured by the spinner anemometer during both periods, while Fig. 44 depicts the de-rated power as compared to the normal power production.

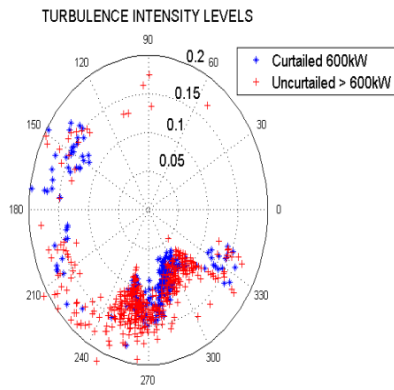


Figure 43: Measured variation of turbulence intensity during the measurement period

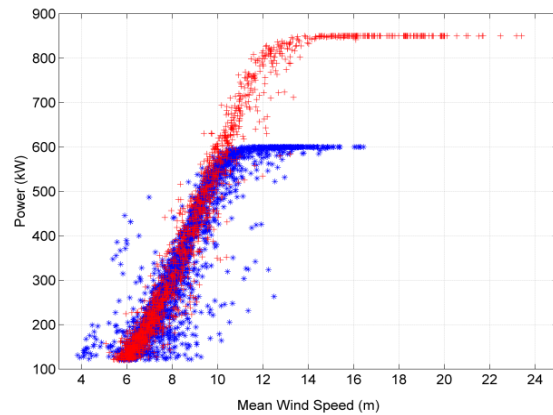
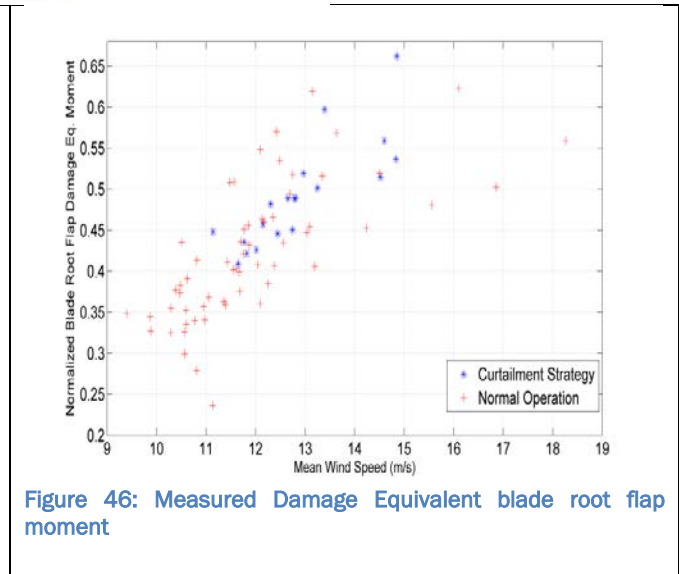
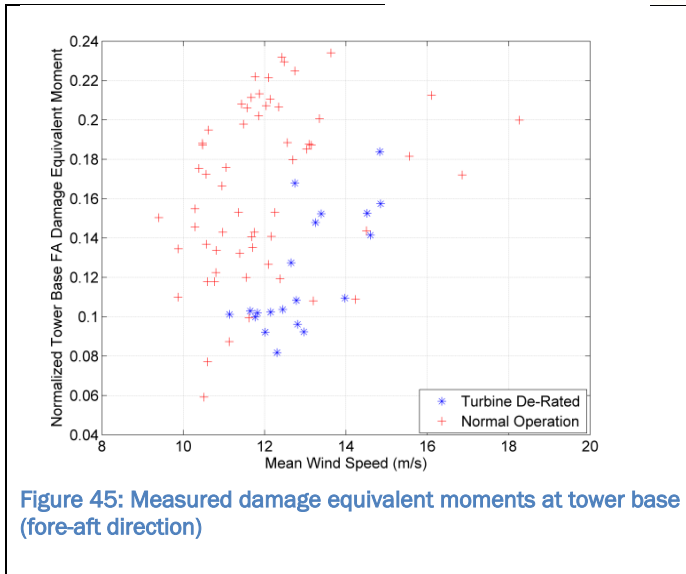


Figure 44: Measured Power curves for curtailed (blue) and normal operation

Based on the measured blade root and tower base loads, the ten minute damage equivalent (Deq) loads were computed as a measure of the blade root fatigue and the tower base fatigue. The Deq were computed both during the curtailed operation and during normal operation to quantify the benefit of curtailment on lowering the fatigue damage.

Since the fatigue damage is a strong function of wind turbulence, a cut-off of turbulence intensity levels above 16% was chosen when the turbine is producing its maximum permitted power level. At 15m/s this corresponds to IEC class A turbulence, which is the highest turbulence class for IEC specific designs. Figure 45 shows the effective reduction in tower base Fore-Aft Deq moment during curtailed operation versus normal operation, while Fig. 46 does the same for blade root Flap Deq moment. It can readily be seen that the tower base fore-aft damage equivalent moments can at certain mean wind speeds be reduced by as much as 40%; while the maximum possible reduction in the blade root damage equivalent moment is of the order of 10%. The reasons for the varying reduction in the damage equivalent moments is based on the fact that the curtailed power of 600 kW is still at the rated rotor speed of the turbine (reached at 9.5m/s) and further reduction in blade root fatigue is possible only if the rotor speed is also reduced. However the significant savings in tower base fatigue with minimal de-rating is a significant benefit to prolong the life of offshore substructures such as jackets.



## Spinner Lidar Demonstration

The DTU Spinner Lidar [21] was shipped to NREL, U.S.A and installed on the CART3 from December 2014 to December 2015 and later to the Scaled Wind Farm Technology (SWiFT) facility by Sandia National Laboratories . The data from the detailed field testing depicted in Figure 47 will help to better understand rotor plane wind evolution.



Figure 47: First field testing of lidar-assisted control at NREL (left), DTU scanning lidar system was installed from February 2014 through October 2015 on the nacelle of the CART3 (right).

With the Spinner Lidar operationally scanning the inflow the following demonstrations were made as envisioned to contribute to the main objectives of the INN WIND.EU project:

1. Detection of wind evolution



A detailed model of the wind evolution with the DTU Spinner Lidar measurements can be derived by analyzing the correlation of the rotor-effective wind speed estimated from turbine data and the rotor-effective wind field measured by the scanning lidar system. Non-frozen wind evolution models can be verified by changing the measurement distance to the scanned measurement points. An improved wind evolution model enhanced with measurements from the full rotor plane measurements will consequently enable more realistic load simulations for large rotor wind turbines.

## 2. Testing of advanced lidar-assisted control

Advanced lidar-assisted controllers [22] achieve a better control performance in simulation studies compared to the baseline feedforward controller already tested on real turbines. These results have already been published in deliverable D1.42. The NREL CART3 Spinner Lidar field test has provided realistic wind measurements that can be used to further develop feed-forward control under realistic full-scale test conditions.

## 3. Measurement in wake situations

The fast scanning Lidar was used to measure the wind fluctuations in the wake of a turbine and to determine the spatial components of the wind velocities. This is a unique characteristic of the Spinner Lidar due to its high sampling of measurement points.

Real-time detailed upwind rotor plane inflow wind measurements with the rotor plane scanning DTU 2D Spinner Lidar is capable of measuring 400 radial wind speeds per second distributed over the entire upwind rotor plane. These 400 measurements per second were streamed in real time from the Spinner Lidar to the computer server at NREL below the CART 3 turbine. Even though, the Spinner Lidar data is not communicating with the control system of the CART3 wind turbine, it was shown that the data could be provided with short enough latency to provide real-time information to the controller for feeding the feed-forward enhanced controllers with concurrent previewed wind information. The Spinner Lidar inflow measurements were synchronized with the CART 3 turbine SCADA data so that detailed information now can be provided about the inflow to aeroelastic load simulations. The line of sight post-processed wind speeds over 16 seconds is shown in Figure 18 as measured by the Spinner Lidar mounted on the Cart wind turbine. The measured contour covers about 60% of the inflow field.

In 2017 high-resolution wake flow measurements obtained from a turbine-mounted scanning lidar have been obtained from 1D to 5D behind another test turbine, a V27. The measured line-of-sight projected wind speeds have in connection with a fast CFD wind field reconstruction model been used to generate 3D wind fields in the scan planes consisting of all three wind components. The combination of a fast-scanning wind lidar and a corresponding fast wind field reconstruction model is shown to be able to provide detailed wind data useful for proactive steering of wakes in real time and also for advanced feed-forward turbine control, [23]. During the contract period several high-resolution lidar wake measurements were obtained from field campaigns in collaboration with NREL and Sandia, lately, in 2017 Spinner Lidar data were recorded at the Scaled Wind Farm Technology (SWiFT) facility<sup>1</sup> by Sandia National Laboratories and the National Renewable Energy Laboratory

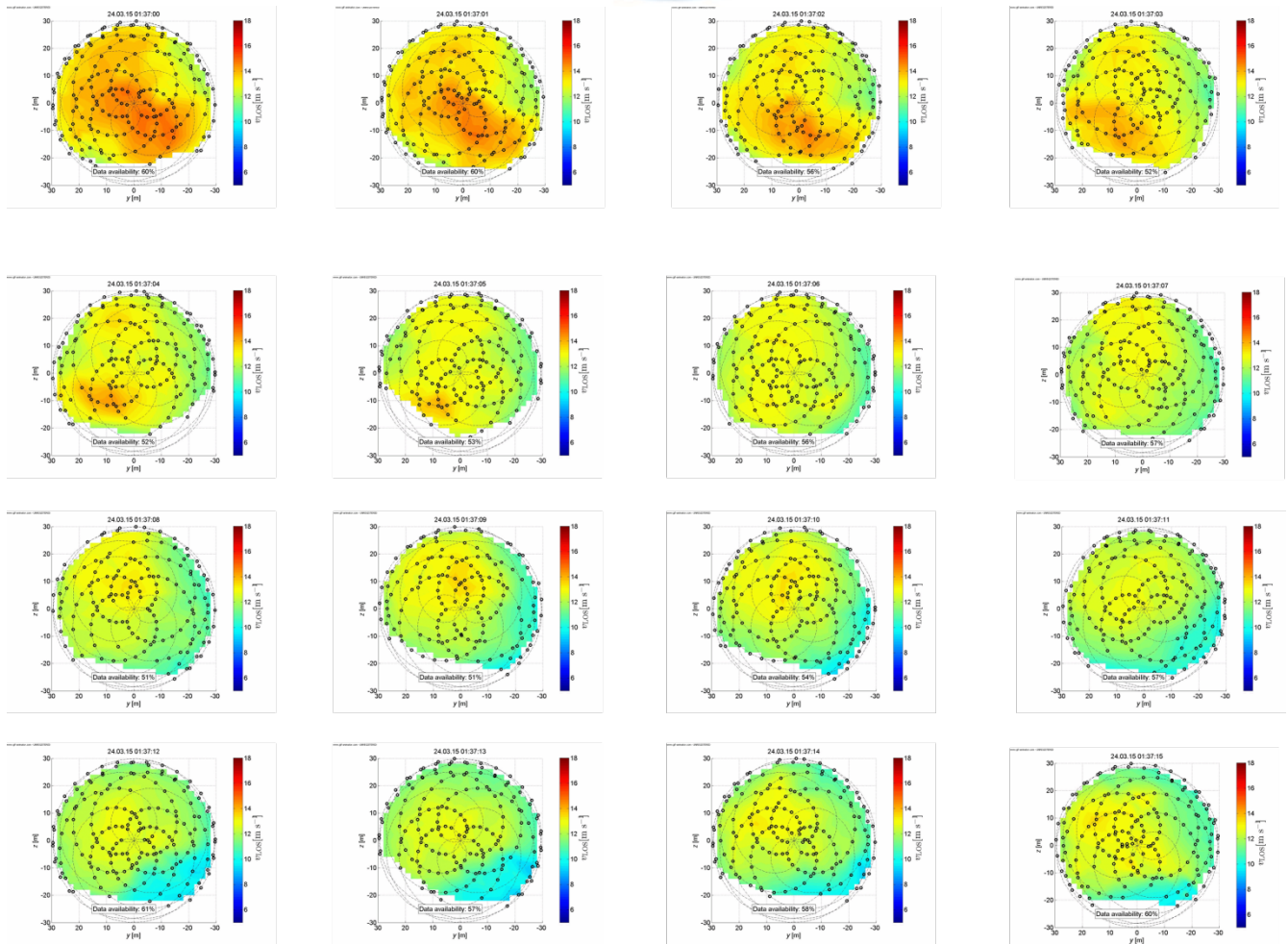


Fig.48. [Left]: Spinner Lidar scanning pattern in the wake of the V27 test turbine at the SWiFT site, overlaid on interpolated line-of-sight speed measurements; [Middle]: Line-of-sight wind speeds measured by the Spinner Lidar on Dec 15<sup>th</sup> 2016 20:31:00 to 20:31:02 at 66.2 m downwind distance, interpolated on a 1x1 m grid facing the turbine, i.e. the turbine is behind the frame. [Right]: The corresponding Lincom reconstructed axial wind component,  $u(y, z)$ .

At SWiFT the purpose of deploying the DTU Spinner Lidar was to measure the response of a V27 turbine wake to varying inflow conditions and turbine operating states. Although the fast-scanning Spinner Lidar is able to measure the line-of-sight projected wind speed at up to 400 points per second, a single lidar is in principle never able to measure all three wind components ( $u, v, w$ ) in the scan plane at the same time. This limitation is often referred to as the “lidar cyclops syndrome”. However, by applying the measured line-of-sight wind speed data as boundary conditions for a fast linearized Navier-Stokes CFD code, referred to as the LINCOM model, 3D wind vector wind fields consistent



with the Spinner Lidars line-of sight measurements and containing all three wind components ( $u$ ,  $v$ ,  $w$ ) can be reconstructed

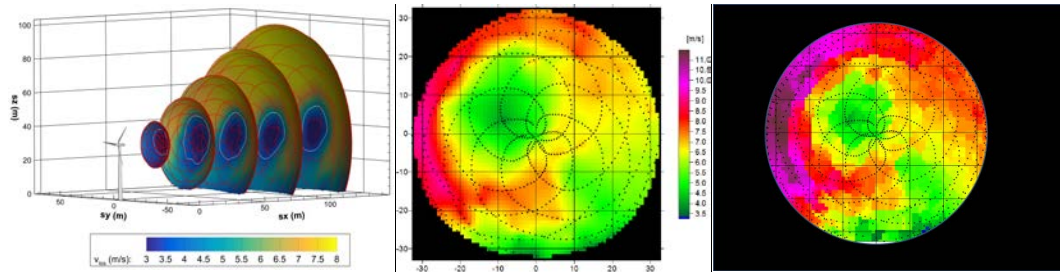


Fig.49. [Left]: Spinner Lidar scanning pattern in the wake of the V27 test turbine at the SWiFT site, overlaid on interpolated line-of-sight speed measurements; [Middle]: Line-of-sight wind speeds measured by the Spinner Lidar on Dec 15<sup>th</sup> 2016 20:31:00 to 20:31:02 at 66.2 m downwind distance, interpolated on a 1x1 m grid facing the turbine, i.e. the turbine is behind the frame. [Right]: The corresponding Lincom reconstructed axial wind component,  $u(y, z)$ .

It has been demonstrated that a single scanning Spinner Lidar mounted on the turbine in the spinner, on the nacelle looking forward, and also installed in the aft looking at the wake flow, in combination with the developed wind field reconstruction methodology can be used to determine the 3D wind components in the inflow as well as in the wake.



## 5.0 Spinner Anemometer based Feed Forward Control (DTU)

### Inflow-based flap control on the two-bladed DTU 10MW RWT on the semi-floater

The post-processed spinner anemometer measurement data presented in the previous section have been analyzed in order to be utilized for inflow-based control simulations. The 10-min average values of the (free-stream derived) wind speed and turbulence intensity from the spinner anemometer post-processed measurement data are shown in Figure 50 and Figure 51. The average turbulence intensity values per wind speed (Figure 52) are then utilized as input for the simulations utilizing inflow-based flap control.

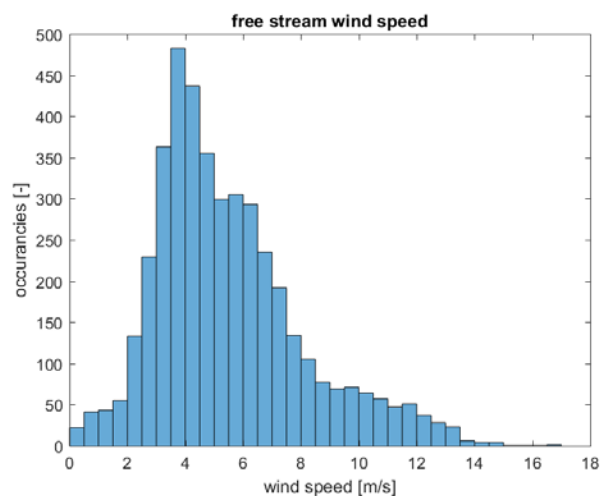


Figure 50 - Wind speed distribution of 10-min average spinner anemometer data samples.

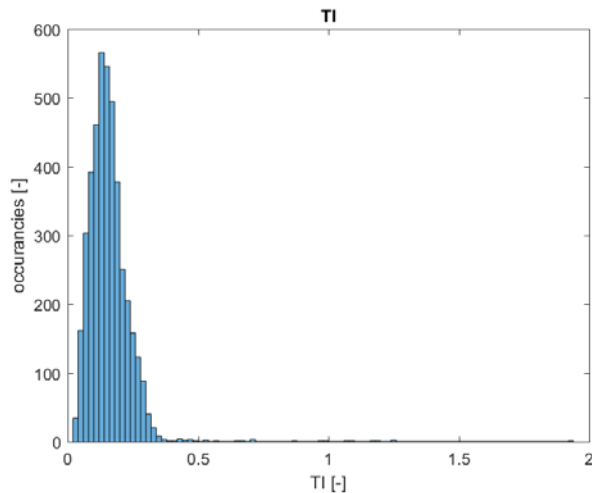


Figure 51 - Turbulence intensity distribution of 10-min average spinner anemometer data samples.

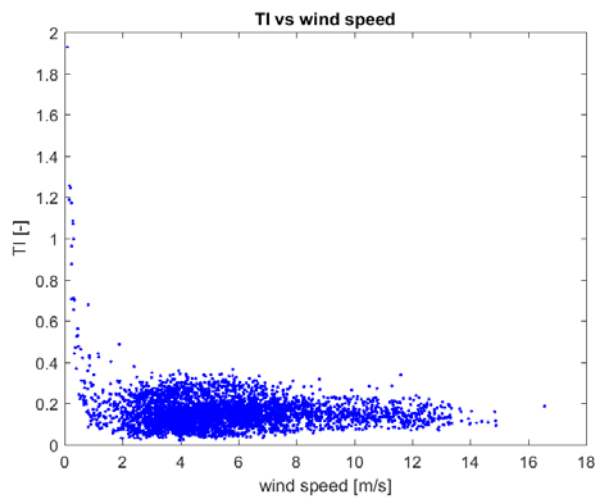


Figure 52 - Turbulence intensity vs wind speed distribution of 10-min average spinner anemometer data samples.

Normal power production DLC1.2 cases are simulated with no wind or wave misalignment, incorporating the derived turbulence characteristics from the spinner anemometer data, for the case of the two-bladed DTU 10MW RWT on the semi-floater. The incorporated flap controller is described in the first section of this report and it consists of a flap scheduling for below rated operating, targeting at increasing power output, and an on-off flap target for increased turbulence operation above rated. The block diagram of the flap controller is shown, in relation to the main controller, sensors and actuators (Figure 3). The effect of the below-rated part of the controller is shown in Figure 53 and Figure 54,



where it is seen that the (collective) flap targets optimal settings, increasing with wind speed, resulting in increase power capture. This results in a gain of +0.54% in AEP for class IA conditions.

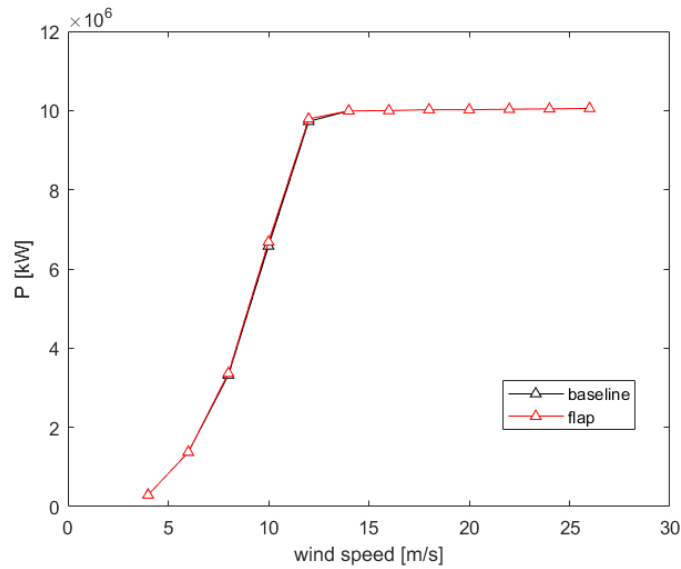


Figure 53 - Comparison of power curves – baseline vs flaps (semi-floater).

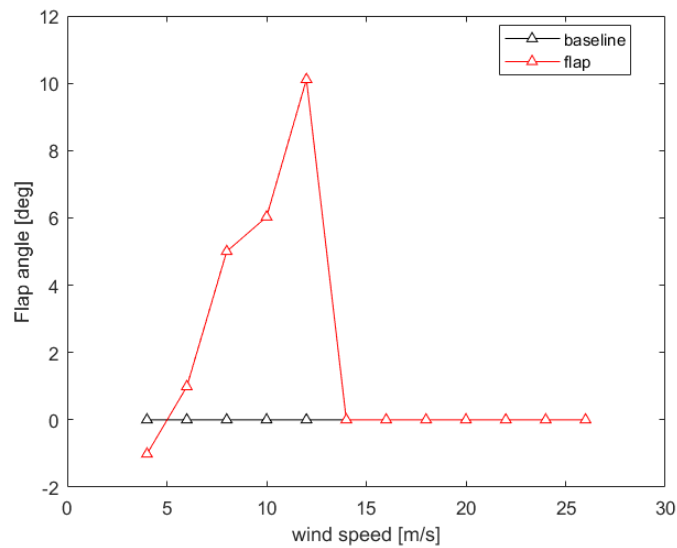


Figure 54 - Comparison of average flap angle – baseline vs flaps (semi-floater).



The effect of the above-rated part of the controller is shown in terms of lifetime fatigue load (Figure 55) and ultimate load (Figure 56) comparisons. It is seen that, some of the load channels lifetime fatigue and ultimate levels are largely reduced up to 23% and 13% respectively.

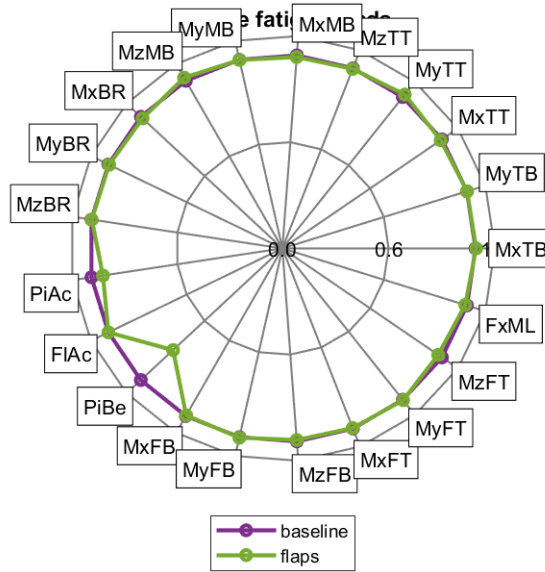


Figure 55 - Comparison of lifetime fatigue loads – baseline vs flaps (semi-floater).

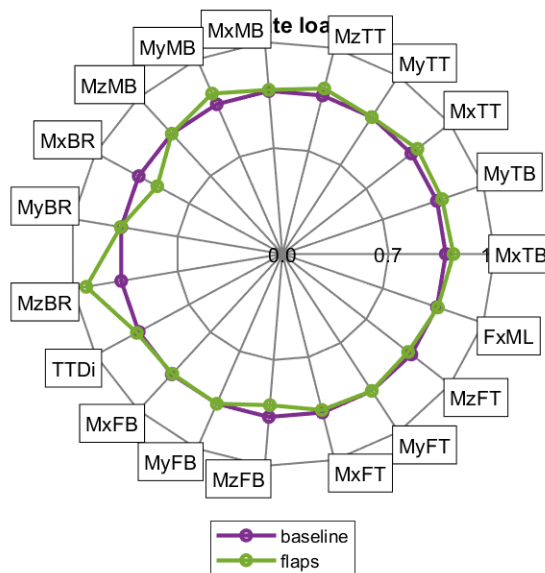


Figure 56 - Comparison of ultimate loads – baseline vs flaps (semi-floater).



## 6.0 Stochastic Embedded Gust Simulations for Design Loads (TUD)

### Introduction

Constrained stochastic simulation (D1.12) is a method that allows the user to generate extreme events in 3D turbulent wind fields. In addition, the probability associated with local maxima and minima can be derived analytically. This means that load cases containing the 50-year gust can be set up directly, without having to generate 50 years of turbulence.

Having full control over the wind field offers great potential. First, it makes it possible to study the interaction between the rotor and extreme gusts (which would otherwise naturally occur in very long time series). Second, it can be used to reconstruct the velocity field around lidar measurements. And, finally, they open the door for very efficient extreme load predictions when coupled to importance sampling methods. These applications will be discussed in detail in the following sections.

What is presented here is a brief overview of the work conducted in the scope of D1.43. The full extent of TU Delft's contribution to D1.12 and D1.43 is compiled in a PhD thesis:

Bos, R. (2017). *Extreme gusts and their role in wind turbine design*. PhD thesis. Delft University of Technology.

### Response to extreme gusts

Compared to, for example, the IEC extreme operating gust, the gusts generated by constrained stochastic simulation are bounded in space and can be positioned anywhere in the wind field. To assess the impact this has on a turbine—most notably the blade root flapwise moments—a large number of these gusts are generated at various locations on the rotor disk.

#### Set-up

As an example, we consider the DTU 10 MW with the baseline controller in Bladed v4.4. Based on the steady thrust and pitch curve, we expect that the rated wind speed of  $\bar{U} = 11.4$  m/s is the point at which the turbine is most susceptible to high gust loads. A severe gust is set up by taking a spheroidal volume with a length of  $2\bar{U}$  and a diameter of 25 m. Based on the theory of D1.12, this corresponds to a 50-year amplitude of 11.0 m/s.

A  $64 \times 64$ , 4-Hz grid is set up with a width and height of 268.8 m ( $= 8L$ ). Each simulation is run for 2 minutes, of which the first minute is discarded to avoid the start-up transients. The gust arrives around the 24-s mark, but varies within a period of  $(2\pi/\Omega)/3$  to make sure that every possible blade position is accounted for. The gusts are positioned uniformly over the frontal plane at  $32 \times 32$  positions, each with 9 seeds, resulting in a total of 9,216 simulations.



## Response in the yz-plane

Figure 57 shows the tower overturning and blade flapwise bending moments as a function of the gust landing on a range of  $y$ - and  $z$ -positions. In both cases, the upper half of the rotor disk is the most vulnerable part, which is due to the wind shear profile. When added to the gust velocity, it causes high apparent wind speeds and higher angles of attack near the zero azimuth position. For the tower overturning moment, the gusts landing higher up have an even bigger impact due to the longer arm with respect to the tower base.

In addition, there is also some asymmetry in the lateral plane. We investigated this by feeding the mean gust shape to a simplified, fixed speed, fixed pitch model of the DTU 10 MW rotor. This mean gust shape is retrieved from the expected value of Equation (2.5) of the D1.12 report; that is,

$$\mathbf{n}_c = \mathbf{A}^*(\mathbf{A}\mathbf{A}^*)^{-1}\mathbf{b}. \quad (7)$$

Using the rotationally sampled velocity signals, we found that the asymmetry is caused by the correlation tensor prescribed by the Mann model. Positive streamwise amplitudes are often accompanied by negative (downward) vertical velocities. Therefore, a blade hit by a gust during its downstroke will also experience a decrease in the azimuthal velocity component. This causes stronger angle of attack changes with higher (dynamic) lift coefficients. Despite the fact that the total velocity component is slightly reduced, the total lift force on the blade is higher. Of course, the opposite happens during an upstroke. The result is that the right side of the rotor (when viewed from upwind) is slightly more susceptible to high gust loads.

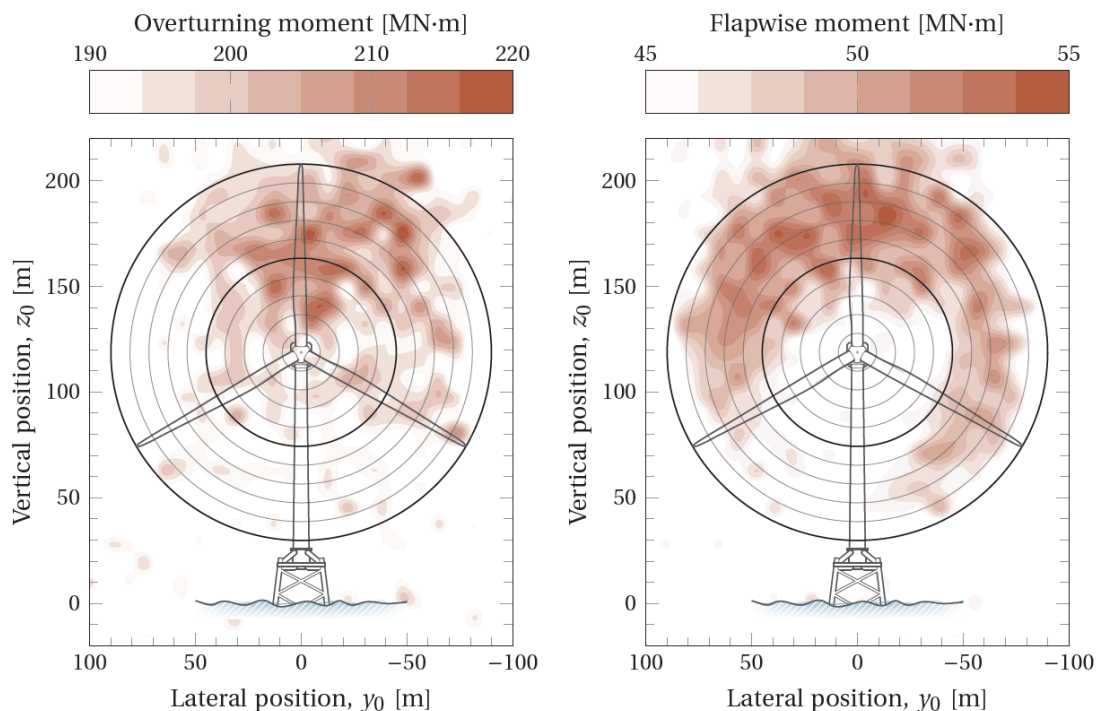
Still, there are a lot of positions—think of the blade root—where a severe gust does not trigger any significant load whatsoever. This has an effect on the 50-year load level, since the probability of a gust landing on a certain position has to be included in the load calculation. Therefore, the expected flapwise bending moment associated with this 50-year event (i.e., the risk) is not very high (only 41.0 MN·m). The actual 50-year load level may not be obtained directly from a 50-year gust. It is an extensive process where a designer has to take into account the contributions of weaker and stronger gusts, landing at different blade positions.

## Response in the time domain

The response in the time domain is plotted in Figure 58 and Figure 59. The maximum bending moments lag behind the maximum amplitude by roughly 5 seconds, although at that time the longitudinal wind speed is still well above the mean. In most cases (at least 95%), the baseline controller handles the gust well (see Figure 58b and 58c). However, there are cases where the gust does trigger high bending moments. One of those is depicted in Figure 59. During that specific event, the rotor was running below the rated speed. This meant that there was still some room for the rotor to speed up before the pitch system had to intervene. The controller indeed managed to limit the torque overshoot, but not before the turbine experienced high maximum bending moments.

Compared to gusts with a fully uniform inflow over the  $yz$ -plane (e.g., the IEC extreme operating gust), there are some important differences. Firstly, a local velocity peak also means that the gust loads do not follow the time signature of the gust, as would be the case with the IEC extreme operating gust. Instead, blade loads and tower loads respectively follow 1P and 3P frequencies.

It is difficult to identify gusts and limit loads based on the high-speed shaft (HSS) torque or other rotor-effective input signals. With blades the size of the DTU 10 MW, gusts are local velocity peaks that often only affect one blade at a time. Therefore, high bending moment acting on a single blade root is not necessarily accompanied by high torque. For the same reason, high blade root moments do not always mean high tower moments. Because the angle of attack changes are very local, collective pitch is a very crude measure and can lead to adverse results in the case of negative gust amplitudes. In the case of the NREL 5 MW machine with the baseline controller (see Figure 59), this turned out to be solely responsible for the 50-year load. A better solution is to rely on individual pitch, distributed



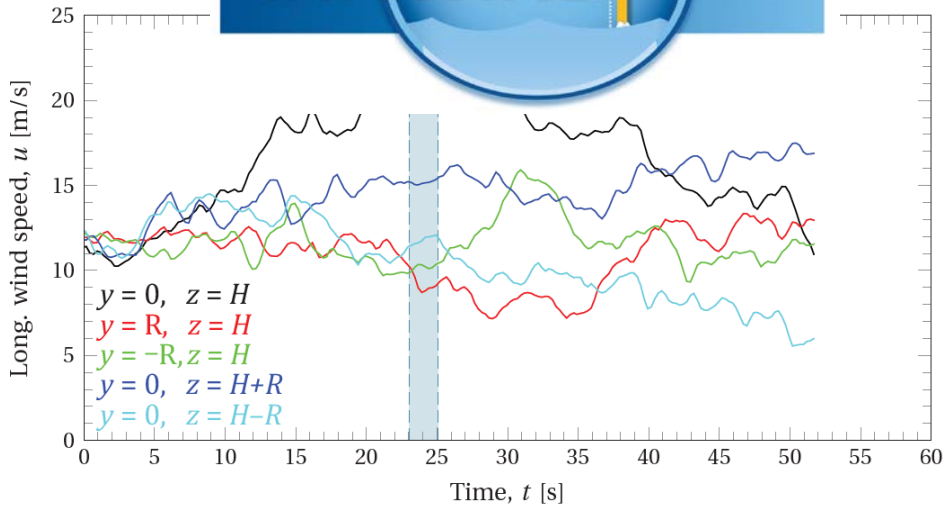
(a): Tower base overturning moment.

(b): Blade root flapwise moment.

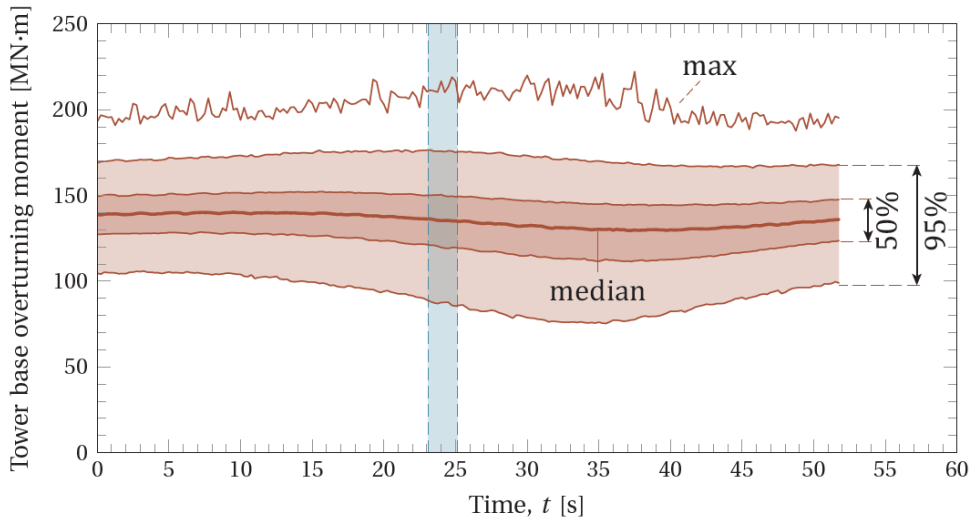
Figure 57: Bending loads, depending on the lateral and vertical gust position.



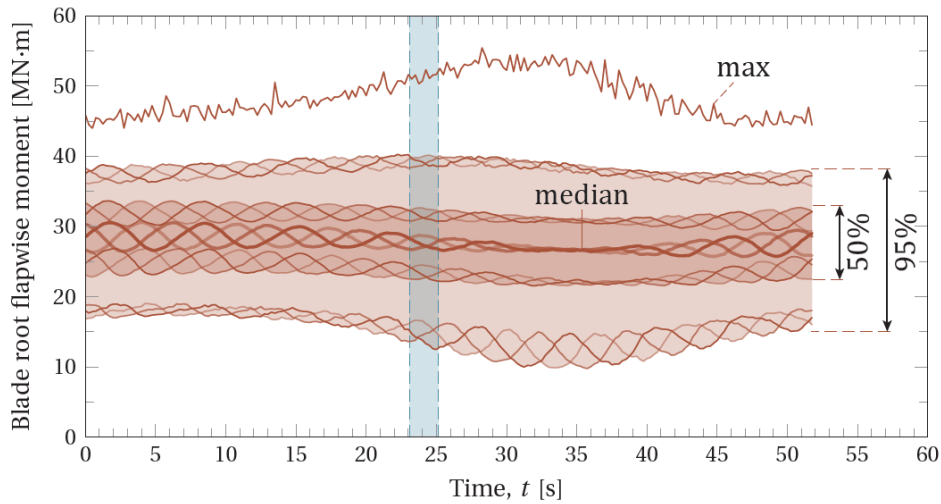
control, and/or lidar-assisted control.



(a): Longitudinal wind speed with the gust centers marked with the shaded area. Here, the gust is centered on the hub at 24 s.

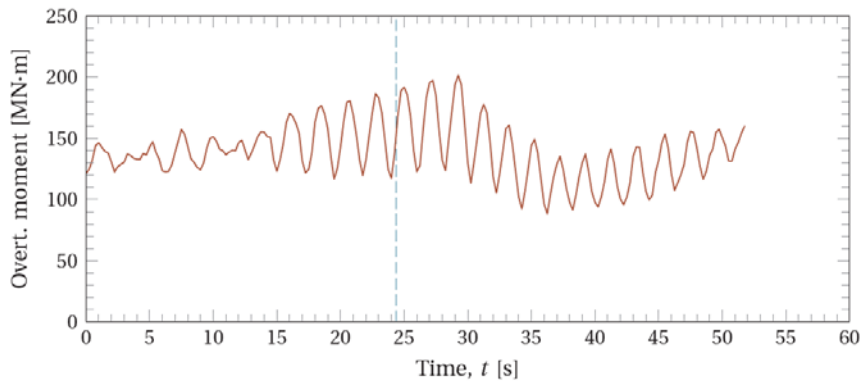


(b): Medians, confidence intervals and maxima of the tower base overturning moments.

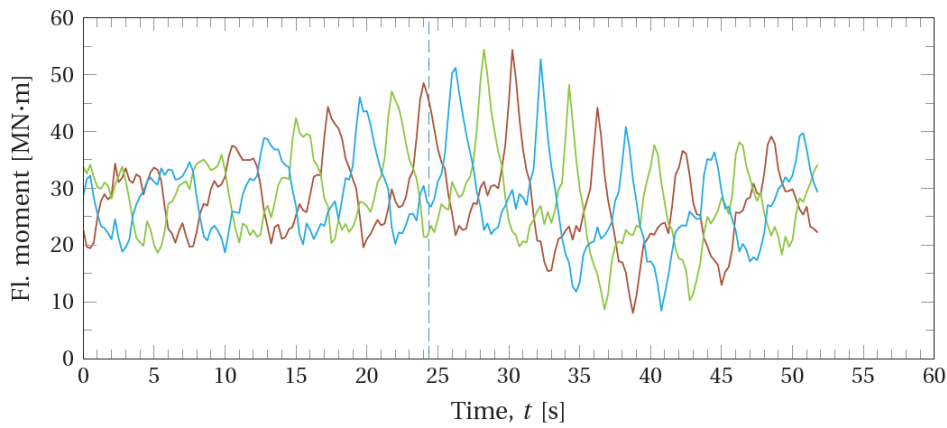


(c): Medians, confidence intervals and maxima of the blade root flapwise bending moments.

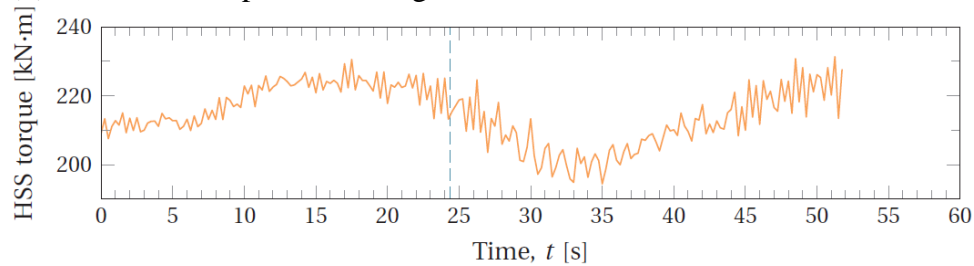
Figure 58: Time series of all 9,216 simulated load cases.



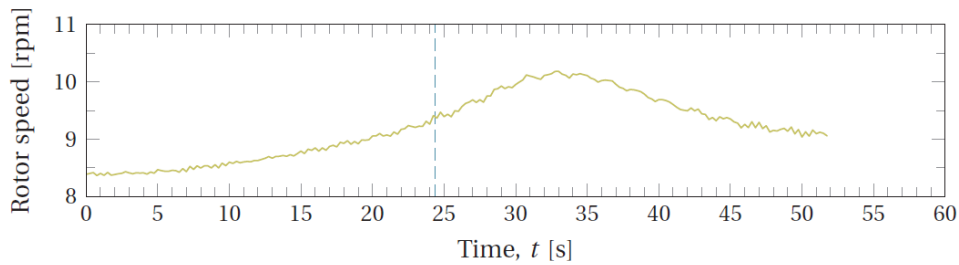
**(a):** Tower base overturning moment.



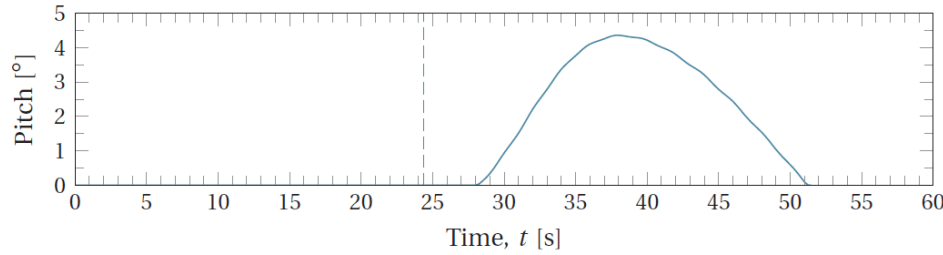
**(b):** Blade root flapwise bending moments.



**(c):** High-speed shaft torque.



**(d):** Rotor speed (low-speed shaft).



(e): Collective pitch angle.

**Figure 59:** Time series belonging to the maximum bending moment (55.4 MN·m, with the extreme gust positioned at  $t_0 = 24.5$  s,  $y_0 = -13$  m,  $z_0 = 184$  m).

### Application to Lidar-assisted control

Another interesting application is the reconstruction of lidar data. On the assumption that turbulence is a stationary, homogeneous, and Gaussian process, the statistics of any 3D spectral model can be used to give the best possible estimate for the velocity field. This was demonstrated using data from the LAWINE project (concluded in October 2016). More details of this method can be found in the paper [24]

#### Set-up

The set-up consisted of an Avent-Lidar 5-beam pulsed lidar prototype that was mounted on the nacelle of a Darwind XD115-5MW wind turbine on the test site of ECN (see Figure 60). It provides data of ten range gates simultaneously (50—185 m upwind), while cycling between the five beam positions (0—4) every 0.25 s.

The lidar does not provide a perfect point measurement, but more of a weighted average. This is modeled by a Gaussian pulse shape [25]:

$$w(r) = \frac{1}{2\Delta R} \left[ \operatorname{erf}\left(\frac{R - r + \frac{1}{2}\Delta R}{\Delta Z}\right) - \operatorname{erf}\left(\frac{R - r - \frac{1}{2}\Delta R}{\Delta Z}\right) \right] \quad (8)$$

where  $R$  is the distance to the range gate,  $\Delta R$  the distance between the range gates,  $\Delta Z$  the  $e^{-1}$  radius of the pulse, and  $\operatorname{erf}(x)$  is the error function. The  $e^{-1}$  radius is derived from the full-width-at-half-maximum pulse width (FWHM):

$$\Delta Z = \frac{\text{FWHM}}{2\sqrt{\ln 2}}, \quad (9)$$

with  $\text{FWHM} = 30$  m for this set-up. Under the assumption that the streamwise velocity component is the dominant one (i.e.,  $u \gg v, w$ ), the line-of-sight velocity at a given point  $j$  is:

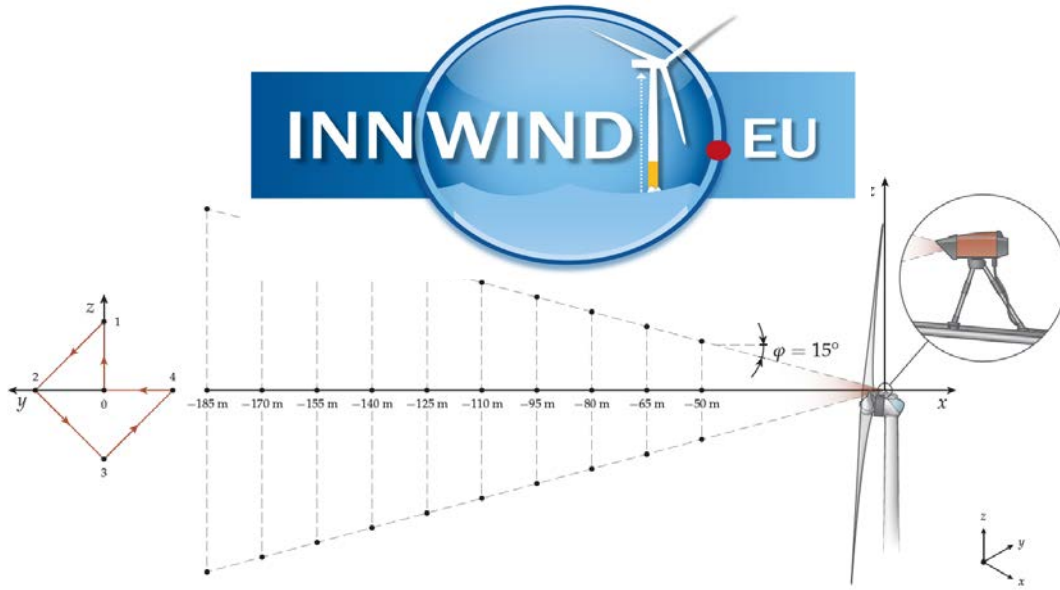


Figure 60: Sketch of the pulsed lidar system mounted on the nacelle of a Darwind XD115-5MW wind turbine.

$$u_{\text{LOS},j} = \cos \varphi_j \int u(x_j + r, y_j, z_j) w(r) dr, \quad (10)$$

where  $\varphi$  is the beam angle.

### 1.1.1 Velocity field reconstruction

The 3D velocity field that surrounds the collection of  $n$  measurements is a conditional field:

$$\hat{\mathbf{u}}(\mathbf{x}) = \left\{ \mathbf{u}(\mathbf{x}) \mid \int u(x_1 + r, y_1, z_1) w(r) dr = \frac{u_{\text{LOS},1}}{\cos \varphi_1}, \dots, \int u(x_n + r, y_n, z_n) w(r) dr = \frac{u_{\text{LOS},n}}{\cos \varphi_n} \right\}. \quad (11)$$

Using the theory of D1.12, it is possible to derive the set of velocity fields that match the set of measurements, while adhering to the statistics of the spectral tensor,  $\Phi(\boldsymbol{\kappa})$ . For this, we assume that  $\mathbf{u}(\mathbf{x})$  is stationary, homogeneous, and Gaussian and can be constructed by a Fourier series:

$$\mathbf{u}(\mathbf{x}) = \bar{\mathbf{u}}(\mathbf{x}) + \sum_{\boldsymbol{\kappa}} \mathbf{C}(\boldsymbol{\kappa}) \mathbf{n}(\boldsymbol{\kappa}) e^{i\boldsymbol{\kappa} \cdot \mathbf{x}}, \quad (12)$$

where  $\mathbf{u} = [u, v, w]^T$  is a velocity vector,  $\mathbf{x} = [x, y, z]^T$  a position vector,  $\boldsymbol{\kappa} = [\kappa_x, \kappa_y, \kappa_z]^T$  the wave number vector,  $\mathbf{C}(\boldsymbol{\kappa})$  a correlation tensor (obtained by a Cholesky decomposition of the spectral tensor; e.g., see (B.13) of IEC 61400-1, 2<sup>nd</sup> edn., Appendix B), and  $\mathbf{n}(\boldsymbol{\kappa}) \sim CN(0, \mathbf{I}_3)$  a vector of complex-normal distributed coefficients. Moreover,  $\bar{\mathbf{u}}(\mathbf{x})$  denotes the (time-invariant) mean wind speed component. This can be written as a matrix multiplication according to:

$$\mathbf{u}(\mathbf{x}) - \bar{\mathbf{u}}(\mathbf{x}) = \boldsymbol{\Psi} \mathbf{n}, \quad (13)$$

where

$$\boldsymbol{\Psi} = [\dots, \mathbf{C}(\boldsymbol{\kappa}_{j-1}) e^{i\boldsymbol{\kappa}_{j-1} \cdot \mathbf{x}}, \mathbf{C}(\boldsymbol{\kappa}_j) e^{i\boldsymbol{\kappa}_j \cdot \mathbf{x}}, \mathbf{C}(\boldsymbol{\kappa}_{j+1}) e^{i\boldsymbol{\kappa}_{j+1} \cdot \mathbf{x}}, \dots],$$

is a Fourier transform matrix and where



$$\mathbf{n} = \begin{bmatrix} \vdots \\ \mathbf{n}(\boldsymbol{\kappa}_{j-1}) \\ \mathbf{n}(\boldsymbol{\kappa}_j) \\ \mathbf{n}(\boldsymbol{\kappa}_{j+1}) \\ \vdots \end{bmatrix},$$

is a one-dimensional white noise vector. From (2.8), the streamwise velocity component is easily obtained by taking the first row; i.e.,

$$u(\mathbf{x}) - \bar{u}(\mathbf{x}) = \Psi_u \mathbf{n}, \quad (14)$$

where

$$\Psi_u = [\dots, [C_{uu}(\boldsymbol{\kappa}_j), C_{uv}(\boldsymbol{\kappa}_j), C_{uw}(\boldsymbol{\kappa}_j)]e^{i\boldsymbol{\kappa}_j \cdot \mathbf{x}}, \dots].$$

What now follows is the same approach used in Section 2.4 of the D1.12 report. When the complete set of lidar measurements,  $1, \dots, n$ , are stored in a one-dimensional vector,  $\mathbf{b}$ :

$$\mathbf{b} = \begin{bmatrix} u_{\text{LOS},1}/\cos \varphi_1 - \bar{u}(\mathbf{x}_1) \\ u_{\text{LOS},2}/\cos \varphi_2 - \bar{u}(\mathbf{x}_2) \\ \vdots \\ u_{\text{LOS},n}/\cos \varphi_n - \bar{u}(\mathbf{x}_n) \end{bmatrix}, \quad )$$

Equation (2.5) can be rewritten as a linear system:

$$\hat{\mathbf{u}}(\mathbf{x}) = \Psi \{\mathbf{n} | \mathbf{Y}\mathbf{n} = \mathbf{b}\}, \quad (15)$$

where the matrix  $\mathbf{Y}$  follows from stacking the matrix (2.11) and filtering it with the kernel  $w(r)$ :

$$\mathbf{Y} = \begin{bmatrix} \dots, W(\kappa_j)[C_{uu}(\boldsymbol{\kappa}_j), C_{uv}(\boldsymbol{\kappa}_j), C_{uw}(\boldsymbol{\kappa}_j)]e^{i\boldsymbol{\kappa}_j \cdot \mathbf{x}_1}, \dots \\ \dots, W(\kappa_j)[C_{uu}(\boldsymbol{\kappa}_j), C_{uv}(\boldsymbol{\kappa}_j), C_{uw}(\boldsymbol{\kappa}_j)]e^{i\boldsymbol{\kappa}_j \cdot \mathbf{x}_2}, \dots \\ \vdots \\ \dots, W(\kappa_j)[C_{uu}(\boldsymbol{\kappa}_j), C_{uv}(\boldsymbol{\kappa}_j), C_{uw}(\boldsymbol{\kappa}_j)]e^{i\boldsymbol{\kappa}_j \cdot \mathbf{x}_n}, \dots \end{bmatrix}.$$

where  $W(\kappa_j)$  is the Fourier transform of  $w(r)$ .

Now, under the strict assumption of Gaussianity, the statistics of  $\hat{\mathbf{u}}(\mathbf{x})$  can be derived analytically:

$$E[\hat{\mathbf{u}}(\mathbf{x})] = \bar{\mathbf{u}}(\mathbf{x}) + \Psi \mathbf{Y}^* (\mathbf{Y} \mathbf{Y}^*)^{-1} \mathbf{b}, \quad (16)$$

$$\text{var}[\hat{\mathbf{u}}(\mathbf{x})] = \Psi \Psi^* - \Psi \mathbf{Y}^* (\mathbf{Y} \mathbf{Y}^*)^{-1} \mathbf{Y} \Psi^*, \quad (17)$$

where  $*$  denotes a conjugate transpose. This means that  $E[\hat{\mathbf{u}}(\mathbf{x})]$  is the expected (mean) velocity field surrounding the measurements. Furthermore,  $\text{var}[\hat{\mathbf{u}}(\mathbf{x})]$  is the variance. At the measurement points, the variance is zero (i.e., the velocity is always equal to the measurement), while infinitely far away, the



variance should be equal to the square of the turbulence intensity (i.e., the best guess with only the ten-minute statistics). The process can be best compared to *kriging*—which was originally applied in geostatistics—where the variance is representative of the uncertainty.

A gust measured in the field

This method was applied to a gust that was picked up by the lidar’s center beam on 22 December 2013. It was the most severe event in the 1.5-year data set, while still being undisturbed from the surrounding turbines and met masts.

Assuming that the terrain is relatively flat and homogeneous, a neutral wind shear profile was fitted to the ten-minute mean wind speeds measured at the positions 0, 1 and 3 at  $r = -140$  m:

$$\bar{u}(z) = \bar{u}(z_{\text{ref}}) \frac{\ln(z/z_0)}{\ln(z/z_{\text{ref}})}, \quad (18)$$

which resulted in a roughness length of  $z_0 = 0.55$  m, matching the site fairly well [28]. In addition, Mann’s spectral tensor was set up with  $L \approx 25$  m (estimated from the low-frequency part of the lidar spectrum),  $\Gamma = 3$  (for neutral conditions) [29] and  $\alpha \epsilon^{2/3} \approx 0.16 \text{ m}^{4/3}/\text{s}^2$ . The latter was found by matching the longitudinal variance of the center beam measurements to the filtered spectral tensor:

$$\int W^2(\kappa_x) \Phi_{uu}(\boldsymbol{\kappa}) d\boldsymbol{\kappa} \approx \sigma_{u,\text{LOS}}^2, \quad (19)$$

Figure 61 shows two cross-sections of the fields  $E[\hat{\mathbf{u}}(\mathbf{x})]$  and  $\text{var}[\hat{\mathbf{u}}(\mathbf{x})]$ . The low-frequency parts of the gust, which hold most of the momentum content, are captured fairly well. The variance is the lowest along the directions of the beams, as should be expected. However, it never reaches complete zero due to the range weighting, so part of this variance has to account for the high frequencies that are not captured by the lidar.

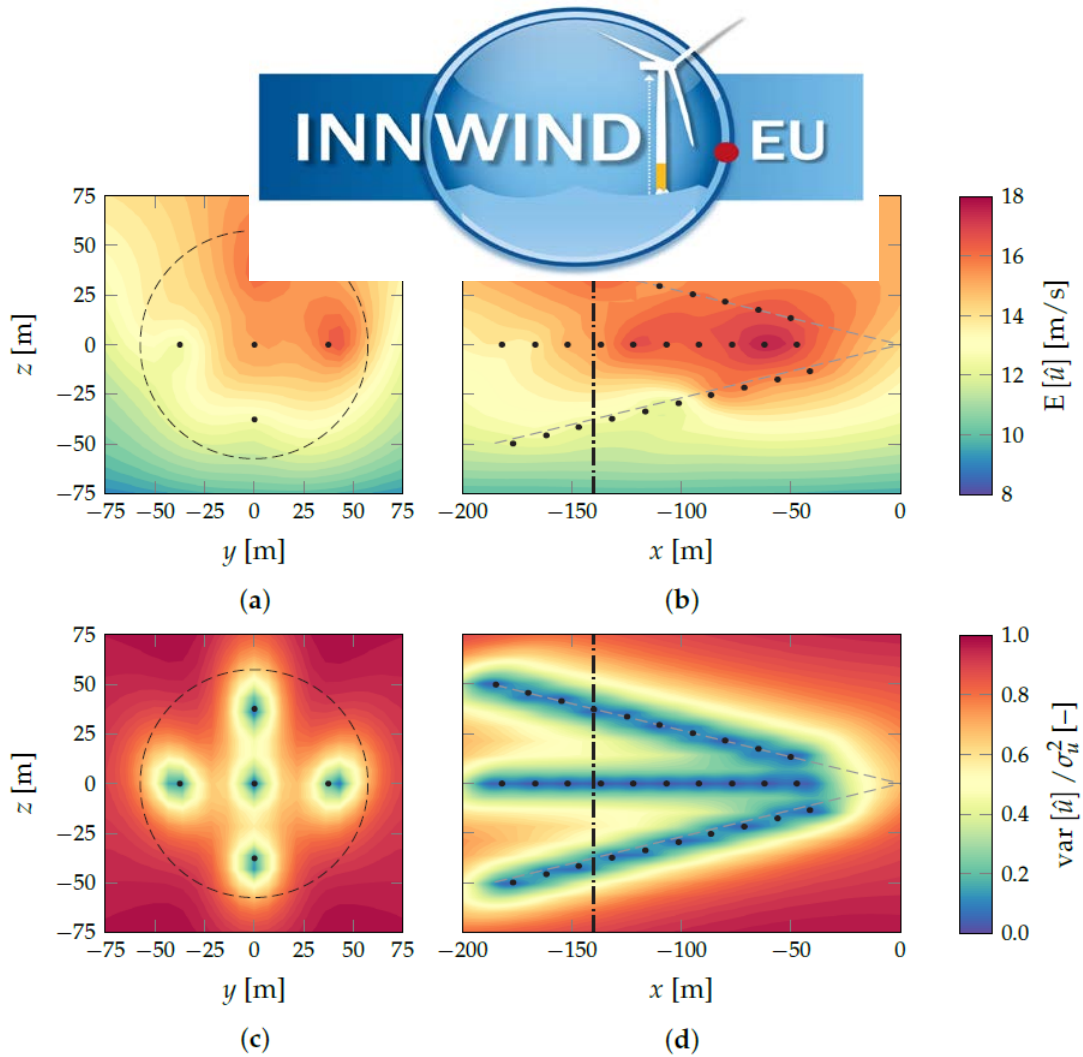


Figure 61: Expected velocity fields in the yz- (a) and xz-planes (b), together with the normalized variance in the yz- (c) and xz-planes (d).

### 1.1.2 Construction of a control input signal

The expected velocity field, together with its variance, can be used to construct an input signal for a gust controller. It relies on the notion that, under Taylor's frozen turbulence hypothesis, it holds that

$$\begin{aligned} \rho \bar{u} \frac{\partial u}{\partial x} &= -\frac{\partial p}{\partial x}, \\ \frac{\partial}{\partial x} (\rho \bar{u} u + p) &= 0, \\ \rho \bar{u} u + p &= \text{const.} \end{aligned} \quad (20)$$

Here,  $\rho$  is the air density and  $p$  is the static atmospheric pressure. The along-wind force, pushing on the yz-plane at a distance  $r$  upwind, is found by integrating the dynamic pressure term,  $\rho \bar{u} u$ , over a surface,  $A$ :



$$F(t; r) = \rho \iint_A \bar{u}(r, y, z) u(r, y, z, t) dy dz. \quad (21)$$

Because  $\bar{u}(\mathbf{x})$  is constant and  $u(\mathbf{x}, t)$  is a Gaussian field, it must follow that  $F(t; r)$  is also Gaussian. This is convenient, since it allows us to also derive its statistics, based on the statistics of a reconstructed velocity field,  $\hat{u}(\mathbf{x}, t)$ :

$$E[\hat{F}(t; r)] = \rho \iint_A \bar{u}(r, y, z) E[\hat{u}(r, y, z, t)] dy dz, \quad (22)$$

$$\text{var}[\hat{F}(t; r)] = \rho^2 A \iint_A \bar{u}^2(r, y, z) \text{var}[\hat{u}(r, y, z, t)] dy dz. \quad (23)$$

This along-wind force is related to the loads on the structure and can be used for gust control. For example, with 97.7% certainty, the along-wind force will stay under the level  $\hat{F} + 2\sigma_{\hat{F}}$  (see Figure 6). The uncertainty is a function of the turbulence coherence and the amount of available measurement points, which will vary due to the technical availability of the lidar and the blades passing in front of the eye. Therefore, a signal  $\hat{F} + n\sigma_{\hat{F}}$  is a rather objective way of judging the lidar input.

The method was cross-checked with a similar input signal: the rotor-effective wind speed,  $U_{\text{eff}}$ , which is a pseudo-signal that is directly derived from the measured rotor torque:

$$Q = \frac{1}{16} \rho C_Q(\theta, \lambda) \pi D^3 U_{\text{eff}}^2, \quad (24)$$

where  $Q$  is the shaft torque,  $C_Q$  the torque coefficient (a function of the pitch angle,  $\theta$ , and tip speed ratio,  $\lambda$ ), and  $D$  the rotor diameter. The rotor-effective wind speed has been proven to be a good input signal for feed-forward control and has been successfully implemented to improve turbine behavior under gust loading [26,27]. Figure 62 shows a direct comparison of the two signals by matching their mains. The rotor-effective wind speed was down sampled to 1 Hz (was 64 Hz) to reduce the noise and focus on the more important low-frequency fluctuations. The 95% range follows from the area enclosed by  $\hat{F} \pm 2\sigma_{\hat{F}}$ . The two signals seem to agree well in a qualitative sense, with the most important up- and downward trends around  $t = 0$  clearly recognizable.

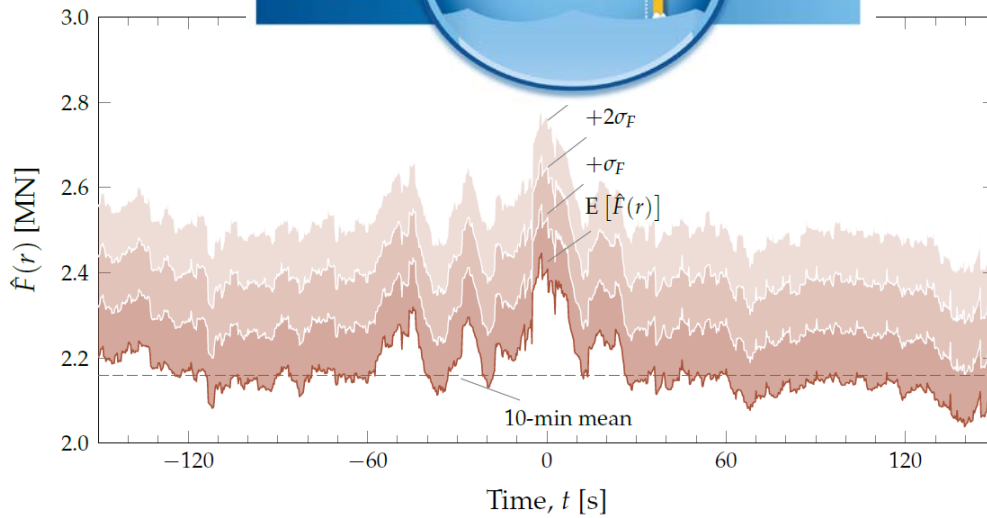


Figure 62: Expected along-wind force belonging to the gust event of Figure 5 at  $r = -140$  m, together with the uncertainty levels.

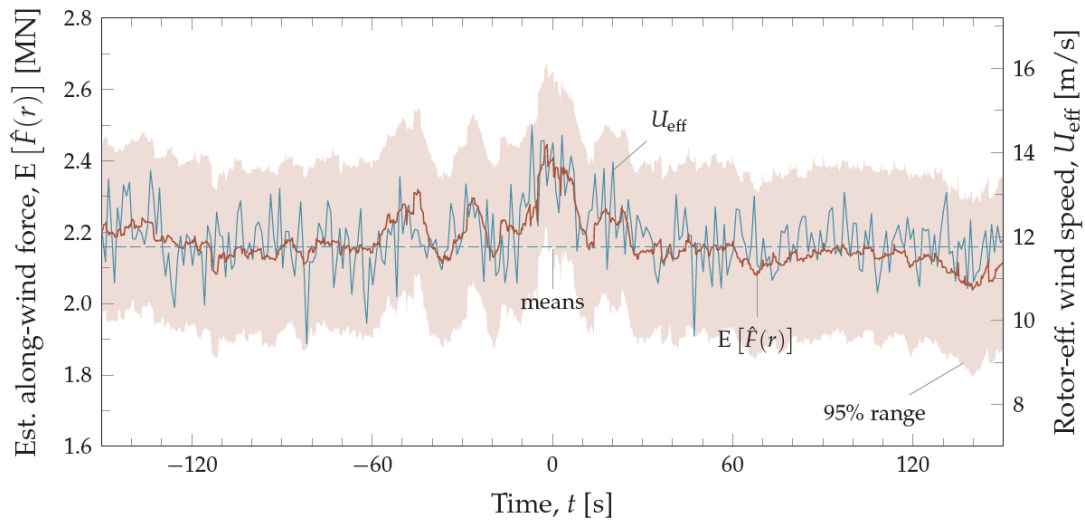


Figure 63: Expected along-wind force belonging to the gust event of Figure 5 at  $r = -140$  m, compared to the rotor-effective wind speed by ECN with a 10.5-s delay to account for advection towards the rotor disk (downsampled to 1 Hz for clarity).

## 1.2 DLC 1.1 extreme load predictions

Probably the most powerful application of constrained stochastic simulation is in the prediction of extreme loads. Extreme loads, most notably the 50-year loads, are difficult to obtain because certain dynamic behavior or controller behavior might only show up in very large sample sizes. This often makes it hard to model the extreme load behavior in cases when the computational budget is limited; for example, in early design phases.



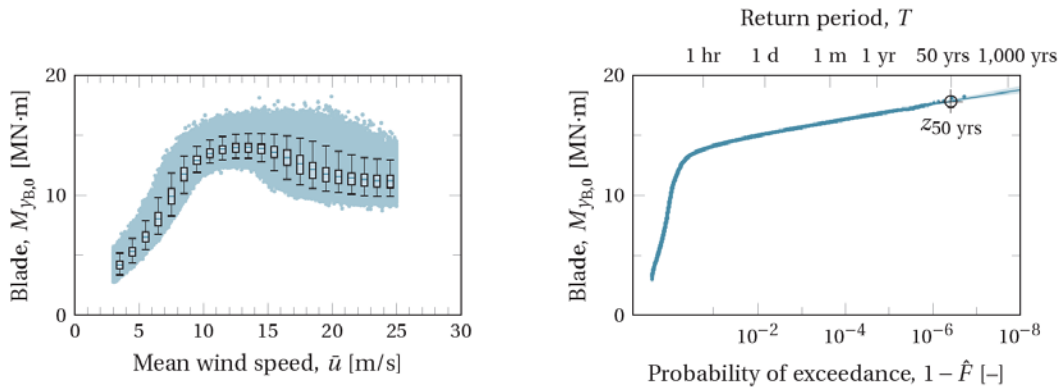
### 1.2.1 Case study: the NREL 5 MW

As a case study, we considered the NREL 5 MW. This was a convenient subject, since a large data set was available with 96 years' worth of extremes [30]. At the same time, it provided a nice insight in the controller behavior in extreme cases. The data set was generated using the onshore version of the NREL 5 MW with the baseline controller, modeled in FAST v7. Wind fields were generated by TurbSim on a 137×137 m, 20×20 grid, with a temporal frequency of 20 Hz, and following an IEC class 1B normal turbulence model. Each simulation was run for 11 minutes, with the first minute discarded to get rid of the start-up transients.

The data set was generated by a crude Monte Carlo method. This means that the mean wind speeds were sampled from the parent Rayleigh distribution and that the extreme load distribution follows naturally from sorting and assigning the appropriate plotting position to the  $i$ th load:

$$\hat{F}(M_{y,i}) = \frac{i}{N+1}, \quad (25)$$

where  $N$  is the sample size. The regions below the cut-in and above cut-out wind speeds can be accounted for by either completing the data set with zero loads or by correcting the load distribution according to



(a): Scatter plot of the entire data set. The edges of the box plots indicate the 25<sup>th</sup> and 75<sup>th</sup> percentiles, the whiskers indicate the 2.5<sup>th</sup> and 97.5<sup>th</sup> percentiles, and the bar shows the medians.

(b): Return level plot, yielding a 50-year extreme of 17.8 MN·m. Longer return periods are obtained by fitting a generalized extreme value distribution. The shaded area marks the 95% confidence interval, which is estimated by resampling the data.

Figure 64: Extreme blade root flapwise moments of the NREL 5 MW reference turbine ( $N = 5 \cdot 10^6$ ).

$$\hat{F}(M_{y,i}) = 1 - \left(1 - \frac{i}{N+1}\right) \int_{\text{cut-in}}^{\text{cut-out}} f(\bar{U}) d\bar{U}. \quad (26)$$



Figure 64 shows the extreme blade root flapwise bending moments. Judging from both the scatter plot (a) and the return level plot (b), the extreme loads seem to originate from relatively high wind speeds in the pitch control regime. It turned out that this was due to a particular weakness in the baseline controller. Strongly negative gust amplitudes would sometimes reduce the wind speed close to the rated wind speed, which causes the turbine to pitch back to zero. When the wind speed recovers, the machine is operating at full thrust in an 18–19-m/s mean wind speed, leading to the high extreme loads (e.g., see Figure 65). When the data set increases in size, the extreme cases appear in even higher wind speeds, since increasingly larger amplitudes are encountered that are able to bring the wind speed back to rated. This also means that, for small sample sizes, the extremes might seem to lie close to the rated

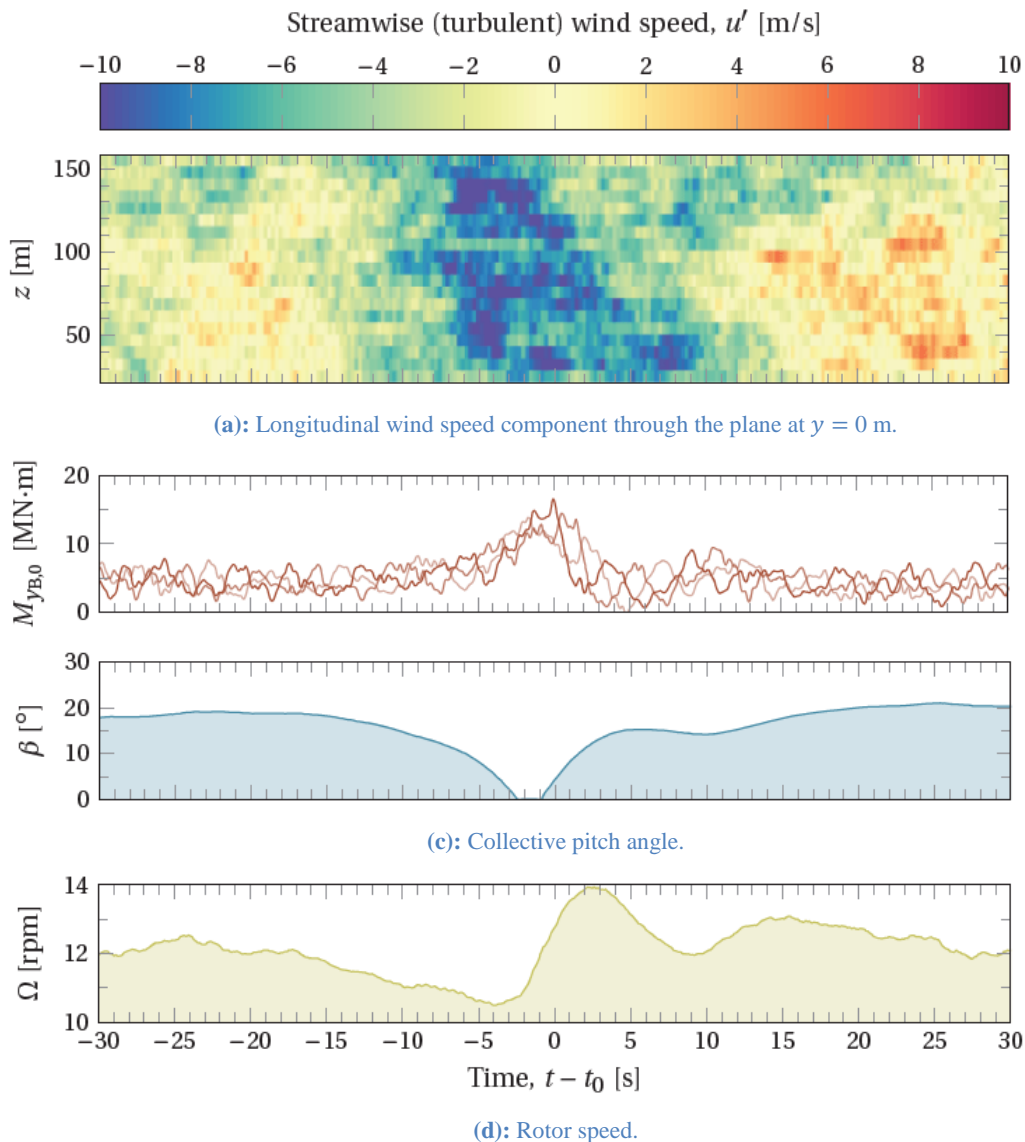


Figure 65: Time series belonging to an extreme flapwise bending moment at  $\bar{U} = 19$  m/s.



wind speed, which is also what is shown by the error bars in Figure 64a.

### An importance sampling method

Not only is it very computationally intensive to establish a 50-year load with sufficient accuracy, it is also very difficult to quantify whether an updated control strategy is able to reduce the 50-year load. A possible solution is to rely on an importance sampling method that uses constrained gusts. The extreme events that cause the behavior shown in Figure 65 can be sampled directly from a distribution  $g(\boldsymbol{\theta})$ . An extreme load distribution then follows from

$$\hat{F}(M_y) = \frac{\sum_{i=1}^N \mathbf{1}(M_{y,i} \leq M_y) \frac{f(\boldsymbol{\theta}_i)}{g(\boldsymbol{\theta}_i)}}{\sum_{i=1}^N \frac{f(\boldsymbol{\theta}_i)}{g(\boldsymbol{\theta}_i)}}, \quad (27)$$

where the probabilities are weighted by a likelihood ratio,  $f(\boldsymbol{\theta})/g(\boldsymbol{\theta})$ . Here,  $\boldsymbol{\theta}$  is a vector in a parameter space,  $f(\boldsymbol{\theta})$  is the parent distribution,  $g(\boldsymbol{\theta})$  is a sampling distribution, and

$$\mathbf{1}(x \in S) = \begin{cases} 1, & \text{if } x \in S, \\ 0, & \text{if } x \notin S, \end{cases} \quad (28)$$

is the indicator function.

Importance sampling can be a very attractive solution when a designer has complete control over the wind field. Instead of running large sample sizes of ten-minute wind fields, the same results can be obtained by only evaluating the response to a small set of extreme gusts, which can be stored in time series of 1—2 minutes.

The critical part of an importance sampling method is always to define a proper sampling distribution. We assume that the extremes loads are dependent on 2 parameters: the mean wind speed,  $\bar{U}$ , and the gust amplitude,  $A$ . The gust position is left unconstrained (i.e., uniformly distributed over the  $yz$ -plane). Then, an initial survey of the parameter space, shown in Figure 66, explains the scatter of Figure 8a. It confirms the suspicion that combinations of high wind speeds and large negative gust amplitudes are responsible for the extreme load behavior.

The probability associated with such gusts are estimated through the *Euler characteristic heuristic*:

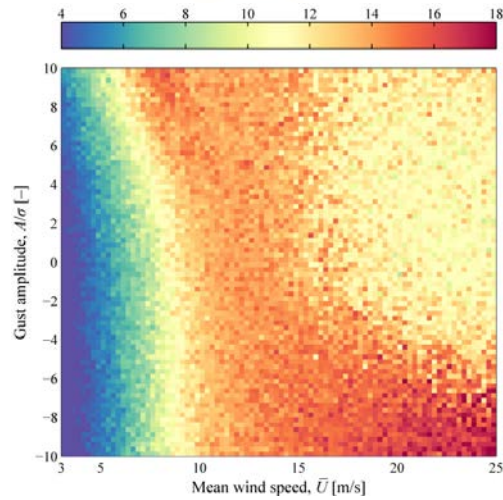


Figure 66: Extreme blade root flapwise moments of the NREL 5 MW reference turbine triggered by point gust amplitudes ( $N = 10^5$ ).

$$f(A) \approx -\frac{d}{dA} E[\varphi(Z_A)], \quad (29)$$

where the expected Euler characteristic,  $E[\varphi(Z_A)]$ , is given by Equation (3.13) of the D1.12 report. Based on Figure 66, two different gust settings are used: (1) a point gust (i.e., exciting a single grid point) and (2) a spheroidal gust with a time scale of 2 s and a lateral diameter of 25 m. The 50-year amplitudes for these events lie approximately at the  $\pm 8\sigma$  and  $\pm 7\sigma$  level, respectively. Two sampling

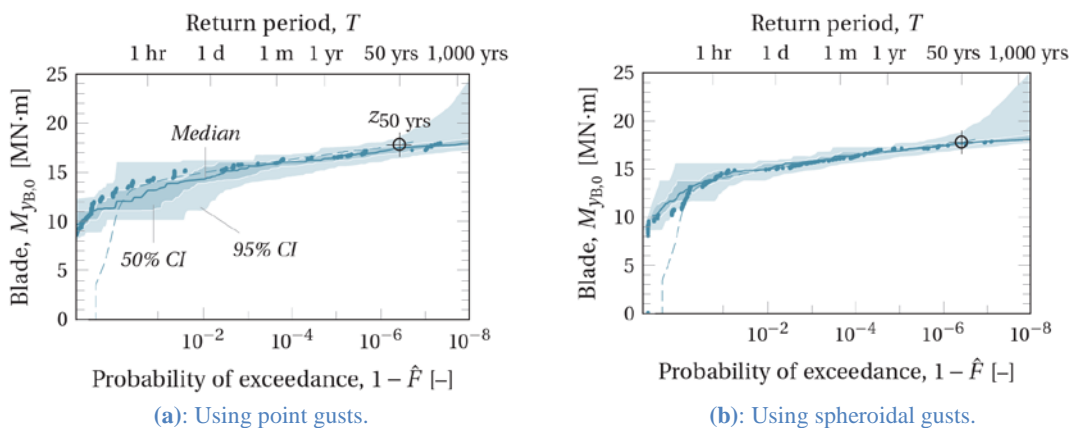


Figure 67: Return level plots obtained by importance sampling ( $N = 10^4$ ). The confidence intervals (CI) were estimated by resampling a larger set of  $5 \cdot 10^4$  gust loads. The dashed line indicates the extreme load distribution constructed from the full, 96-year data set. The dot markers belong to an arbitrary sample.

distributions are then set up:



$$g_1(\bar{U}, A) \approx \frac{1}{2\pi \cdot 2 \cdot 0.5} \exp \left[ -\frac{(U - 20)^2}{2 \cdot 2^2} - \frac{(A/\sigma + 7)^2}{2 \cdot 0.5^2} \right], \quad (30)$$

$$g_2(\bar{U}, A) \approx \frac{1}{2\pi \cdot 2 \cdot 0.5} \exp \left[ -\frac{(U - 20)^2}{2 \cdot 2^2} - \frac{(A/\sigma + 6)^2}{2 \cdot 0.5^2} \right], \quad (31)$$

which are two normal distributions centered on a slightly lower level than the 50-year level. Gusts are then generated from the Kaimal spectrum in two-minute time series (of which the first minute was used as a start-up buffer) and using the same grid settings as in the reference data set. The loads were obtained through FAST v7.<sup>1</sup>

Figure 67 shows the return level plots obtained by these sampling distributions on the basis of a sample size of  $N = 10^4$ . The 50-year load can often be interpolated, which eliminates the need of an extrapolation scheme. With both gust types, the 50-year load is obtained with high accuracy, although the spheroidal gusts produce better results. This is because they are larger and contain more momentum. Therefore, they have a bigger impact on the loads and are thus better correlated to the extremes.<sup>2</sup> The point gusts produce a 95% confidence interval of [16.4, 18.6] MN·m (−7.9%, +4.5%). The spheroidal gusts [17.0, 18.8] MN·m (−4.5%, +5.6%).

An advantage of working with gusts is that they can be stored in one-minute time series. When ignoring the start-up buffer, a sample size of  $N = 10^4$  gusts has the same computational burden of  $N = 10^3$  ten-minute wind fields. In order to make a direct comparison, the performance of the importance sampling method was compared to that of a conventional method that relies on sampling ten-minute wind speeds, either directly from the parent Rayleigh distribution or from a uniform distribution bounded by the cut-in and cut-out points. The extrapolation scheme was automated by setting the starting point of the distribution tail as the center of the plot on Gumbel paper; i.e.,

$$-\ln[-\ln(\hat{F})] > \frac{1}{2} \min\{-\ln[-\ln(\hat{F})]\} + \frac{1}{2} \max\{-\ln[-\ln(\hat{F})]\}. \quad (32)$$

This produced results that were fairly accurate but, most of all, consistent and objective. Extrapolation was then done by fitting a generalized extreme value distribution to the tail:

$$G(M_y; \mu, \sigma, \xi) = \exp \left[ -\left(1 + \xi \frac{M_y - \mu}{\sigma}\right)^{-\frac{1}{\xi}} \right], \quad (33)$$

which seemed to match the tail best for large sample sizes.<sup>3</sup>

<sup>1</sup> A prior check was run with a large number of ten-minute, unconstrained fields to confirm that they produce the same results as the reference data set.

<sup>2</sup> In principle, any gust shape should be able to produce the correct return levels.

<sup>3</sup> For small sample sizes, a straight line often produced better results.



The performance of the methods is expressed as the median absolute deviation to the true 50-year bending moment of 17.8 MN·m:

$$\varepsilon_{\text{MAD}} = \text{median}(|\hat{M}_y - M_y|). \quad (34)$$

This is similar to the root-mean-squared error, but is less distorted by extremely bad fits. Figure 68 then shows the comparison of the methods. For the same quality result, the importance sampling method is,

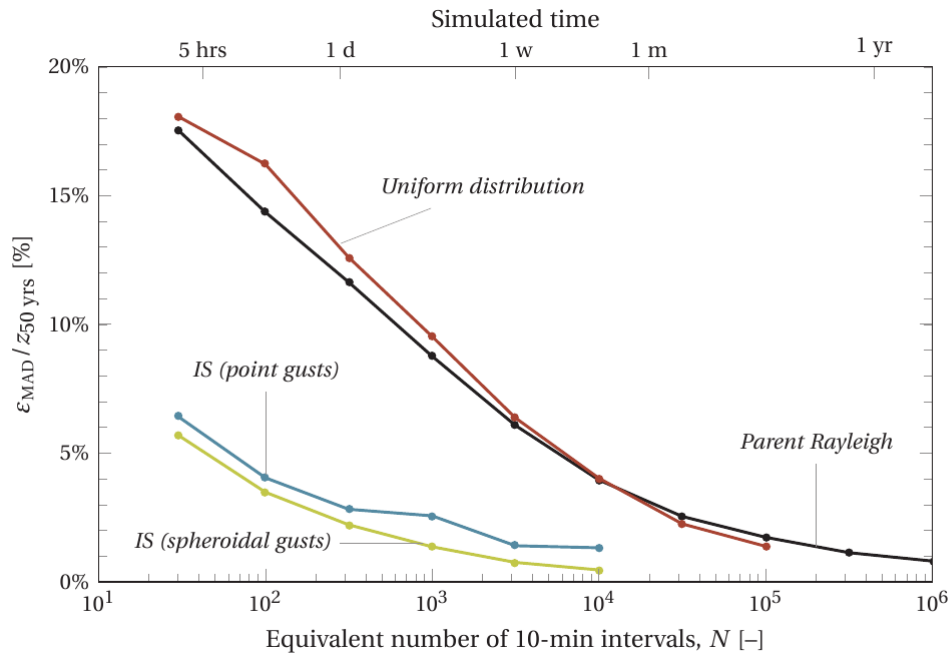


**Figure 68:** Median-absolute deviation to the 50-year load as obtained by the importance sampling method (IS), compared to sampling ten-minute mean wind speeds from a uniform distribution and from the parent Rayleigh distribution (i.e., crude Monte Carlo).

in general, about two orders of magnitude faster than sampling ten-minute mean wind speeds. This makes it especially suitable for early design phases when computational resources are scarce.



## 8.0 Conclusions

Two new wind measurement systems have been demonstrated on wind turbines, the Spinner anemometer for measuring turbulence and as input for wind turbine control and the Spinner lidar for measuring inflow variations in front of the turbine. The demonstrations showed that the spinner anemometer can be directly used for detecting mean wind speed and turbulence as an input for controls. The spinner lidar while showing promise captures a very detailed flow field information, which is more valuable for offline wind analysis rather than for control purposes. De-rating of the turbine power by small levels up to 30% of the rated power during periods of high wind turbulence measured using a spinner anemometer can significantly reduce tower base fatigue and improve the lifetime of jacket sub structures. The loss in energy capture due to de-rating should be compared with the savings in OPEX and increased lifetime.

A new feed-forward individual flap control algorithm based on wind speed measurements obtained using a spinner anemometer was tested. The spinner based flap controller is combined with IPC with the aim to reduce pitch actuator duty cycle. Assessment of load reduction capabilities of the combined pitch/flap control loop against pure IPC and assessment of pitch actuator duty cycle reduction is performed. The new controller has been tested on the DTU 10MW RWT mounted on the DTU jacket. A significant blade flapwise fatigue load reduction ranging between 20-35% depending on the inflow yaw angle is achieved through the new control method. As the controller has been designed with the control objective to reduce 1p variation of blade loads, a slight increase on tower fatigue loads of about 1.5% is obtained at  $0^\circ$  yaw angle that goes up to 4% at  $-15^\circ$  yaw angles. Ultimate load analysis of selected design driving DLCs indicated that overall ultimate blade loads decrease by about 4% while tower and jacket design moment decreases by about 2%.

A comparison has been made between using IPC and IFPC using industry standard IPC algorithms in the INN WIND.EU 10 MW Reference wind turbine. Flap actuation is shown to have very similar blade root loading characteristics to full blade pitching, however depending on the size of flap actuation angles are much larger. In this study a ratio of ~5:1 has been demonstrated. Flap actuation also shows a similar impact on blade tip deflections compared to full span pitching with a ratio closer to 1:1. This indicates that similar algorithms can be used successfully for IFC/IFPC and IPC, though care must be taken to monitor TTC due to the larger blade tip deflections when using flap control. This also demonstrates that for fatigue load reduction, the key advantages from flap control are limited to a reduction in pitch actuator requirements when using the typical d-q axis based control. It may be possible for the actuators to target loading at higher rotor harmonic frequencies than IPC, though less damage is concentrated at these frequencies. With appropriate phase correction in the IPC/IFC commands, IPC and IFC can successfully be applied together in an IFPC arrangement with no additional modification to the IFC/IPC algorithms.



The IFPC controller was shown to produce fatigue DELs with 3% of IPC alone, which is close enough that the difference could be reduced through careful tuning of the IFPC controller. A load case description was created that included flap actuator and algorithm faults. The additional fault cases were not driving cases and the additional freedom of flap actuation was shown to be able to reduce extreme rotor asymmetric loading by using flaps to balance rotor tilt/yaw moments induced through pitch failures. This ability resulted in ~10% reductions in hub yaw and tower base torsional moments relative to IPC alone, whilst keeping other extreme loads within 3.5%. To lead to a reduction in LCoE then, the lifetime additional cost of the flap system must be constrained to the reductions in LCoE from pitch system redesign as well as reduced asymmetric loading on the turbine.

To make full use of an IFPC system, it is recommended that future work look at the cost reductions that could be gained by targeting localised loading along the turbine blade rather than concentrating on blade root loading. This could also be coupled with investigations using multiple flaps along each blade for more degrees of freedom for control.

The integrated innovative concept of a two-bladed rotor mounted on a semi-floater is combined with the advanced control concept of active trailing edge flaps. When comparing the onshore and semi-floater implementations of the two-bladed rotor, it is shown that most of the load channels lifetime fatigue and ultimate levels are largely reduced up to 95% and 78% respectively. When evaluating the performance of the flap controller in the onshore implementation of the two-bladed rotor, it is shown that most of the load channels lifetime fatigue and ultimate levels are largely reduced up to 59% and 47% respectively. When evaluating the performance of the flap controller in the semi-floater offshore implementation of the two-bladed rotor, it is shown that most of the load channels lifetime fatigue and ultimate levels are largely reduced up to 16% and 21% respectively. The results highlight the individual and combined benefit of the semi-floater and flap controller concepts in terms of load alleviation.

The specific LCOE benefits are quantified in more detail in deliverable D1.44.



## References

- [1] Barlas, T. K. and van Kuik, G. A. M., Review of state of the art in smart rotor control research for wind turbines, *Progress in Aerospace Sciences* — 2010, Volume 46, Issue 1, pp. 1-27, 2010.
- [2] Madsen, H. A. et al., Towards an industrial manufactured morphing trailing edge flap system for wind turbines, *Proceedings of EWEC 2014*, Barcelona, Spain, 2014.
- [3] Barlas, T. et al., Extreme load alleviation using industrial implementation of active trailing edge flaps in a full design load basis, *Journal of Physics: Conference Series (Online)*, vol 753, 042001, 2016.
- [4] INN WIND.EU, Deliverable D2.3.2 – Validation of New Control Concepts by Advanced Fluid-Structure Interaction Tools, 2016.
- [5] Bak, C. et al Description of the DTU 10 MW Reference Wind Turbine, Technical report, DTU Vindenergi-I-0092, 2013.
- [6] Larsen, T. J. et al., How 2 Hawc2, the user's manual, Technical report, Risø-R-1597(ver. 4-4)(EN), 2013.
- [7] Bergami, L. and Gaunaa, M., ATEFlap Aerodynamic Model, a dynamic stall model including the effects of trailing edge flap deflection, Technical report, Risø-R-1792(EN), 2012.
- [8] T. von Borstel, "InnWind Design Report Reference Jacket," D4.3.1, 2017.
- [9] Bergami, L., Adaptive Trailing Edge Flaps for Active Load Alleviation in a Smart Rotor Configuration, PhD thesis, DTU Wind Energy, 2013.
- [10] Hansen, M. H. et al., Basic DTU Wind Energy controller, Technical report, DTU Vindenergi-E-0018(EN), Edition 2, 2015 (orbit.dtu.dk).
- [11] INN WIND.EU, Deliverable D1.3.2 – PI-based assessments of 2 bladed concepts, 2016.
- [12] Bergami, L. et al., A Two-Bladed Teetering Hub configuration for the DTU 10 MW RWT: loads considerations. *Proceedings of EWEA 2014*, Barcelona, Spain, 2014.
- [13] IEC. IEC 61400-3. Wind turbines – Part 3: Design requirements for offshore wind turbines, 2005.
- [14] Natarajan, A. et al., Design Load Basis for Offshore Wind turbines: DTU Wind Energy Report No. E-0133, 2016.
- [15] Pedersen TF, Madsen HA, Møller R, Courtney, M, Sørensen NN, Enevoldsen P, Egedal P, "Spinner Anemometry – An Innovative Wind Measurement Concept", *EWEC2007 Milan*.
- [16] Pedersen TF, Sørensen NN, Vita L, Enevoldsen P, Optimization of Wind Turbine Operation by Use of Spinner Anemometer, Risø-R-1654(EN), August 2008
- [17] Pedersen TF, Demurtas G, Zahle F, "Calibration of a spinner anemometer for yaw misalignment measurements", *Wind Energy* 2014, we1798
- [18] IEC 61400-12-1, Wind turbines – part 12-1: Power performance measurements of electricity producing wind turbines, 2005, International Electrotechnical Commission



- [19] Pedersen TF, Demurtas G, Gottschal J, Højstrup J, Nielsen JD, Christiansen W, Weich G, Sommer A, Kristoffersen JR, Improvement of Wind Farm Performance by Means of Spinner Anemometry, DTU Wind Energy E-0040, December 2013
- [20] Pedersen TF, Demurtas G, Sommer A, Højstrup J, Measurement of rotor centre flow direction and turbulence in wind farm environment, Journal of Physics: Conference Series (Online), Vol. 524, No.1, 012167, 2014
- [21] Sjöholm, M., Pedersen, A. T., Angelou, N., Foroughi Abari, F., Mikkelsen, T., Harris, M., ... Kapp, S. (2013). Full two-dimensional rotor plane inflow measurements by a spinner-integrated wind lidar. In *EWEA 2013* (p. PO.ID 250). Vienna. Retrieved from <http://www.ewea.org/annual2013/>
- [22] Kumar, A. A., Bossanyi, E., Scholbrock, A. K., Fleming, P. A., & Boquet, M. (2015). Field Testing of LIDAR Assisted Feedforward Control Algorithms for Improved Speed Control and Fatigue Load Reduction on a 600 kW Wind Turbine. Ewea.
- [23] Mikkelsen, T., Angelou, N., Hansen, K., Sjöholm, M., Harris, M., Slinger, C., ... Vives, G. (2013). A spinner-integrated wind lidar for enhanced wind turbine control. *Wind Energy*, 16(4), 625–643. <http://doi.org/10.1002/we>
- [24] Bos R, Giyanani A, Bierbooms W. (2016). Assessing the severity of wind gusts with lidar. *Remote Sens*, 8, 758. doi:10.3390/rs8090758.
- [25] Frehlich, R.; Meillier, Y.; Jensen, M.L.; Balsley, B.; Sharman, R. (2006). Measurements of boundary layer profiles in an urban environment. *J. Appl. Meteorol. Climatol*, 45, 821–837.
- [26] van der Hooft, E.L.; Schaak, P.; van Engelen, T.G. (2003). *Wind Turbine Control Algorithms*, Energy Research Centre of The Netherlands: Petten, The Netherlands.
- [27] van der Hooft, E.L.; van Engelen, T.G. (2004). Estimated wind speed feed forward control. In: *Proceedings of the European Wind Energy Conference*, 22–25 November 2004, London, UK.
- [28] de Jong, J.J.M.; de Vries, A.C.; Klaasen, W. (1990). Influence of obstacles on the aerodynamic roughness of the Netherlands. *Bound Lay. Meteorol.*, 91, 51–64.
- [29] Sathe, A.R.; Mann, J.; Barlas, T.; Bierbooms, W.A.A.M.; van Bussel, G.J.W. (2013). Influence of atmospheric stability on wind turbine loads. *Wind Energy*, 16, 1013–1032.
- [30] Barone, M., Paquette, J., Resor, B., and Manuel, L. (2012). Decades of wind turbine load simulation, 50th AIAA Aerosp. Sci. Meet. Incl. New Horizons Forum Aerosp. Expo., Nashville, TN, United States, 9–12 January, 2012, doi:10.2514/6.2012-1288.



## Appendix A Load case definition for 10 MW Reference, IPC vs IFPC Comparison (DNV GL)

### General Comments

Fatigue results have been combined assuming:

- Wind with annual mean speed of 10 m/s (Class I) and Weibull distribution.
- Wind directional probability is equal about 12 sectors (360°), so results from four directions (0-90°) can be combined.
- Start-up fatigue loads are accounted for by doubling the fatigue loading from normal shutdown simulations.

Excluded cases have been judged to not meaningfully contribute to lifetime DEL's.

Excluded extreme load cases are assumed not to be driving.

Certain control system failure cases have been excluded as alarm logic renders those failure modes to be benign or equivalent to existing load cases.

### Fatigue Load Cases

<b>Design load case:</b>					1.2			
<b>Operating condition:</b>					Power production			
<b>Wind conditions:</b>					Normal turbulence model, $V_{in} < V_{hub} < V_{out}$			
<b>Sea conditions:</b>					Normal sea state, no currents, MSL			
<b>Type of analysis:</b>					Fatigue			
<b>Partial safety factors</b>					Partial safety factor for fatigue			
<b>Description of simulations:</b>								
	Wind conditions				Wave conditions		Other	
	Vhub (m/s)	Long. TI (%)	Lat. TI (%)	Vert. TI (%)	Hs (m)	Tp (s)	Yaw Error (°)	Hours per year
1.2aax1-2	4	20.40%	16.30%	10.20%	1.10	5.88	-8	175.3
1.2abx1-2							0	175.3
1.2acx1-2							8	175.3
1.2bax1-2	6	17.50%	14.00%	8.75%	1.18	5.76	-8	411.2
1.2bbx1-2							0	411.2
1.2bcx1-2							8	411.2
1.2cax1-2	8	16.00%	12.80%	8.00%	1.31	5.67	-8	440.5
1.2cbx1-2							0	440.5



1.2ccx1-2							8	440.5
1.2dax1-2							-8	415.7
1.2dbx1-2	10	15.20%	12.16%	7.60%	1.48	5.74	0	415.7
1.2dcx1-2							8	415.7
1.2eax1-2							-8	353.7
1.2ebx1-2	12	14.60%	11.68%	7.30%	1.70	5.88	0	353.7
1.2ecx1-2							8	353.7
1.2fax1-2							-8	274.9
1.2fbx1-2	14	14.20%	11.36%	7.10%	1.91	6.07	0	274.9
1.2fcx1-2							8	274.9
1.2gax1-2							-8	196.6
1.2gbx1-2	16	13.90%	11.12%	6.95%	2.19	6.37	0	196.6
1.2gcx1-2							8	196.6
1.2hax1-2							-8	130.0
1.2hbx1-2	18	13.60%	10.88%	6.80%	2.47	6.71	0	130.0
1.2hcx1-2							8	130.0
1.2iax1-2							-8	79.8
1.2ibx1-2	20	13.40%	10.72%	6.70%	2.76	6.99	0	79.8
1.2icx1-2							8	79.8
1.2jax1-2							-8	45.5
1.2jbx1-2	22	13.30%	10.64%	6.65%	3.09	7.40	0	45.5
1.2jcx1-2							8	45.5
1.2kax1-2							-8	24.2
1.2kbx1-2	24	13.10%	10.48%	6.55%	3.42	7.80	0	24.2
1.2kcx1-2							8	24.2
<b>Comments:</b>	<p>Three dimensional three component Kaimal turbulent wind field (600 s sample).            Normal sea state with irregular waves defined using JONSWAP spectrum (Peakedness = 1).            Wind gradient exponent (exponential model), <math>\alpha = 0.14</math>.            Mean sea level of 50 m.            Two seeds per speed and yaw error indexed 1-2.            Simulations run with 4 wind directions in 30° sectors around the structure from 0 - 90° (indexed x=a-d).            Supervisory control is disabled for these simulations.</p>							

<b>Design load case (DLC):</b>	2.4
<b>Operating condition:</b>	Power production followed by a control system fault
<b>Wind conditions:</b>	Normal turbulence model at $V_r$ and $V_{out}$
<b>Sea conditions:</b>	Normal sea state, no currents, MSL
<b>Type of analysis:</b>	Fatigue
<b>Partial safety factors</b>	Partial safety factor for fatigue
<b>Description of simulations:</b>	



	Wind conditions				Wave conditions		Other	
	Vhub (m/s)	Long. TI (%)	Lat. TI (%)	Vert. TI (%)	Hs (m)	Tp (s)	Fault	Occurrences/Hours per year per seed
2.4aax1-6	11.4	14.78%	11.82%	7.39%	1.63	5.84	a	1.7
2.4abx1-6	25	13.00%	10.40%	6.50%	3.60	7.95	a	1.7
2.4bax1-6	11.4	14.78%	11.82%	7.39%	1.63	5.84	b	0.8
2.4bbx1-6	25	13.00%	10.40%	6.50%	3.60	7.95	b	0.8
2.4caxy1-6	11.4	14.78%	11.82%	7.39%	1.63	5.84	c	22.2
2.4cbxy1-6	25	13.00%	10.40%	6.50%	3.60	7.95	c	1.8
<b>Comments:</b>	<p>Three dimensional three component Kaimal turbulent wind field (60 s sample).            Normal sea state with irregular waves defined using JONSWAP spectrum (Peakedness = 1).            Wind gradient exponent (exponential model), <math>\alpha = 0.14</math>            Mean sea level of 50 m.            Six seeds per speed indexed 1-6.            Simulations run with 4 wind directions in 30° sectors around the structure from 0 - 90° (indexed x=a-d)            Fault occurs 20 s into simulation.            Faults considered:            a) Grid loss            b) Transducer error, n4 trip            c) Oblique inflow, i.e. max wind direction from North that control system allows before shutdown. Assumption: 24h per year under these conditions. Indexed y = a/b for +/- yaw.            Amplitudes of 46°, 37°. Simulations run with 4 wind directions in 30° sectors around the structure from 0 - 90° (indexed x=a-d). Supervisory is disabled.</p>							

<b>Design load case (DLC):</b>	6.4
<b>Operating condition:</b>	Parked (stand still or idling)
<b>Wind conditions:</b>	Normal turbulence model, $V_{hub} < 0.7 V_{ref}$
<b>Sea conditions:</b>	Normal sea state, no currents, MSL
<b>Type of analysis:</b>	Fatigue
<b>Partial safety factors:</b>	Partial safety factor for fatigue

<b>Description of simulations:</b>								
	Wind conditions				Wave conditions		Other	
	Vhub (m/s)	Long. TI (%)	Lat. TI (%)	Vert. TI (%)	Hs (m)	Tp (s)	Yaw Error (°)	Hours per year
6.4aax1-2	2	29.20	23.36	14.60	1.07	6.03	-8	345.1
6.4abx1-2							0	345.1
6.4acx1-2							8	345.1
6.4bax1-2	30	11.80	9.44	5.90	4.46	8.86	-8	21.5
6.4bbx1-2							0	21.5
6.4bcx1-2							8	21.5



<b>Comments:</b>	<p>Three dimensional three component Kaimal turbulent wind field (600 s sample).          Normal sea state with irregular waves defined using JONSWAP spectrum (Peakedness = 1).          Wind gradient exponent (exponential model), <math>\alpha = 0.14</math>.          Mean sea level of 50 m.          Two seeds per speed and yaw error indexed 1-2.          Simulations run with 4 wind directions in 30° sectors around the structure from 0 - 90° (indexed x=a-d).          Idling pitch angle of 90°.          Supervisory control is disabled for these simulations.</p>
------------------	--

### Extreme Load Cases

<b>Design load case (DLC):</b>	1.3						
<b>Operating condition:</b>	Power production						
<b>Wind conditions:</b>	Extreme turbulence model, $V_{in} < V_{hub} < V_{out}$						
<b>Sea conditions:</b>	Normal sea state, no currents, MSL						
<b>Type of analysis:</b>	Ultimate						
<b>Partial safety factors</b>	Normal						
<b>Description of simulations:</b>							
	Wind conditions				Wave conditions		Other
	Vhub (m/s)	Long. TI (%)	Lat. TI (%)	Vert. TI (%)	Hs (m)	Tp (s)	Yaw Error (°)
1.3aa1-6	9.4	26.68%	21.34%	13.34%	1.43	5.72	-8
1.3ab1-6							0
1.3ac1-6							8
1.3ba1-6	11.4	23.18%	18.54%	11.59%	1.63	5.84	-8
1.3bb1-6							0
1.3bc1-6							8
1.3ca1-6	13.4	20.74%	16.59%	10.37%	1.85	6.01	-8
1.3cb1-6							0
1.3cc1-6							8
1.3da1-6	20	16.17%	12.94%	8.09%	2.76	6.99	-8
1.3db1-6							0
1.3dc1-6							8
1.3ea1-6	25	14.30%	11.44%	7.15%	3.60	7.95	-8
1.3eb1-6							0
1.3ec1-6							8
<b>Comments:</b>	<p>Three dimensional three component Kaimal turbulent wind field (600 s sample).          Normal sea state with irregular waves defined using JONSWAP spectrum (Peakedness = 1).          Wind gradient exponent (exponential model), <math>\alpha = 0.14</math>.          Mean sea level of 50 m.          Six seeds per speed and yaw error indexed 1-6.          Simulations run with 1 wind directions 0 °  <math>c = 2</math>.          The characteristic loads for each load case group are calculated as the mean of the maxima from each of the six seeds.</p>						



	Supervisory control is disabled for these simulations.
--	--

<b>Design load case (DLC):</b>	1.4
<b>Operating condition:</b>	Power production
<b>Wind conditions:</b>	Extreme coherent gust with change of direction (ECD)
<b>Sea conditions:</b>	Normal sea state, no currents, MSL
<b>Type of analysis:</b>	Ultimate
<b>Partial safety factors</b>	Normal

Description of simulations:							
	Wind conditions				Wave conditions		Other
	Vhub (m/s)	$\Delta V$ (m/s)	V <sub>end</sub> (m/s)	Direction change (°)	Hs (s)	Tp (s)	Yaw Error (°)
1.4aaa_x_z	9.4	15	24.4	25.53	1.43	5.72	-8
1.4aab_x_z							0
1.4aac_x_z							8
1.4aba_x_z	9.4	15	24.4	51.07	1.43	5.72	-8
1.4abb_x_z							0
1.4abc_x_z							8
1.4aca_x_z	9.4	15	24.4	76.60	1.43	5.72	-8
1.4acb_x_z							0
1.4acc_x_z							8
1.4baa_x_z	11.4	15	26.4	21.05	1.63	5.84	-8
1.4bab_x_z							0
1.4bac_x_z							8
1.4bba_x_z	11.4	15	26.4	42.11	1.63	5.84	-8
1.4bbb_x_z							0
1.4bbc_x_z							8
1.4bca_x_z	11.4	15	26.4	63.16	1.63	5.84	-8
1.4bcb_x_z							0
1.4bcc_x_z							8
1.4caa_x_z	13.4	15	28.4	17.91	1.85	6.01	-8
1.4cab_x_z							0
1.4cac_x_z							8
1.4cba_x_z	13.4	15	28.4	35.82	1.85	6.01	-8
1.4cbb_x_z							0
1.4cbc_x_z							8
1.4cca_x_z	13.4	15	28.4	53.73	1.85	6.01	-8
1.4ccb_x_z							0



1.4ccc_x_z						8
<b>Comments:</b>	Steady wind with speed and direction transient (rise time = 10s). Normal sea state with irregular waves defined using JONSWAP spectrum (Peakedness = 1). Wind gradient exponent (exponential model), $\alpha = 0.14$ . Half type transient occurs 10 s into simulation. 200 s simulations. Mean sea level of 50 m. Direction change applied positively (indexed x=1) and negatively (indexed x=2). Simulations run with 1 wind directions 0°.					
	Starting azimuth angle varied from 0-90° in 30° intervals (indexed z =1-4).					

<b>Design load case (DLC):</b>	2.1
<b>Operating condition:</b>	Power production plus occurrence of fault
<b>Wind conditions:</b>	Normal turbulence model, $V_{in} < V_{hub} < V_{out}$
<b>Sea conditions:</b>	Normal sea state, no currents, MSL
<b>Type of analysis:</b>	Ultimate
<b>Partial safety factors</b>	Normal

<b>Description of simulations:</b>					
	Wind conditions		Wave conditions		Other
	Vhub (m/s)	Long. TI (%)	Hs (s)	Tp (s)	Fault
2.1aa01-12	9.4	15.44	1.43	5.72	a
2.1ab01-12					b
2.1ac01-12					c
2.1ba01-12	11.4	14.78	1.63	5.84	a
2.1bb01-12					b
2.1bc01-12					c
2.1bd01-12					d
2.1be01-12					e
2.1ca01-12	13.4	14.32	1.85	6.01	a
2.1cb01-12					b
2.1cc01-12					c
2.1cd01-12					d
2.1ce01-12					e
2.1da01-12	20	13.40	2.76	6.99	a
2.1db01-12					b
2.1dc01-12					c
2.1dd01-12					d
2.1de01-12					e
2.1ea01-12	25	13.00	3.60	7.95	a
2.1eb01-12					b
2.1ec01-12					c



2.1ed01-12					d
2.1ee01-12					e
<b>Comments:</b>	<p>Three dimensional three component Kaimal turbulent wind field (3 min sample).          Normal sea state with irregular waves defined using JONSWAP spectrum (Peakedness = 1).          Wind gradient exponent (exponential model), <math>\alpha = 0.14</math>          Fault occurs 10 s into simulation          Twelve turbulent wind fields used for each simulation, each using a different random number seed (indexed 1-12).          Mean sea level of 50 m          Simulations run with 1 wind directions <math>0^\circ</math>          Faults: a) Controller failure. Over speed n4 trip tested          b) Pitch angle deviation. Individual pitch runaway of blade 1 towards feather (recoverable) at 100% of hardware limit pitch rate          c) Pitch angle deviation. Individual pitch runaway of blade 1 towards fine (recoverable) at 100% of hardware limit pitch rate          d) Flap angle deviation. Individual flap runaway of blade 1 towards feather (recoverable) at 100% of hardware limit pitch rate.          e) Flap angle deviation. Individual flap runaway of blade 1 towards fine (recoverable) 100% of hardware limit pitch rate.          The characteristic loads for each load case group are calculated as the mean of the upper half of the maxima from each of the twelve seeds.</p>				

<b>Design load case (DLC):</b>	2.2
<b>Operating condition:</b>	Power production plus occurrence of fault
<b>Wind conditions:</b>	Normal turbulence model, $V_{in} < V_{hub} < V_{out}$
<b>Sea conditions:</b>	Normal sea state, no currents, MSL
<b>Type of analysis:</b>	Ultimate
<b>Partial safety factors</b>	Abnormal

<b>Description of simulations:</b>					
	Wind conditions		Wave conditions		Other
	Vhub (m/s)	Long. TI (%)	Hs (s)	Tp (s)	Fault
2.2aa1-12	9.4	15.44	1.43	5.72	a
2.2ab1-12					b
2.2ac1-12					c
2.2ba1-12	11.4	14.78	1.63	5.84	a
2.2bb1-12					b
2.2bc1-12					c
2.2bd1-12					d
2.2ca1-12	13.4	14.32	1.85	6.01	a
2.2cb1-12					b
2.2cc1-12					c
2.2cd1-12					d
2.2da1-12	20	13.40	2.76	6.99	a
2.2db1-12					b
2.2dc1-12					c



2.2dd1-12					d
2.2ea1-12	25	13.00	3.60	7.95	a
2.2eb1-12					b
2.2ec1-12					c
2.2ed1-12					d
<b>Comments:</b>					<p>Three dimensional three component Kaimal turbulent wind field (3 min sample).          Normal sea state with irregular waves defined using JONSWAP spectrum (Peakedness = 1).          Wind gradient exponent (exponential model), <math>\alpha = 0.14</math>          Fault occurs 10 s into simulation          Twelve turbulent wind fields used for each simulation, each using a different random number seed (indexed 1-12).          Mean sea level of 50 m          Simulations run with 1 wind directions <math>0^\circ</math>          Faults: a) Controller failure. Over speed nA trip tested          b) Control failure: collective pitch runaway towards fine at 100% of software limit pitch rate          c) Pitch seizure. Single blade fails to pitch (3 min sample).          d) Flap seizure. Single flap fails to pitch (3 min sample).          The characteristic loads for each load case group are calculated as the mean of the upper half of the maxima from each of the twelve seeds.</p>

<b>Design load case (DLC):</b>	2.3			
<b>Operating condition:</b>	Power production plus loss of electrical grid connection			
<b>Wind conditions:</b>	Extreme operating gust (EOG)			
<b>Sea conditions:</b>	Normal sea state, no currents, MSL			
<b>Type of analysis:</b>	Ultimate			
<b>Partial safety factors</b>	Abnormal			
<b>Description of simulations:</b>				
	Wind conditions		Wave conditions	
	Vhub (m/s)	EOG gust (m/s)	Hs (s)	Tp (s)
2.3ab_x_y	9.4	4.69	1.43	5.72
2.3bb_x_y	11.4	5.25	1.63	5.84
2.3cb_x_y	13.4	5.80	1.85	6.01
2.3db_x_y	20	7.64	2.76	6.99
2.3eb_x_y	25	9.03	3.60	7.95
<b>Comments:</b>	<p>Steady wind with transient gust (gust period = 10.5s). 1 minute simulations          Normal sea state with irregular waves defined using JONSWAP spectrum (Peakedness = 1).          Wind gradient exponent (exponential model), <math>\alpha = 0.14</math>          Gust occurs 10 s into simulation          Internal or external electrical fault modelled as an instantaneous loss of the generator torque          Mean sea level of 50 m          Simulations run with 1 wind directions <math>0^\circ</math>          Fault phasing indexed x=a-d corresponds to tstart gust +0, +2.45, +4.0 and +5.25s respectively.          Starting azimuth angle varied from <math>0-90^\circ</math> in <math>30^\circ</math> intervals (indexed y=a-d).          Wind direction is <math>0^\circ</math></p>			



<b>Design load case (DLC):</b> <b>Operating condition:</b> <b>Wind conditions:</b> <b>Sea conditions:</b> <b>Type of analysis:</b> <b>Partial safety factors</b>		4.2 Normal shut-down plus deterministic gust Extreme operating gust (EOG) Normal sea state, no currents, MSL Ultimate Normal		
<b>Description of simulations:</b>				
	Wind conditions		Wave conditions	
	Vhub (m/s)	EOG gust (m/s)	Hs (s)	Tp (s)
4.2ab_x_y	9.4	4.69	1.43	5.72
4.2bb_x_y	11.4	5.25	1.63	5.84
4.2cb_x_y	13.4	5.80	1.85	6.01
4.2db_x_y	20	7.64	2.76	6.99
4.2eb_x_y	25	9.03	3.60	7.95
<b>Comments:</b>	Steady wind with transient gust (gust period = 10.5s). 1 minute simulations Normal sea state with irregular waves defined using JONSWAP spectrum (Peakedness = 1). Wind gradient exponent (exponential model), $\alpha = 0.14$ . Gust occurs 10 s into simulation. Mean sea level of 50 m. Simulations run with 1 wind directions 0°.			
	Normal stop phasing indexed x=1-4 corresponds to tstart gust +0, +2.45, +4.0 and +5.25s respectively. Starting azimuth angle varied from 0-90° in 30° intervals (indexed y=1-4). Wind direction is 0°.			